Summer 2011

Computational investigation of plasma actuator as an active flow control strategy of laminar separation bubbles

Justin Roger Aholt

Department:

COMPUTATIONAL INVESTIGATION OF PLASMA ACTUATOR AS AN ACTIVE FLOW CONTROL STRATEGY OF LAMINAR SEPARATION BUBBLES

by

JUSTIN ROGER AHOLT

A THESIS

Presented to the Faculty of the Graduate School of the

MISSOURI UNIVERSITY OF SCIENCE AND TECHNOLOGY

In Partial Fulfillment of the Requirements for the Degree

MASTER OF SCIENCE IN AEROSPACE ENGINEERING

2011

Approved by

Fathi Finaish, Advisor
Serhat Hosder
Joshua Rovey

ABSTRACT

A parametric computational study designed to examine the plausibility of an external body force generated by active means, such as a plasma actuator, as a means of controlling a Laminar Separation Bubble (LSB) over an airfoil at low Reynolds numbers was conducted. Computational Fluid Dynamics (CFD) was employed to characterize the effect that a body force, localized to a small region tangent to the airfoil surface, might have on an LSB.

In this study, the effects of altering the strength and location of the "actuator" on the size and location of the LSB and on the aerodynamic performance of the airfoil were observed. In a separate investigation, the effects of operating an actuator in a 'burst' mode are investigated, where the effects of pulsing frequency and duty cycle are examined to determine whether further performance enhancements can be achieved via such means.

It was found that the body force, when properly located and with sufficient magnitude, could effectively eliminate the LSB. Additionally, it was found that by eliminating the LSB, the aerodynamic efficiency of the airfoil could be improved by as much as 60%. Thus, it was determined that such a system may indeed be an effective measure of reducing or eliminating the negative effects associated with LSBs at low Reynolds numbers. Additionally, pulsed operation of the actuator was found to enhance effectiveness by as much as 20% over a power-equivalent steady actuator. These results indicate that such a control strategy may be an excellent candidate for future experimental research regarding this topic.

ACKNOWLEDGMENTS

I first wish to thank my advisor, Dr. Fathi Finaish, for his years of guidance and support, both in my research experience and personal development. I also wish to thank Dr. Serhat Hosder and Dr. Joshua Rovey for their service on my committee and all advice and assistance they provided me with this project. Their help is sincerely appreciated. I would also like to acknowledge the facilities and resources provided by the Department of Mechanical and Aerospace Engineering at the Missouri University of Science and Technology, as well as the financial support of the NASA-Missouri Space Grant Consortium.

TABLE OF CONTENTS

LIST OF ILLUSTRATIONS

Page

LIST OF TABLES

Page

NOMENCLATURE

Symbol	Description
α	Airfoil angle of attack (degrees)
ρ_∞	Free-stream density (kg/m^3)
μ_∞	Free-stream dynamic viscosity (Pa-s)
A^*	Actuator cross-sectional area (volume per unit span to which body force is applied, scaled to c^2, dimensionless)
A_{eff}	Effective actuator discharge volume per unit span (m^2)
c	chord-length (m)
C_d	Drag coefficient
C_l	Lift coefficient
C_p	Pressure coefficient
D	Actuator duty cycle (dimensionless)
f	Dimensionless actuator pulse frequency, $= \frac{1}{T}$
f_d	Magnitude of applied body-force per unit volume (N/m^3)
f_{nd}	Dimensionless body force per unit volume, $= \frac{f_d c}{\rho_\infty V_\infty^2}$
K_{sc}	Dimensionless actuator scaling parameter, $= \frac{\rho_\infty}{\mu_\infty^2} T' c$
L/D	Lift-to-drag ratio, $= \frac{C_l}{C_d}$
M_∞	Free-stream Mach number
Re	Chord Reynolds number, $= \frac{\rho_\infty V_\infty c}{\mu_\infty}$
T	Dimensionless actuation period, $= \frac{T_d V_\infty}{c}$
T_d	Actuation period (s)
T'	Actuator thrust per unit span (N/m)
t_{pd}	Time actuator is active over 1 duty cycle (s)
t_p	Dimensionless time actuator is active over 1 duty cycle, $= \frac{t_{pd} V_\infty}{c}$
V_∞	Free-stream velocity (m/s)
x	Chord-wise position with respect to airfoil leading edge (m)

X	$= \frac{x}{c}$
x_s	Chord-wise position with respect to laminar separation point (m)
X_s	$= \frac{x_s}{c}$
y	Chord-normal position with respect to airfoil leading edge (m)
Y	$= \frac{y}{c}$

1. INTRODUCTION

A variety of factors have led to a surge in present interest in low Reynolds number aerodynamics. For instance, recent interest in renewable energy has resulted in growing interest in wind turbines and related technologies. Recent advancements in the fields of micro-system technology have enabled the development of mini- and micro aerial vehicles, which have a broad range of potential applications. The development of aircraft on such a small scale has led to a variety of previously rarely encountered low Reynolds number boundary layer phenomena, such as laminar separation bubbles.

The boundary layer is extremely influential to aerodynamic performance characteristics, especially drag. The boundary layer is also characteristically sensitive; i.e. small perturbations to the boundary layer can result in significant alterations of aerodynamic performance. It is thought that active control strategies designed to take advantage of this instability could effect significant improvements in performance with relatively low power requirements.

1.1. LITERATURE SURVEY

1.1.1. Laminar Separation Bubbles. A Laminar Separation Bubble (LSB) is a phenomenon which has been encountered in a variety of subsonic, low Reynolds number aerospace applications. A LSB is a phenomenon which occurs when a laminar boundary layer encounters an adverse pressure gradient along an aerodynamic surface, which induces boundary layer separation. Instability inherent to the free-shear layer causes the boundary layer to undergo a rapid turbulent transition. This turbulence results in increased momentum transport normal to the shear layer, entraining the low-momentum fluid in the wake of the separation point and causing boundary layer reattachment. This process results in the formation of a closed bubble, as shown in Figure 1.1.

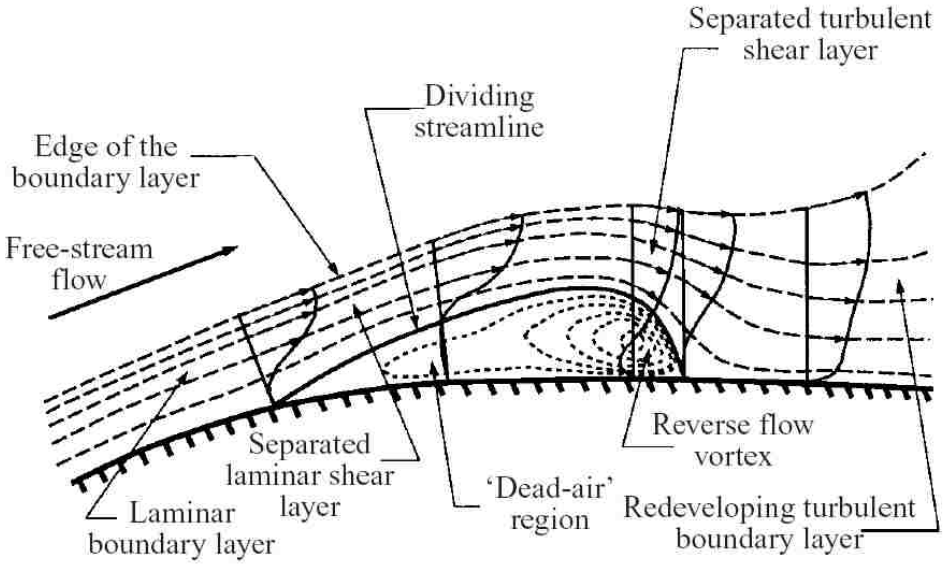

Figure 1.1. Conceptual schematic of a laminar separation bubble. From Horton [1].

1.1.1.1 Common Characteristics of LSBs. LSBs are widely regarded as a low Reynolds number phenomenon, rarely observed in applications with characteristic Reynolds numbers greater than 10^6 [2]. Although a laminar boundary layer and adverse pressure gradient are requisite to the formation of a LSB, they do not, by any means, guarantee its formation. In fact, LSBs are only found to exist within a narrow range of pressure gradients and Reynolds numbers. Too small a pressure gradient fails to induce laminar separation, while too large a pressure gradient leads to laminar separation without reattachment. Analogous trends are observed with variation in Reynolds number. LSBs are not necessarily steady. Low frequency LSB oscillations have been observed on airfoils which are susceptible to trailing-edge or thin-airfoil stall [3]. Additionally, LSBs are generally found to be highly sensitive to stimuli. Experimental studies such as that by Zaman and McKinzie [4] have found that LSBs could be manipulated via mere acoustic excitation. Other studies have found minute changes in Reynolds number and upstream flow-field perturbations to be capable of dramatically altering LSB dimensions and aerodynamic effects, as well as inducing LSB instability and 'bursting', whereby the turbulent boundary layer fails to reattach to the surface, causing premature leading-edge stall [3, 5].

LSBs can potentially have a great impact on the aerodynamic performance of a body. Studies have shown that, while an LSB can enhance lift under certain circumstances, its primary contribution to aerodynamic performance typically comes in the form of a pressure drag penalty. Several factors contribute to this adverse behavior. By displacing the inviscid flow over the leading edge of the airfoil, the LSB simultaneously degrades the airfoil's natural suction peak and decreases pressure recovery over the aft portion of the airfoil, as shown in Figure 1.2.

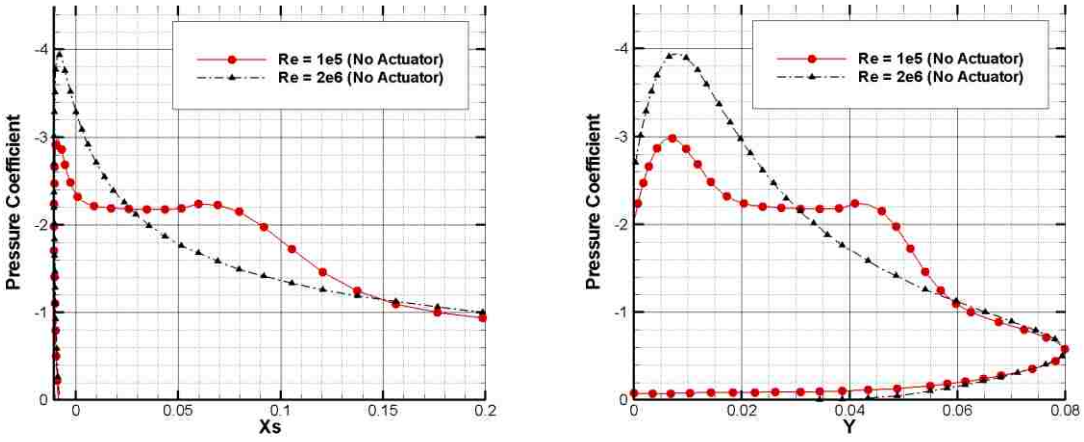

(a) C_p vs. X_s (b) C_p *vs. Y*

Figure 1.2. Comparison between pressure distributions of 16% thick elliptic airfoil with and without LSB ($\alpha = 10°$)

The drag resulting from an LSB can be tremendous. For the case shown in Figure 1.2, the drag coefficient of the airfoil with the LSB is over 150 percent greater than that without [6]. Similar behavior has been noted for other airfoils as well [7, 8]. The instability which characterizes many LSBs may also influence aerodynamic performance. The aforementioned unsteady behavior of certain LSBs has also been found to dramatically affect aerodynamic performance. A study by Zaman *et al.* [9] found that this phenomenon resulted in lift coefficient fluctuations of as much as 50 percent over certain airfoils. At its extreme, this phenomenon results in periodic bursting.

1.1.1.2 LSBs in Practice. LSBs are commonly encountered in a wide variety of aerospace applications. However, LSBs are almost universally considered a parasitic phenomenon, both as a result of their tendency to reduce aerodynamic performance and their unpredictability. Consequently, the goal of most current research regarding this topic is LSB elimination. A sampling of applications in which LSBs are encountered is given here.

Wind Energy. Wind turbines are required to operate under a wide variety of operating conditions. In the development of stall-regulated turbines, observations were made that, at high wind speeds, the turbines chaotically exhibited multiple distinct power levels under seemingly identical conditions. Upon further study by Bak, *et al.* [5], it was found that the turbine blades were exhibiting two distinct stalling angles of attack, a phenomenon which came to be known as 'double stall', and that the cause of this phenomenon was the existence of a LSB. In this study, it was found that the LSB was extremely sensitive to upstream conditions, and that the premature stall was the result of LSB bursting. Double stall presents a number of issues, specifically regarding the estimation of long term energy production and the determination of the maximum projected blade loading. Additionally, it has raised concerns over dynamic loading characteristics resulting from stall-induced vibrations [5, 10].

Turbo-machinery. A study by Hourmouziadis [11] found that at high altitude cruise, the Reynolds numbers of Low Pressure Turbine (LPT) blades can drop below 25,000, and a study by Sharma [12] found that the losses experienced by LPT blades can increase by nearly 300 percent as the blade Reynolds number is decreased below 200,000. He found these losses to be the result of laminar separation over the blade's suction surface. An experimental study conducted by Stieger *et al.* [13] confirms the existence of laminar separation over LPT blades. Stieger observed large scale fluctuations in the surface pressure distribution over the blades of a LPT cascade. It was found that the source of the fluctuations was the existence of a periodically bursting LSB, similar to that observed by Bak [5]. Stieger observed that the blade row pressure drop could fluctuate by as much as 30 percent due to this phenomenon.

Unmanned Aerial Vehicles. Recent advancements in the field of micro-system technologies have resulted in the development of mini- and micro-UAVs, which have a

broad range of potential applications. Due to the scale of such aircraft, Reynolds numbers in the 40,000 to 500,000 range are very common, making the aircraft susceptible to low Reynolds number phenomena such as LSBs. In the design of low Reynolds number lifting bodies, LSB consideration is critical. As reported by Nagel, *et al.* [14], a problem often encountered in low Reynolds number wing design is an abrupt loss of lift as a result of stall induced by LSB bursting. A study by Leslie *et al.* [15] noted that LSBs commonly exist on UAV propellers, and that they are a leading source of propeller noise. Leslie found that by eliminating LSBs, propeller noise could be reduced by as much as 4 dB.

Planetary Exploration. Aircraft have been identified as an advantageous means of Martian exploration in the distant future [16]. Such an exploration vehicle would be advantageous to orbiting satellites with respect to observation data quality, and to ground-based rovers with respect to mobility. However, the density of the Martian atmosphere is roughly one percent of the Earth's, and early Martian aircraft size will likely be limited by launch constraints. Consequently, characteristic Reynolds numbers of the first Martian aircraft will likely be on the order of 1000 – 100,000 [16]. Thus, it is likely that Martian UAVs will encounter many of the same low Reynolds number phenomena as their counterparts on Earth, including LSBs.

1.1.1.3 Methods of LSB Control. Because LSBs are generally considered undesirable, due to the parasitic and unpredictable effects they typically have on aerodynamic performance, the goal of most current research efforts regarding LSBs is their elimination. LSB control methods can be broadly categorized as either passive or active control strategies. Active control differs from passive control in that active control requires the supply of external power and/or input.

Passive Control Strategies. The majority of LSB control strategies are passive. The simplest and most commonly implemented strategy of LSB elimination is the imposition of mechanical turbulators to existing designs and structures. The principle under which a turbulator operates is simple: The turbulator, placed upstream of the laminar separation point, acts as an amplifier of laminar boundary layer instabilities, promoting premature turbulent transition. Because turbulent flow is less prone to separation than laminar flow, the flow is less likely to separate from the surface when

encountering an adverse pressure gradient. Turbulators take a number of forms, ranging from zigzag and dimple tape to boundary layer trip wires. Such control strategies have been successfully implemented by Stieger [13] on LPT blades and Leslie [15] on UAV propellers. A second method of LSB elimination is 'careful' aerodynamic design. Typically, airfoils are specially designed with high leading edge curvature to promote premature turbulent transition, as with turbulators. This control strategy was employed successfully by Bak [5] on wind turbine airfoils. Conceivably, one could also use such a strategy to smooth the adverse pressure gradient responsible for separation. A third passive control mechanism which has been successfully demonstrated is the application of vortex generators. Vortex generators are typically small vanes oriented perpendicular to the airfoil surface, but with an incidence to the flow direction. Vortex generators induce stream-wise vortices to the boundary layer. These vortices energize the boundary layer and induce a turbulent transition, which prevents flow separation.

As indicated, most passive control strategies rely upon artificial turbulence generation as a means of preventing flow separation. All passive control devices are optimized for a specific design condition, and thus typically perform sub-optimally under off-design conditions. In applications where a variety of flow conditions are encountered, the turbulence inducing controls are typically beneficial under only a small subset of those conditions, inducing a net drag penalty much of the expected operating time.

Active Control Strategies. The potential for active flow control strategies is evident, whereby, in contrast to passive control strategies, systems are capable of being dynamically controlled to maintain optimal aerodynamic performance of a device over a range of operating conditions. However, current active LSB control technology is immature. To successfully implement a LSB control system, interactive techniques are required to determine the existence of an LSB and the measures required to control it optimally in real time. Novel LSB sensors, such as that developed by King *et al.* [2] have been developed to provide this capability, but attempts at integration with LSB control systems have not met complete success. Additional concerns exist for individual control systems. Consequently, active LSB control strategies have not been widely adopted in

practice. However, despite these challenges, there is a general consensus that active control strategies show a great deal of promise in this application.

One of the simplest active LSB control systems available is an adaptive mechanical turbulator. Similar in concept and function to a passive turbulator, adaptive turbulators rely upon turbulence generation to prevent flow separation. However, adaptive turbulators are retractable, and can thus be removed from the flow field when unneeded. One drawback to adaptive turbulators, as reported by King [2], is an inability to alter the effectiveness of the turbulator, limiting the range of its usefulness. A second drawback of adaptive turbulators is the requirement of mechanical parts to actuate the control system. Similar control strategies have been applied with vortex generators. Other, more complex, control systems involve sucking or blowing air through holes in the surface to generate vortices which suppress separation [17]. However, these methods require complex, and often heavy, systems to process volumes of air, making them impractical for many aerospace applications.

1.1.2. Introduction to Aerodynamic Plasma Actuators. An aerodynamic plasma actuator is a relatively simple device, consisting of a pair of electrodes separated by a dielectric material, arranged in an asymmetric configuration, as shown in Figure 1.3. As shown, one of the electrodes is exposed to the ambient fluid, while the other is embedded within the dielectric material. In most test articles, the electrodes are thin copper strips, and the dielectric material is Kapton polyimide film [18, 19].

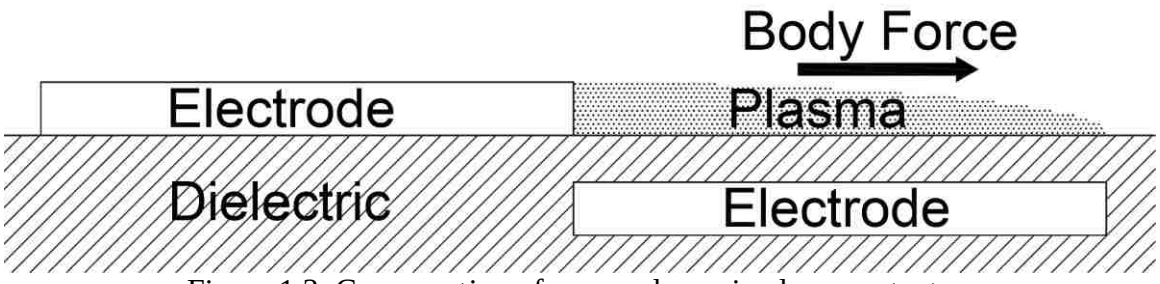

Figure 1.3. Cross-section of an aerodynamic plasma actuator

Plasma actuators are operated by applying a high voltage ac potential across the electrodes. When the potential difference reaches critical amplitude, the fluid in the region of the region between the exposed electrode and dielectric ionizes, resulting in a plasma discharge, as shown in Figure 1.4. This discharge has the effect of imparting directed momentum into the surrounding fluid. This injection of momentum can have a profound impact on the local flow-field. If properly exploited, plasma actuators can be a very effective flow control mechanism. Although plasma actuators require large voltages to operate, they require very little current, and most plasma actuators operate at power levels between 2 and 40 Watts per foot of span [20].

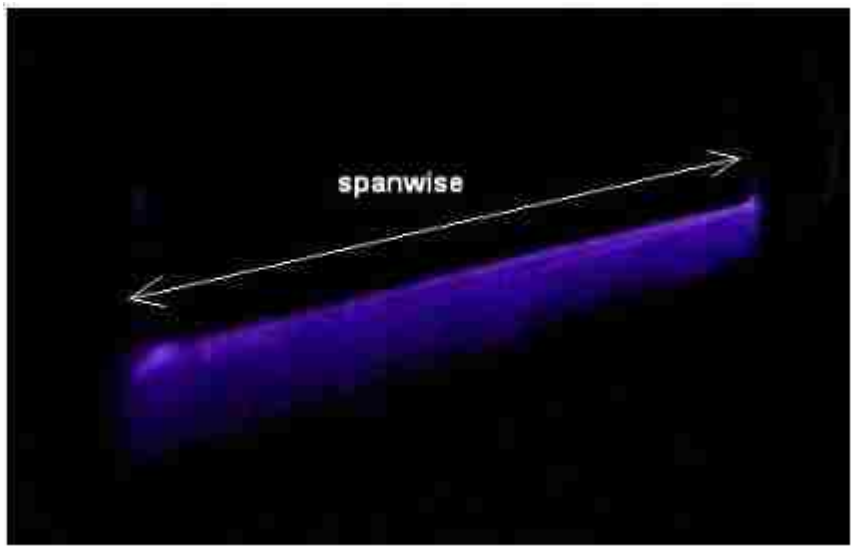

Figure 1.4. Plasma actuator in action. From Corke, *et al* [21].

1.1.2.1 Dielectric Barrier Discharge Plasmas. The Dielectric Barrier Discharge (DBD) requires a high ac potential (typically 5 to 10 kV_{p-p}), applied across the electrodes at a frequency of 1 to 10 kHz [18, 19]. During the half-cycle of the discharge over which the exposed electrode acts as cathode, electrons build up, and begin emitting from the surface of the electrode. These electrons interact with the neutral fluid between the electrode and the dielectric, weakly ionizing the gas, before depositing on the surface of

the dielectric. The generated plasma experiences a body force along the field lines, proportional to the local electric field strength. The dielectric barrier physically prevents the electrons from reaching the embedded electrode, so the charges build up on the dielectric surface, opposing the applied voltage. For this reason, the process is self-limiting; i.e. the potential difference must be continually increased for the discharge to be maintained. Similar behavior is observed on the positive running half-cycle of the discharge. In this case, the discharge is limited by the number of charges deposited on the dielectric surface during the previous half-cycle. This self-limiting behavior allows for a sustained discharge without arcing at atmospheric pressure [18].

Although a DBD plasma resembles a steady glow discharge to the naked eye, it is actually a highly organized structure, both spatially and temporally [19], as illustrated in Figure 1.5. This structure is highly dependent upon the applied voltage waveform. However, the frequency at which the DBD is driven is typically several orders of magnitude greater than the characteristic fluid response frequency, causing the actuator to behave in a quasi-steady manner, unless forced to behave otherwise. Recent research has shown that, by pulsing the actuator at frequencies designed to amplify flow instabilities, actuator effectiveness can be dramatically improved in certain flow control applications [16, 21, 22].

1.1.2.2 Advantages and Disadvantages of Plasma Actuators. Plasma actuators present several distinct advantages over conventional flow control devices. Plasma actuators are purely solid state devices, requiring no moving parts or bleed air to operate. They have virtually no effect on aerodynamic performance when not employed, and their effectiveness can be modulated simply via variation in power input. Plasma actuators feature actuation response times far smaller than that achievable via mechanical means. As previously mentioned, plasma actuators can be adapted to operate at characteristic fluid frequencies, so as to excite desired flow instabilities.

However, plasma actuators also have several disadvantages. Though a plasma actuator is not typically considered a massive component, its operation typically necessitates the use of a high voltage power supply, and often some means of energy storage, such as a battery. In weight-sensitive applications, such as aircraft flow control, the weight penalty incurred by such components can outweigh the aerodynamic benefits

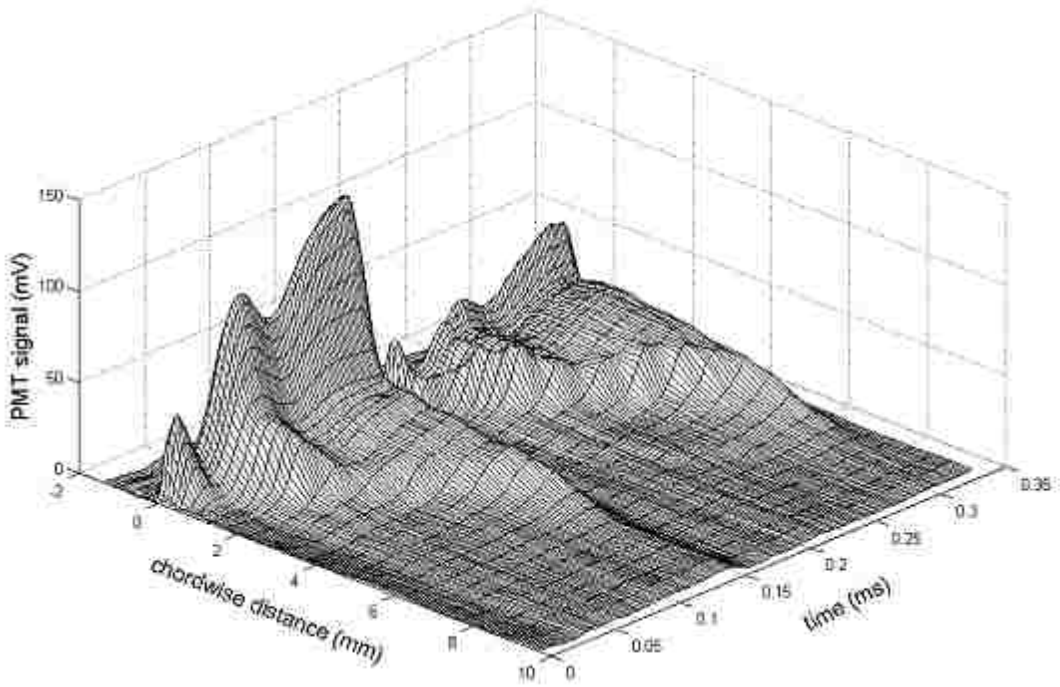

Figure 1.5. Spatial-temporal structure of a DBD discharge (PMT signal is proportional to plasma density). From Enloe *et al.* [19].

gained from the actuator. In such applications, it is important to weigh the advantages gained via plasma actuator use against the drawbacks.

1.1.2.3 Current Applications. Plasma actuators have been successfully implemented in a variety of current flow control applications. They have been used to particular effect in low Reynolds number and boundary layer control applications. For instance, an experimental study by Huang *et al.* [23] examined the effect that a plasma actuator might have on laminar boundary layer separation over airfoils in a LPT cascade. It was observed that operation of a plasma actuator steadily downstream of the separation point resulted in airfoil performance improvements comparable to that achieved via a vortex generator. An innovative study by Nelson *et al.* [24] found that steady DBD plasma actuators could be moderately effective in enhancement of traditional turbine blade stall characteristics and lift generation. The study also introduced a strategy of enhancing actuator performance. This strategy involved deliberately modifying the airfoil shape to induce flow separation at selected positions on the airfoil surface, and

placing unsteadily operated actuators in position to control the resultant separation. It was found that this resulted in dramatic improvements to actuator effectiveness. Plasma actuators have also been identified as possible means of augmenting lift over low Reynolds number wings [21, 25, 26] and preventing rotating stall in compressors [27], among others. Although most of these applications have made use of steady actuation, recent studies have shown that plasma actuators operated at unsteady frequencies designed to amplify boundary layer instabilities could result in even more dramatic performance enhancements than previously thought in the controlling of unsteady phenomena [16, 21, 22].

1.2. PLASMA ACTUATORS AS A POTENTIAL METHOD OF LSB CONTROL

Due to the success that plasma actuators have demonstrated in various low Reynolds number and boundary layer applications, it is thought that they may effective in the control of LSBs. Whereas current LSB control mechanisms rely on turbulence generation to prevent separation, it is thought that plasma actuators could achieve the same effect by injecting enough momentum into the boundary layer to overcome the adverse pressure gradient responsible for separation. This strategy of LSB elimination is thought to be superior to conventional means because it does not rely upon turbulence as a means to the end of LSB elimination. Thus, drag could be reduced beyond the capabilities of conventional means. Additionally, it is thought that the ability of plasma actuators to control unsteady phenomena via low frequency pulsing could be harnessed to exert additional control over LSBs.

1.3. SCOPE OF THE PRESENT WORK

1.3.1. The Flow Problem and Associated Parameter Space. In this study, a baseline case in which a large Laminar Separation Bubble is present is selected for manipulation. In this study, a 16 percent thick elliptical airfoil at a 10 degree angle of attack is selected, as illustrated in Figure 1.6. The selected Reynolds number and Mach number in this case are 10^5 and 0.01, respectively.

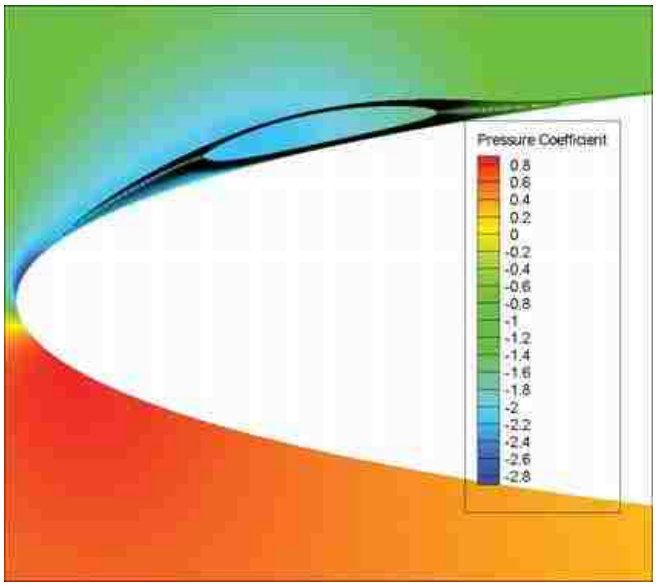

Figure 1.6. Stream traces and pressure coefficient contour plot of baseline flow problem

The primary objective of this computational study is to assess the feasibility of a plasma actuator as a means of controlling Laminar Separation Bubbles. Both steady and pulsed plasma actuation modes are investigated. In this study, a LSB is observed over the leading edge of a 16 percent thick elliptical airfoil at low Reynolds numbers. A plasma actuator, modeled as a localized body force, is applied to the airfoil surface, and used to effect changes in the characteristics of the bubble and the aerodynamic performance of the airfoil. Parametric studies are conducted for both the steady and pulsed actuator configuration to determine the optimal configurations of the actuator in each case. The pulsed and steady control methods are compared to determine the advantages gained by pulsing the actuator. Additionally, power and voltage requirements of the plasma actuator are estimated in order to gauge the practicality and effectiveness of the proposed LSB control method.

1.3.2. Steady Actuator Modeling and Optimization. An effort is made to estimate the effect that a steadily operated plasma actuator can have on the baseline LSB case listed above at a Reynolds number of 10^5. Toward this end, it is necessary to modify

a commercial Computational Fluid Dynamics (CFD) code to incorporate a localized body force. A parametric study is conducted, in which the location and strength of the actuator are varied, in order to determine the optimal configuration of the actuator. The practicality of such a plasma actuator configuration is examined.

1.3.3. Pulsed Actuator Modeling and Optimization. In contrast to a steadily operated actuator, a pulsed actuator can control separation via periodic excitation of boundary layer instabilities. For instance, the actuator can be used to induce Tollmien-Schlichting (TS) waves upstream of the laminar separation point, forcing premature turbulent transition, and thus preventing separation [28]. It is necessary to modify the CFD code to handle a pulsed body force. A parametric study is conducted, in which the pulsing frequency and duty cycle of the actuator are varied. One goal of this study is to establish a relationship between pulsing frequency and duty cycle of the actuator and its influence on aerodynamic performance. A second goal is to determine the optimal pulsed actuator configuration. The effectiveness of the pulsed actuator configurations is then compared to that of the steady configuration to determine whether unsteady actuation is beneficial.

2. COMPUTATIONAL APPROACH

2.1. FLOW-FIELD GRID GENERATION

2.1.1. Surface Geometry Definition. For obvious reasons, it was necessary to select an airfoil over which LSBs have been observed in practice. In this study, a 16 percent thick elliptical airfoil was selected as the surface geometry upon which to conduct this analysis. While elliptical airfoils are rarely if ever used in current aerospace applications, they have been proposed for niche applications such as hybrid rotor/wing aircraft [29]. In any case, the geometry of the selected airfoil itself is immaterial to the purposes of this study. What is important is the fact that the existence of laminar separation bubbles over the leading edge of the airfoil under specific free-stream conditions has been numerically confirmed, making it a suitable airfoil geometry for this study [29].

2.1.2. Surface Grid Generation. In this study, a baseline 250 point surface grid was slightly modified to accommodate the actuator model. The original grid featured 250 points, with point density proportional to the curvature of the airfoil, as shown in Figure 2.1.

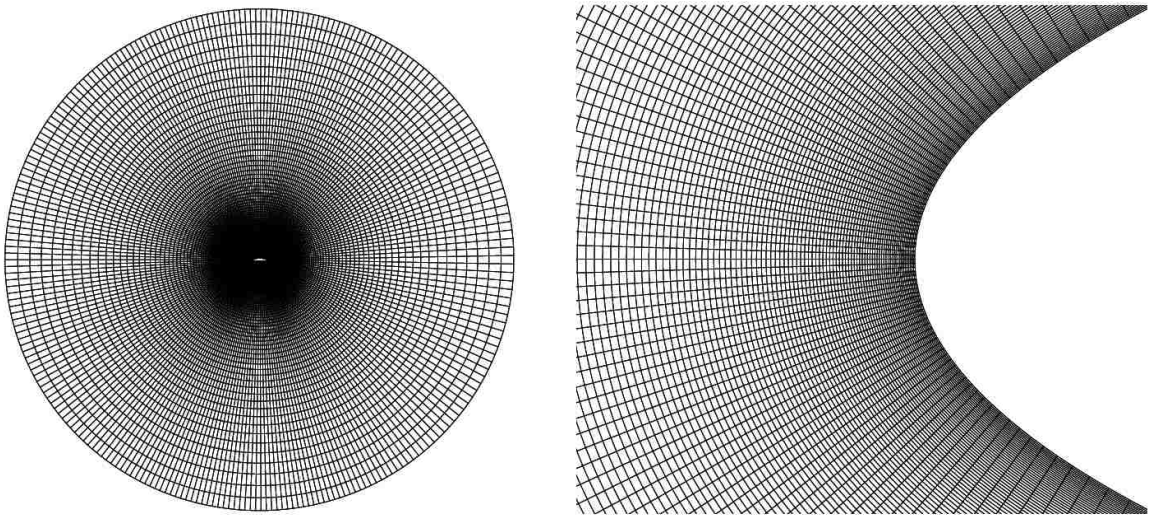

(a) Full grid (b) Close-up of grid leading edge

Figure 2.1. Original volume grid

This ensured that regions in which the highest pressure and velocity gradients are expected would have adequate stream-wise grid density to capture said gradients. The surface grid was limited to 250 points due to a flow-solver constraint. As previously mentioned, the grid was modified to handle a 'plasma actuator' model. Grid points were reallocated from the aft lower surface of the airfoil to the leading edge region over which the actuator was to be placed. In this region, the points were distributed linearly to prevent changes in the size of the actuator region, as shown in Figure 2.2.

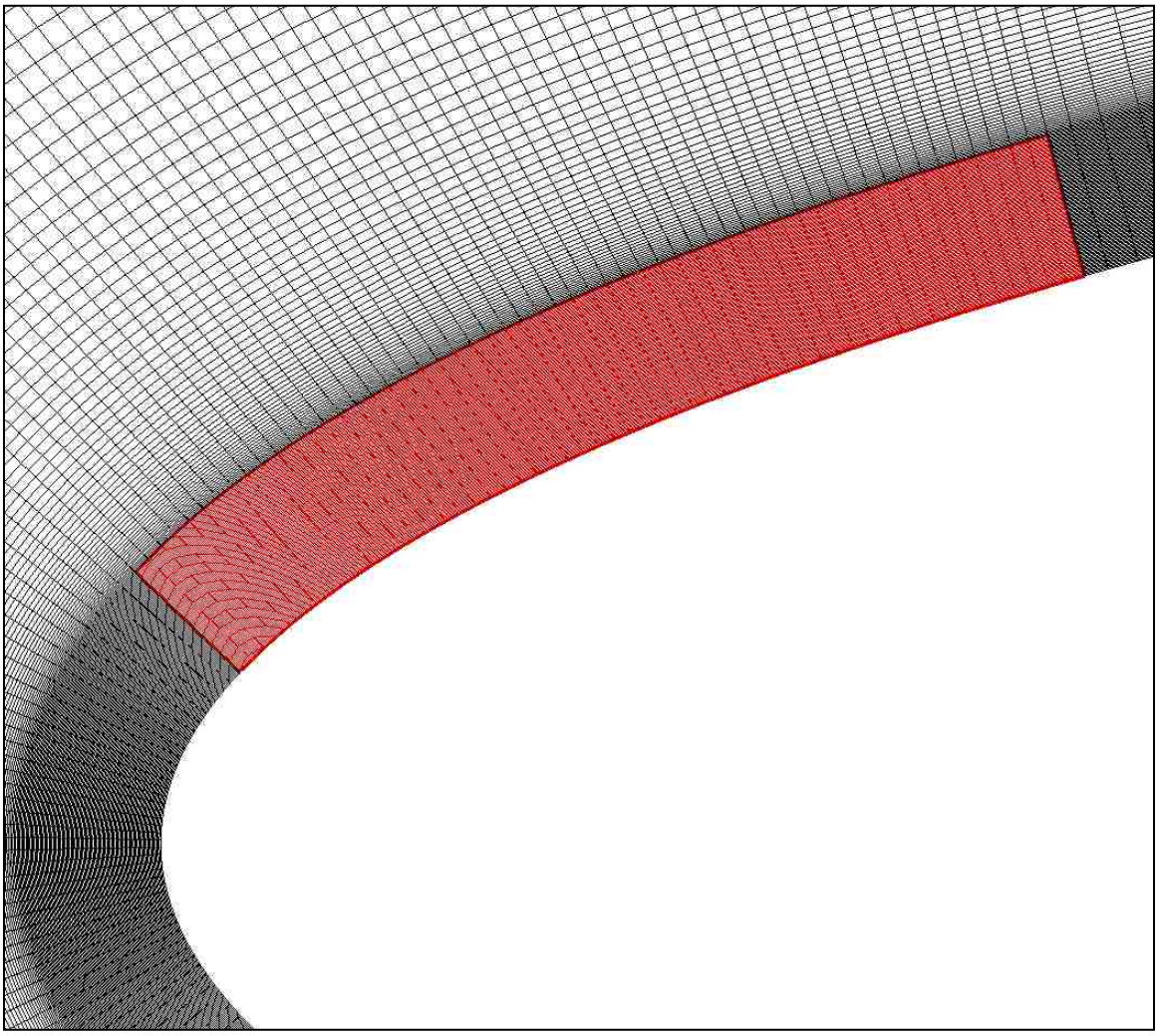

Figure 2.2. Upper leading edge of modified volume grid (stream-wise linear region is highlighted in red)

Grid density is lost over the lower trailing edge as a result of this grid point reallocation. However, because the lower trailing edge is far removed from the flow-field region of interest where the LSB is observed (the upper leading edge), the effect that the reduced grid density over this region has on the numerical accuracy of this study is considered an acceptable loss.

2.1.3. Volume Grid Generation. The volume grid in this study was a 2-dimensional overset structured grid, generated with a NASA supplied software package called HYPGEN (Hyperbolic grid generator). Because of the bluntness of the selected airfoil trailing edge, a traditional 'C-grid', in which a wake surface boundary is intersected with the trailing edge of the airfoil and a volume grid is wrapped around the airfoil-wake surface, could not be used. Instead, an 'O-grid' was used, in which layers of grid points are 'grown' outward toward the trailing edge.

The volume grid was 'grown' or extrapolated outward from the airfoil surface in three layers. Because the key focus of this study is boundary layer development, special consideration is given to the region nearest the airfoil, here designated the 'viscous region' because it encompasses the boundary layer. In this region, the grid point distribution was linear, with an individual grid point spacing of 1×10^{-4}c. The viscous region featured 100 points, corresponding to a net region thickness of 0.01c.

The second region, designated the 'inner region,' featured 100 points, spaced nonlinearly, and a net thickness of 0.5c. Though the inner region is less densely populated than the viscous region, the velocity gradients here were observed to be very small, if not negligible, meaning that a sparser grid could be used without sacrificing numerical accuracy.

The third region, labeled 'outer region' was very sparsely populated, with 83 points spanning 10 chord lengths. This region primarily served as a buffer between the inner region and the far-field boundary. Velocity and pressure gradients were not readily visible in this region. A summary of the preceding information is given in table 2.1.

Table 2.1. Volume grid layer summary

Region	Points	Net Thickness	Spacing
L1 (viscous region)	100	0.01c	Linear
L2 (inner region)	100	0.50c	Nonlinear
L3 (outer region)	83	10.00c	Nonlinear
Total	283	10.51c	

2.2. FLOW-FIELD SOLUTION METHODOLOGY

2.2.1. Description of Flow Solver. Computational Fluid Dynamics (CFD) was the primary tool employed in this study. The flow solver used was a Reynolds-Averaged Navier Stokes (RANS) code called NASA OVERFLOW (OVERset grid FLOW solver). OVERFLOW was originally developed by NASA in the 1970s to simulate flow over the space shuttle, but was later modified to handle the low-speed subsonic flight regime [30]. OVERFLOW uses a first-order implicit time marching scheme to handle unsteady flows. More information about OVERFLOW is provided in the OVERFLOW manual [30].

2.2.2. Boundary Conditions. In the specified grid, four boundaries are present, as shown in Figure 2.3. These boundaries are the airfoil surface, the intersecting grid boundaries at the trailing edge of the airfoil, and the far-field boundary.

The airfoil surface is modeled as a viscous, adiabatic wall. The periodic boundary condition is applied to the intersect boundary. The free-stream/characteristic condition is applied to the far-field boundary, forcing a specified free-stream velocity and angle of attack. This information is summarized in table 2.2. One additional condition, planar symmetry, is applied in the Z-plane to assure 2-dimensional flow.

2.2.3. Turbulence Modeling. The RANS equations are time-averaged by definition. This results in several limitations of RANS codes such as OVERFLOW. Approximate and typically empirical turbulence models are required to accurately simulate time-steady characteristics where turbulent flow is present. In this study, the Spalart-Allmaras (SA) turbulent model was applied in the viscous regions of the flow. Furthermore, RANS alone cannot be used to predict turbulent transition. However, in this study, the laminar-to-turbulent transition itself is not investigated, but rather the

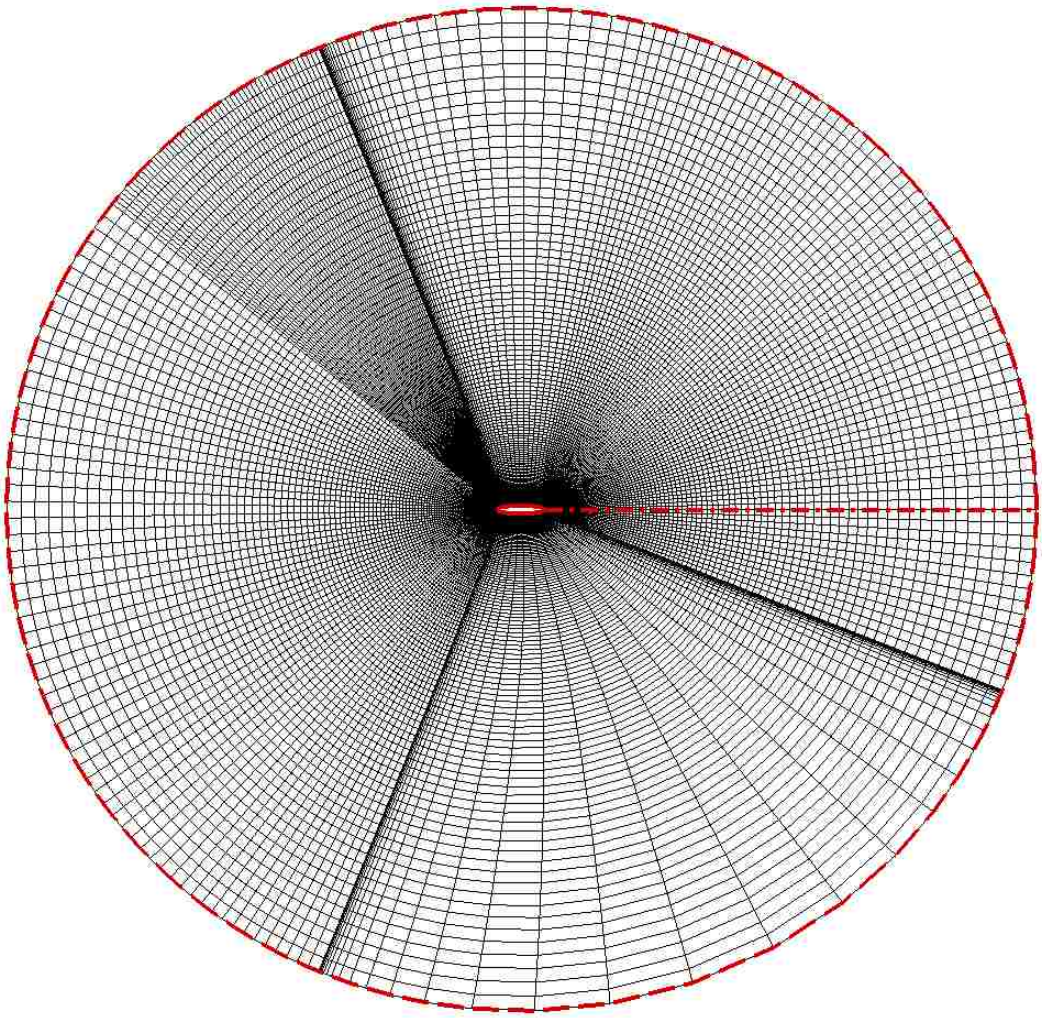

Figure 2.3. Grid boundaries (solid=airfoil surface, dash-dot=intersecting grid boundaries, dashed=far-field boundary)

Table 2.2. Summary of boundary conditions

Boundary	Specified Boundary Condition
Airfoil surface	Viscous, adiabatic wall
Grid Self-intersection	Periodic
Far-field	Characteristic/free-stream

influence that a control mechanism can have on the shape and size of the resultant LSB. Therefore, laminar flow was assumed from x/c = 0 to x/c = 0.1. Turbulent transition was

forced at x/c = 0.10, and fully turbulent boundary layer flow was assumed beyond x/c = 0.15. This modeling technique resulted in the formation of a stable LSB, as shown in Figure 1.1. Obviously, this technique is limited, insofar as it cannot predict the effect that an actuator might have on the turbulence transition mechanisms. However, as a demonstration of a control strategy designed to alter the pressure distribution over the airfoil, it is thought to be adequate.

2.2.4. Plasma Actuator Modeling. The actuator was modeled as a simple body force applied to a small region adjacent to the airfoil surface, as shown in Figure 2.4. To model this force, the OVERFLOW source code was modified to handle an additional right-hand side body force source term, incorporating a dimensionless quantity, f_{nd}, defined as

$$f_{nd} = \frac{f_d c}{\rho_\infty V_\infty^2}, \tag{1}$$

where f_d is the magnitude of the applied body force per unit volume, c is the airfoil chord, ρ_∞ is the free-stream density, and V_∞ is free-stream velocity. The space the body force occupied was designed to be the rough equivalent of that required by a plasma actuator. In this study, the body force was localized to a region 0.02c × 0.003c, with the body force applied in the x-direction, as shown in Figure 2.4.

Modeling a pulsed actuator was done by varying the frequency and duty cycle of the actuator pulse. Variations in body force magnitude due to the voltage change are ignored. Thus, the resultant applied waveform is a step, as shown in Figure 2.5.

2.2.5. Input Parameter Space. The free-stream conditions in this study are held constant. The free-stream Mach number is set to 0.01, ensuring negligible compressibility effects, and the Reynolds number is set to 1×10^5. The angle of attack α of the airfoil is held constant at 10 degrees. Free-stream turbulence intensity is 10

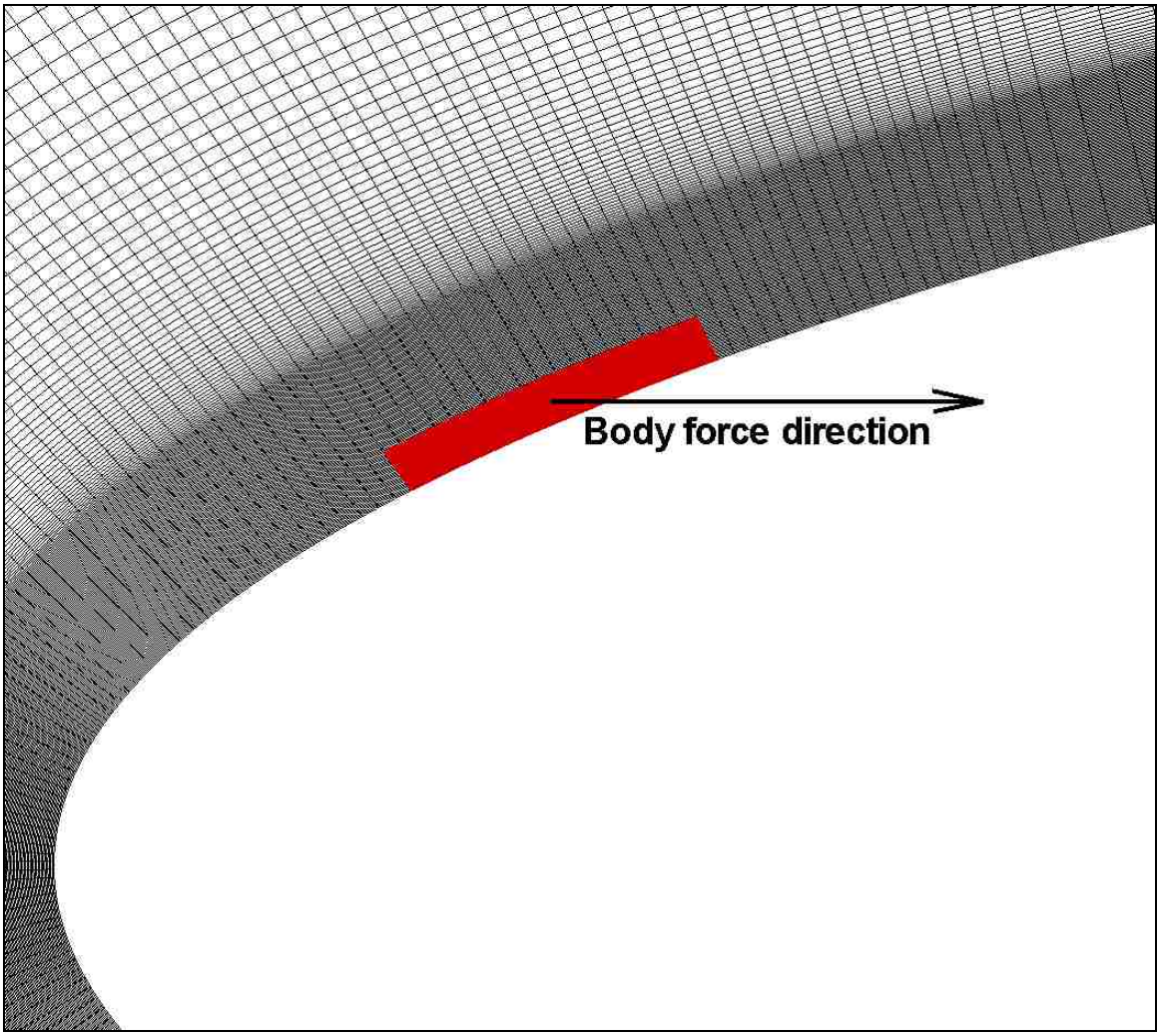

Figure 2.4. Body force location and direction

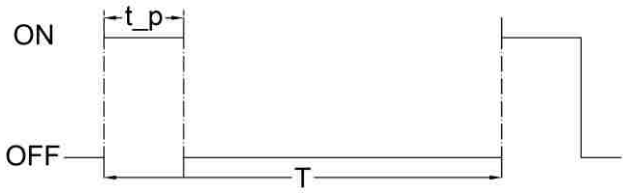

Figure 2.5. Example body force waveform

percent in all regions except where laminar flow is specified, near the leading edge of the airfoil. Other free-stream conditions are assumed to be those of air under standard sea-level conditions. This is summarized in table 2.3.

Table 2.3. Free-stream conditions

Condition	Set value
Mach Number (M_∞)	0.01
Reynolds Number (Re)	1×10^5
Angle of Attack (α)	10°
Turbulence Intensity	10%

The parameters of interest in this study are body force location, magnitude, frequency and duty cycle. The location of the leading edge of the actuator is varied between X_s = -0.005c and 0.028c, while the magnitude of the body force is varied between f_{nd}= 0 and 20. The duty cycle of the actuator is varied between 0 (no pulse) and 100% (steady state) while the pulse frequency is varied between f = 0.125 and 2.0 for selected conditions. This information is summarized in table 2.4.

Table 2.4. Investigated parameter space

Parameter	Selected Range		
X_s	-0.005c	to	0.028c
f_{nd}	0	to	20
D	0%	to	100%
f	0.125	to	2.000

2.2.6. Methodology Validation and Limitations. To this author's knowledge, no experimental data is available for the specific case under investigation (16% thick elliptical airfoil at α=10 deg., *Re* = 1.0e5). However, a limited amount of experimental data is available for similar cases.

A study by Choi [31] considers the aerodynamic characteristics of a 20% thick elliptical airfoil at a Reynolds number of 2.48e5-3.91e6, and presents computational results alongside with experimental. In this study, both the computational and experimental results presented indicate the presence of a leading edge LSB at angles of attack ranging from 8-15 degrees at Reynolds numbers ranging from 2.48e5 to 4.96e5. A study conducted prior to this work using identical methods to those in this study [6] predicted the formation of a LSB over a 16% thick elliptical airfoil at a 10 degree angle of attack over a Reynolds number range of 5.0e4 to 6.0e5. This is completely consistent with the range of Reynolds numbers under which LSBs were experimentally observed (2.48e5 was the lowest Reynolds number considered and the next highest was 1.24e6). While these data sets cannot be directly compared because of the slightly different airfoil geometries studied, the comparison nevertheless lends confidence to the work conducted in this study.

A more direct comparison can be made with the work of Kwon [32]. This study provides experimental data for a 16% thick elliptical airfoil at a Reynolds number of 3.0e5 and a range of angles of attack. Though no observation of a LSB was made in this study, it was noted by the authors that the methods used were incapable of detecting such phenomena. Cross-referencing this study with that previously mentioned using identical methodology, we find that they share a common data point within their respective parameter spaces. The lift and drag coefficients found by Kwon in this condition is compared to the numerical predictions in table 2.5.

As shown, the computational study underestimated the magnitudes of both force coefficients by approximately 20%. The reason for these discrepancies is not known with certainty, though several known issues may have contributed. Trailing edge separation of elliptical airfoils is inevitable due to their bluntness, and this separated region has a tremendous impact on the aerodynamic performance of the airfoil. Insufficient surface grid density over the aft portion of the airfoil may have prevented the flow solver from

Table 2.5. Comparison between experimental and computational force coefficients for 16% thick elliptic airfoil (α=10°, *Re*= 3.0e5)

Parameter	Kwon [32]	CFD	Error
C_l	~1.0	0.82	~18%
C_d	~0.04	0.032	~20%

accurately modeling this flow region. Additionally, the simple Spalart-Allmaras turbulence model, while capable of efficiently and accurately modeling attached boundary layers, is not well suited to predict flow separation. While this isn't an issue in modeling the LSB (the separation is laminar), it is important in predicting trailing edge separation. Although these issues may prevent highly accurate comparison with experimental results, the overarching goal of this study is not accurate performance prediction, but relative performance enhancement. These sacrifices in accuracy are considered acceptable, providing the computational results to be compared are equally handicapped.

On an analogous note, for the reasons listed above, steady and time-accurate solutions are not directly compared in this study. As will be seen, time-accurate solutions of un-actuated and steadily actuated cases were found to consistently produce slightly larger LSBs resulting in predictable differences of up to 11% in C_l and C_d even after the flow-field has reached equilibrium. The cause of this phenomenon is unknown, but comparison of the flow-fields showed no major discrepancies between the solutions generated by each method other than the one previously noted. However, because of this discrepancy, when comparing the effectiveness of pulsed and steady actuators, the pulsed actuator results are compared to time-accurate solutions with steady actuators run to equilibrium, rather than true time-steady solutions, to eliminate inadvertent numerical bias.

2.3. POST-PROCESSING

2.3.1. Quantitative Analysis. A variety of tools was used to extract and analyze data obtained from OVERFLOW. FOMOCO (FOrce and MOment Computation tools for Overset grids), a software package often bundled with OVERFLOW, was used to compute the force and moment coefficients of the airfoil under each obtained case. Plotting of the airfoil pressure distribution and pressure gradient distribution, as well as the determination of laminar separation and reattachment points were achieved with Tecplot 360™, a proprietary flow visualization software.

2.3.2. Qualitative Analysis. Tecplot 360™ was also used to conduct flow-visualization, which is essential to understanding the flow physics governing airfoil performance. Pressure and velocity contour plots, vector field plots, and streamline plots are produced and analyzed in this work.

3. RESULTS AND DISCUSSION: PARAMETRIC STUDY OF EFFECTS OF STEADILY OPERATED ACTUATOR ON LSB AND AIRFOIL PERFORMANCE

3.1. NOMENCLATURE USED IN PROCEEDING ANALYSIS

To better represent the obtained results, a new coordinate system is defined. The location of the leading edge of the actuator is used as the X-axis variable in the following analysis, as indicated in Figure 3.1. As shown, X_s is defined as the location of the leading edge of the actuator with respect to the laminar separation point of the control case. This schematic also shows the direction of the applied body force.

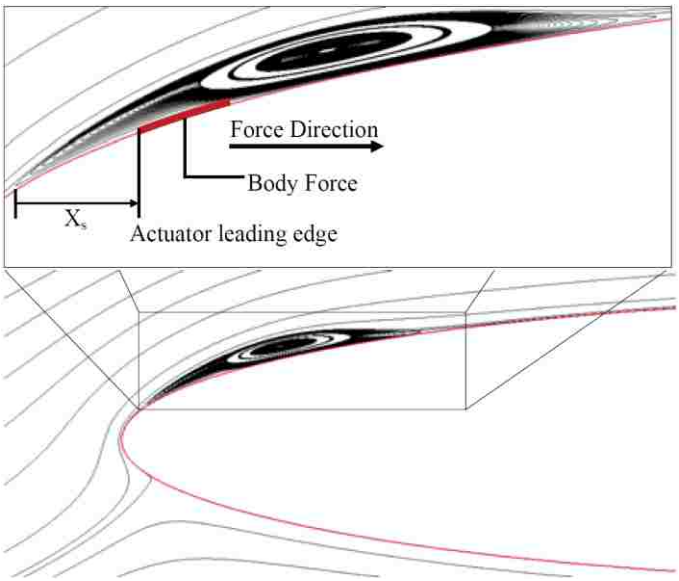

Figure 3.1. Coordinate system used in analysis

3.2. QUALITATIVE INVESTIGATION OF EFFECTS OF ACTUATOR ON LSB CHARACTERISTICS

Figure 3.2 shows the effect of the body force magnitude and location on the LSB and airfoil lift to drag ratio. This figure is organized into three rows. The top row shows

the reference case, where no actuator was applied. The center and bottom rows show the effects of actuator placement on LSB development for actuator strengths f_{nd} = 10 and 20, respectively. In frames d through i, the actuator location is indicated with a pale highlight.

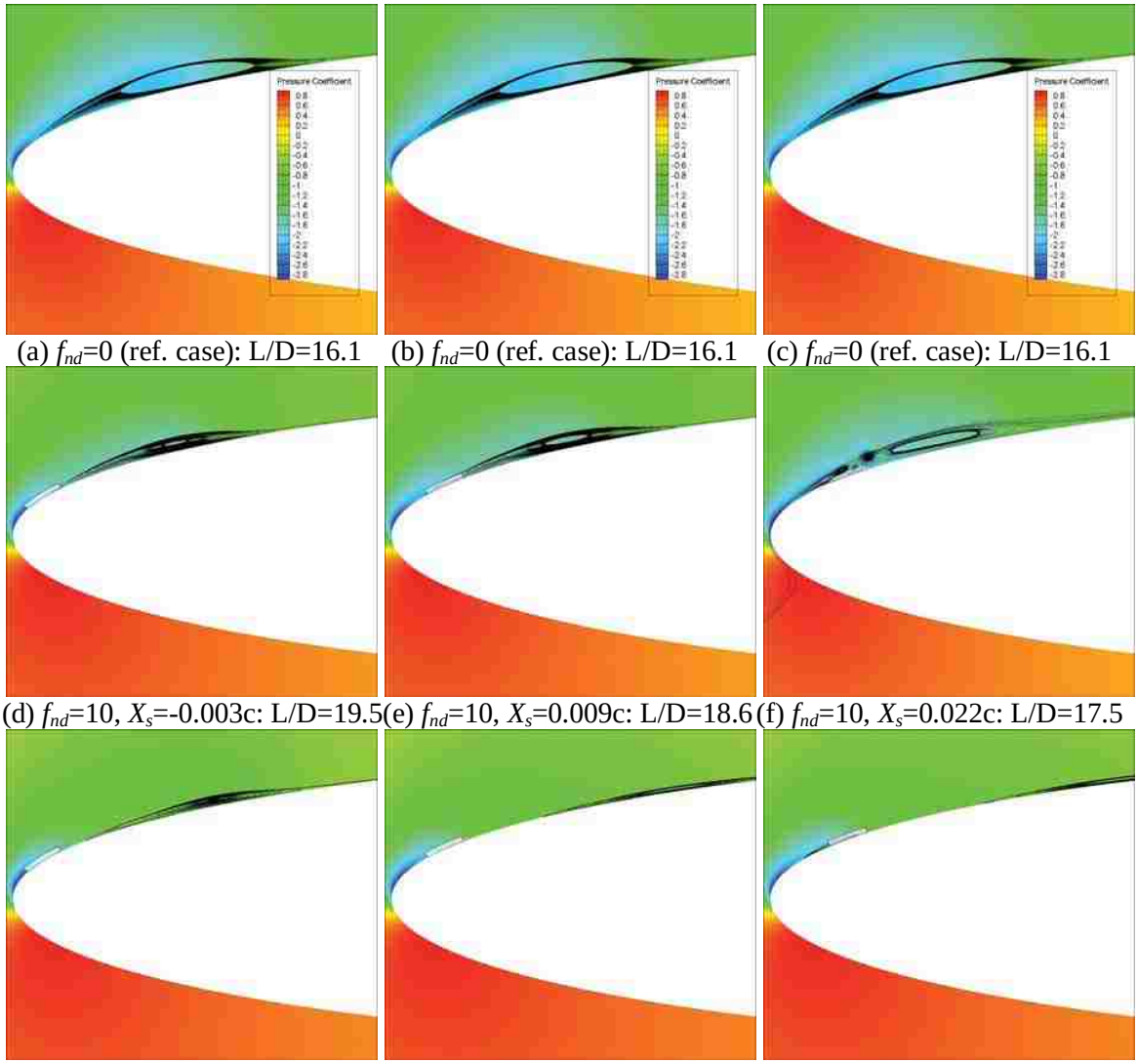

(a) f_{nd}=0 (ref. case): L/D=16.1 (b) f_{nd}=0 (ref. case): L/D=16.1 (c) f_{nd}=0 (ref. case): L/D=16.1

(d) f_{nd}=10, X_s=-0.003c: L/D=19.5 (e) f_{nd}=10, X_s=0.009c: L/D=18.6 (f) f_{nd}=10, X_s=0.022c: L/D=17.5

(g) f_{nd}=20, X_s=-0.003c: L/D=23.5 (h) f_{nd}=20, X_s=0.009c: L/D=25.8 (i) f_{nd}=20, X_s=0.022c: L/D=25.3

Figure 3.2. Influence of actuator strength and location on LSB development and corresponding lift-to-drag ratio

As shown, when placed upstream of the nominal separation point (X_s = -0.003), the actuator has the effect of shrinking the LSB in all dimensions. As the actuator is moved 0.009 *c* downstream of the separation point, the same effect is observed, but to a lesser effect in the f_{nd} = 10 case. In the f_{nd} = 20 case, the LSB appears to have been simultaneously "squeezed" to the airfoil surface and "stretched" laterally. The laminar separation point is clearly shifted downstream from the nominal location. As observed for f_{nd} = 10, as the actuator is moved further downstream to X_s = 0.022 *c*, it causes additional flow complexity in the form of an LSB breakup. As shown in

Figure 3.2.f, two smaller clockwise rotating bubbles are clearly visible upstream of the primary one, which interact to induce secondary counter-clockwise rotation. Here, the effective airfoil shape does not appear to have been significantly altered with respect to that of the reference case. As shown in

Figure 3.2.i, for f_{nd} = 20, as the actuator is shifted to X_s = 0.022 *c*, the LSB is merely shifted and stretched further downstream. However, a secondary separation point has formed upstream of the actuator, near the nominal separation point. From this information, it would appear that moving the actuator too far downstream of the laminar separation point results in the reformation of the LSB upstream of the actuator.

Figure 3.2 also shows a correlation between LSB size reduction and airfoil aerodynamic performance. As indicated, the cases in which the LSB size is reduced most tend to yield higher lift-to-drag ratios than their counterparts. This correlation is discussed in greater detail in 3.3 and 3.4.

Figure 3.3 through Figure 3.5 give the computed pressure coefficient distribution of the airfoil over the upper leading edge of the airfoil for various force magnitudes at given actuator locations. Each figure contains two plots: one conventionally plotting the pressure coefficient against X_s, and a second plotting C_p against *y*. The C_p *vs. Y* plots are relevant to this analysis because they can be integrated to find the net pressure drag over the airfoil, just as C_p vs. *x* plots can be integrated to determine lift. The location of the LSB in each case roughly corresponds to the location of the secondary suction peak located downstream of the airfoil's natural peak. The reason that LSBs tend to reduce aerodynamic efficiency is their tendency to degrade the natural suction peak of the airfoil. The most significant consequence of this increase in pressure over the leading edge of the

airfoil is a dramatic increase in pressure drag. In extreme cases, it can also reduce the lift generated by the airfoil [6]. It follows, then, that airfoil performance can be enhanced by restoring the "natural" suction peak of the airfoil. As shown in Figure 3.3 through Figure 3.5, regardless of actuator location, as the magnitude of the body force is increased, the primary suction peak of the airfoil becomes more pronounced. This is the physical mechanism responsible for the improvement in the aerodynamic efficiency of the airfoil. The greatest improvement is shown in Figure 3.4 with f_{nd} = 20. As shown, in this case the suction peak associated with the LSB has effectively vanished, and the natural suction peak has been restored. Not coincidentally, this case corresponded to the greatest improvements seen in the lift-to-drag ratio of the airfoil. Of special note in Figure 3.5 is the existence of multiple distinct pressure peaks for all but one of the cases. This is the result of the LSB breakup previously mentioned, wherein multiple distinct bubbles are observed.

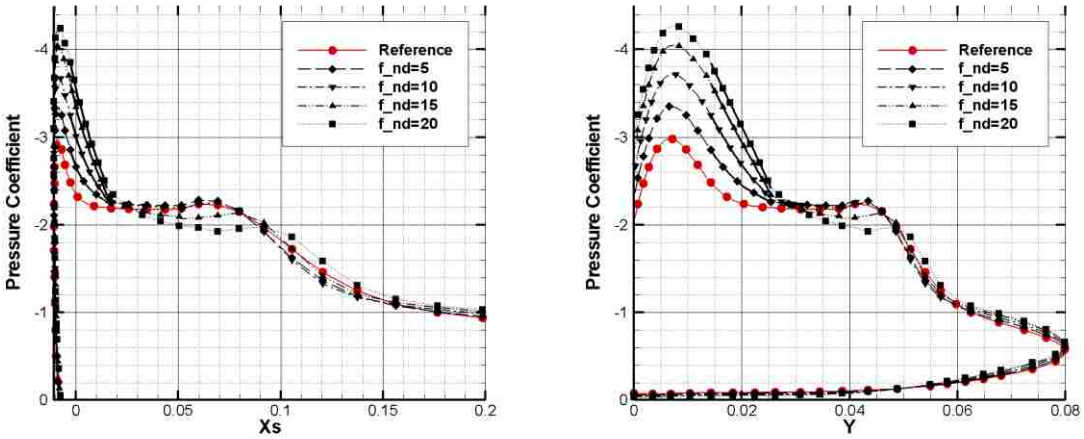

(a) C_p vs. X_s (b) C_p *vs. Y*

Figure 3.3. Influence of actuator strength on pressure distribution over upper leading edge of airfoil (X_s = -0.003c)

For convenience, Figure 3.6 and Figure 3.7 are provided, complementing the data shown in Figure 3.3 through Figure 3.5. Figure 3.6 and Figure 3.7 show the effect of moving the actuator downstream for two force magnitudes. As shown, the optimal

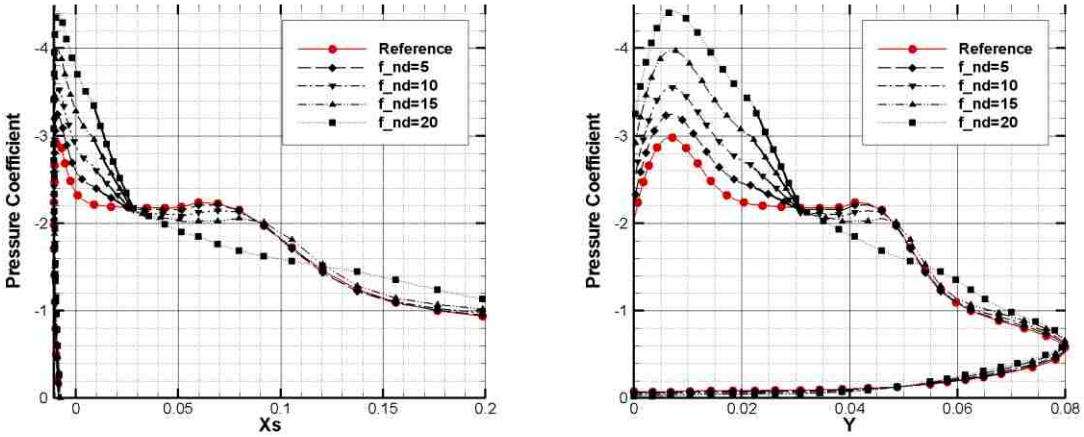

(a) C_p vs. X_s (b) C_p *vs. Y*

Figure 3.4. Influence of actuator strength on pressure distribution over upper leading edge of airfoil (X_s = 0.009c)

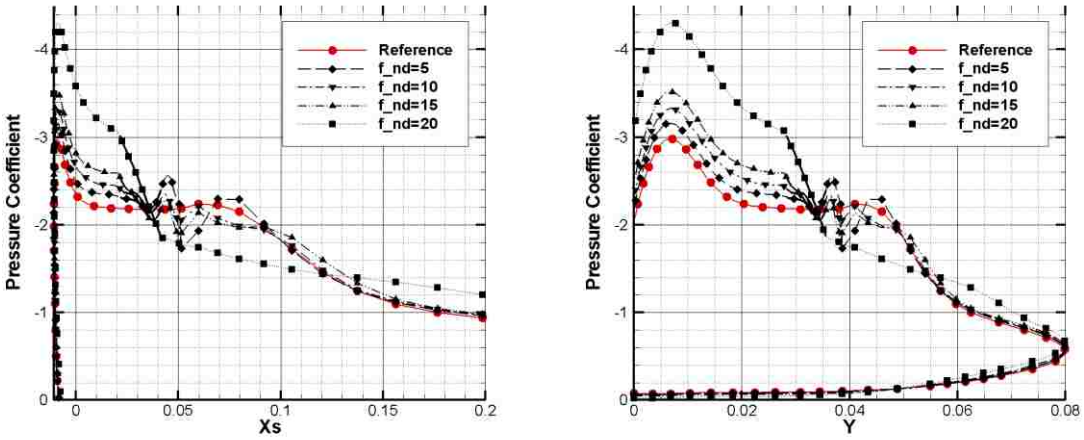

(a) C_p vs. X_s (b) C_p *vs. Y*

Figure 3.5. Influence of actuator strength on pressure distribution over upper leading edge of airfoil (X_s = 0.022c)

location of the actuator with respect to pressure peak restoration is dependent upon force magnitude. This is consistent with the observations previously made with respect to the LSB size and airfoil lift to drag ratio.

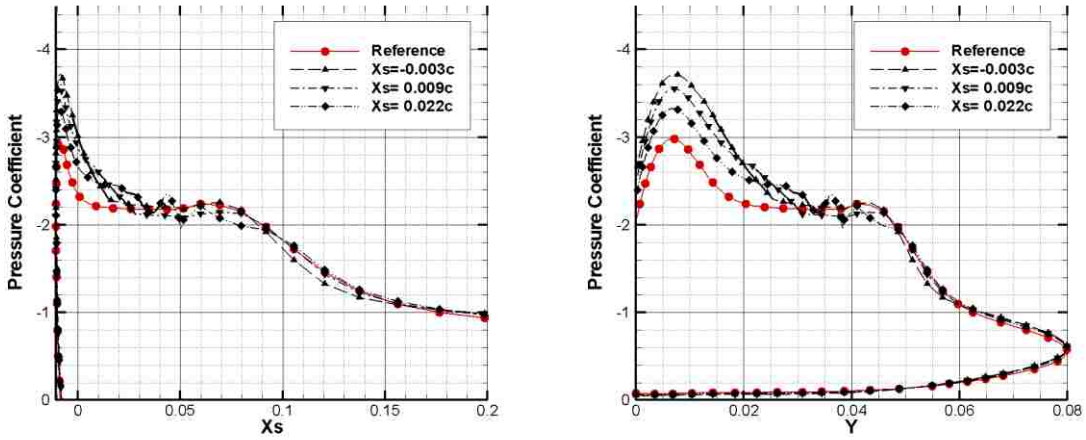

(a) C_p vs. X_s (b) C_p *vs. Y*

Figure 3.6. Influence of actuator location on pressure distribution over upper leading edge of airfoil (f_{nd} = 10)

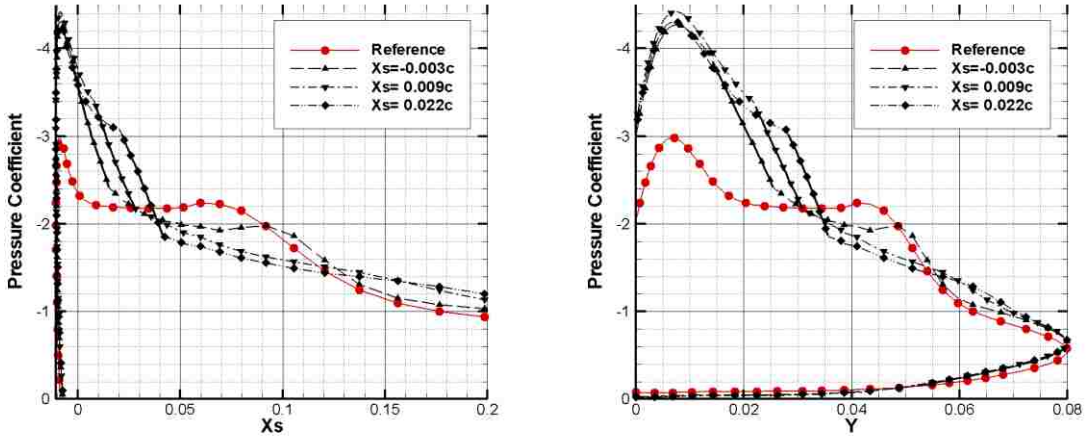

(a) C_p vs. X_s (b) C_p *vs. Y*

Figure 3.7. Influence of actuator location on pressure distribution over upper leading edge of airfoil (f_{nd} = 20)

3.3. DEPENDENCE OF LSB SIZE ON ACTUATOR STRENGTH AND POSITION

In order to quantitatively examine the relationship between the actuator strength/position and the size of the bubble, and thus the change in the effective airfoil shape, a new parameter was defined. The comparative area plotted in Figure 3.8 is simply the product of the chord-wise length of the bubble and the height of the center of rotation with respect to the airfoil surface. It is merely a means of comparing solutions, and should not be treated as a direct measure of the area of the LSB. Figure 3.8 shows the dependence of the comparative area of the LSB on actuator position, for f_{nd} magnitudes of 0, 5, 10, 15, and 20.

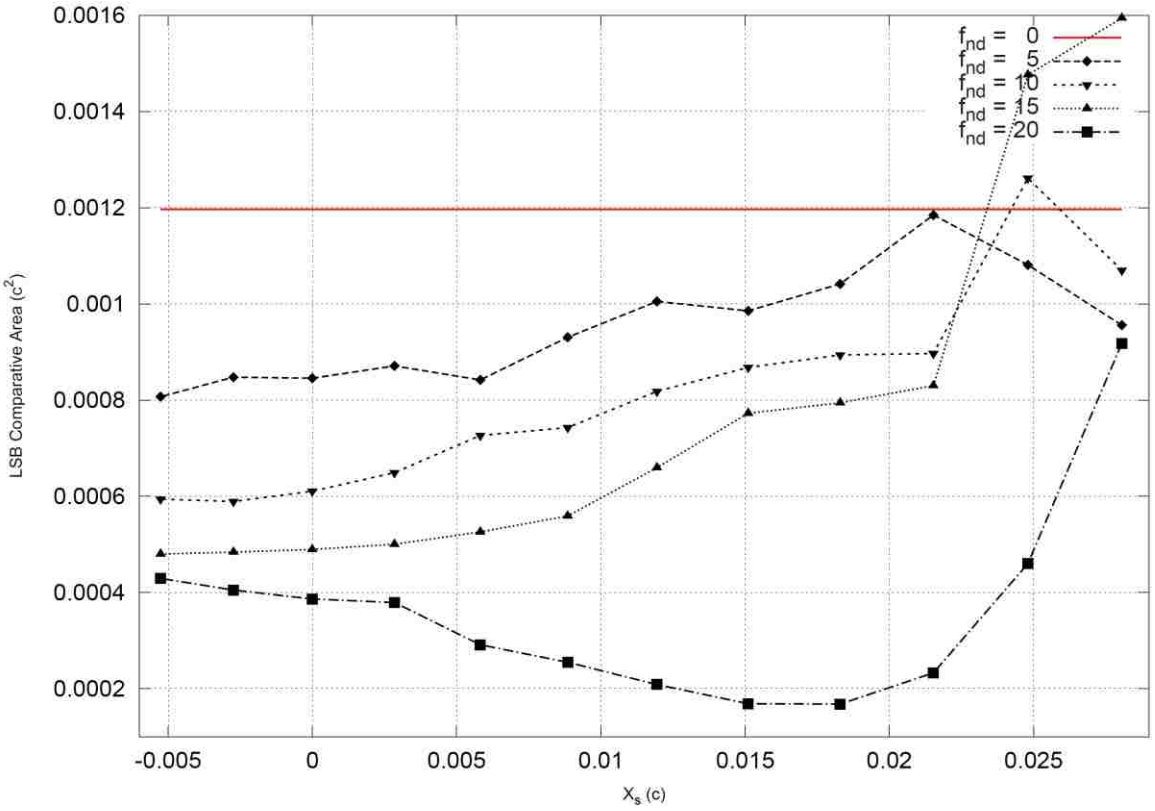

Figure 3.8. Influence of actuator location and strength on LSB size

As shown in Figure 3.8, it was found that increasing the body force magnitude generally reduced the size of the LSB. This is in agreement with intuition, as a body force applied in the direction of the fluid motion would be expected to counteract the adverse pressure gradient responsible for the initial flow separation. It was found that for f_{nd}s of 5, 10, and 15, the location of the actuator which resulted in minimum LSB size was upstream of the nominal leading edge of the LSB. For each of these cases, optimal actuator performance was observed to occur when the actuator was "straddling" the LSB separation point, with the actuator leading edge upstream of the separation point, and the trailing edge downstream. However, for f_{nd} = 20, the optimal actuator location was found to be roughly 0.017 *c* downstream of the LSB separation point. This discrepancy was unexpected. It may be the case that the larger force magnitude had a strong enough upstream influence to achieve the desirous effect seen in the other cases, and that downstream placement had a greater effect on the rest of the bubble. However, more research is required to confirm this hypothesis. It may also be the case that the discrepancy was the result of error associated with the crudeness of the method to determine LSB area. However this suggestion would seem to be partially discredited by the airfoil performance data given in 3.4. The trends described in this section break down as the actuator leading edge is moved roughly 0.2 *c* downstream of the LSB separation point for the f_{nd} = 5, 10, and 15 cases, as shown in Figure 3.8. This phenomenon is the result of actuator-induced flow-field complexity, more fully discussed in 3.5.

3.4. DEPENDENCE OF AIRFOIL AERODYNAMIC PERFORMANCE ON ACTUATOR STRENGTH AND POSITION

Figure 3.9 gives the lift to drag ratio of the airfoil versus actuator location for various force magnitudes. As shown, the actuator location corresponding to peak aerodynamic efficiency is not constant with respect to f_{nd}. For f_{nd} = 5 and 10, the optimal actuator leading edge location is slightly upstream of the nominal LSB leading edge. For the f_{nd} = 15 case, optimal efficiency occurs when the actuator is placed 0.005 *c* downstream of the separation point, and for the f_{nd} = 20 case, this occurs at approximately 0.013 *c*. It was found that for an f_{nd} of 5, the lift to drag ratio of the airfoil could be

improved by 8.1 percent at X_s = -0.0027 c (0.0027 c upstream of the separation point). For f_{nd} = 10, the lift to drag ratio could be increased by 21.8 percent at X_s = 0. At f_{nd} = 15, the lift to drag ratio could be improved by 39.8 percent at X_s = 0.0028 c. At f_{nd} = 20, the lift to drag ratio was found to improve by 61.2 percent to 25.9 at X_s = 0.0119 c.

Although the optimal locations of the actuator with respect to the LSB area and airfoil efficiency are not identical, it is apparent from the data that the shrinking or elimination of the LSB generally corresponds to improvements in aerodynamic efficiency. Comparing the case whereby the maximum performance enhancement was attained to the reference case, this trend becomes apparent. Under the maximum performance case, the actuator effectively eliminates the LSB, as shown in Figure 3.10, which compares that case to the control case.

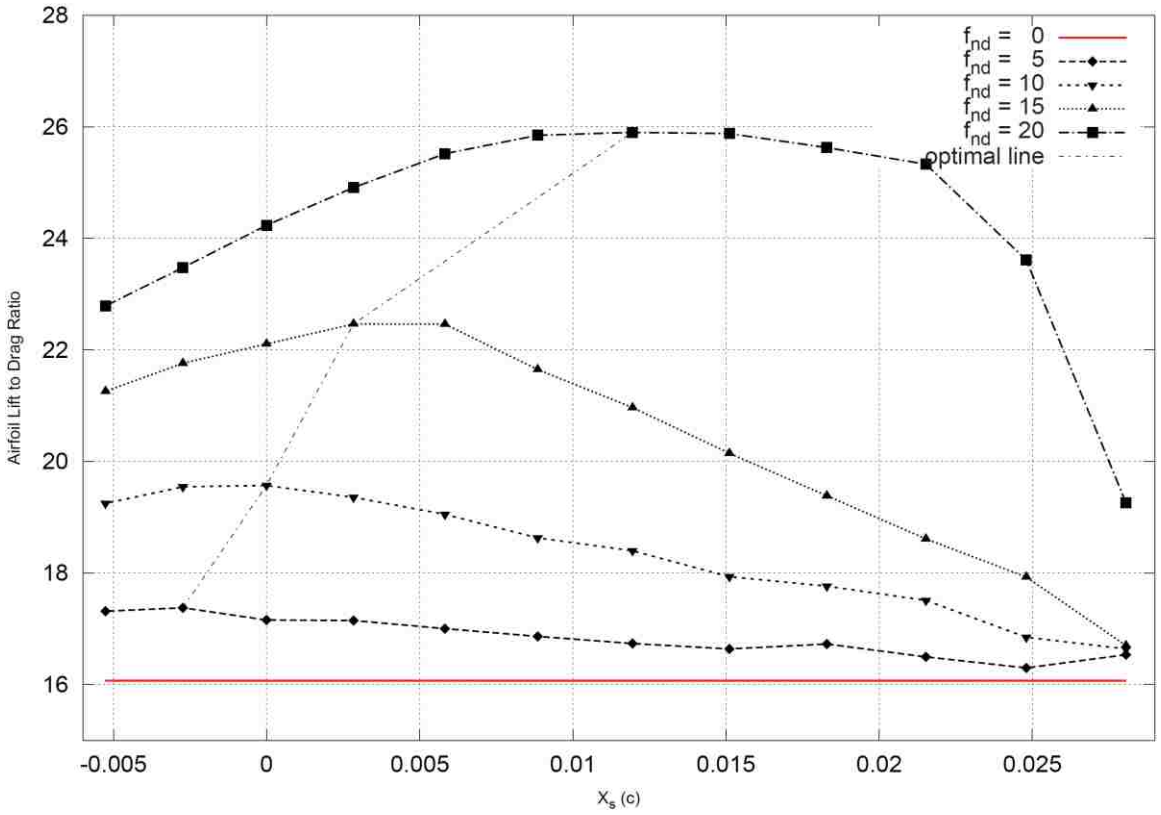

Figure 3.9. Dependence of airfoil lift-to-drag ratio on actuator strength and location

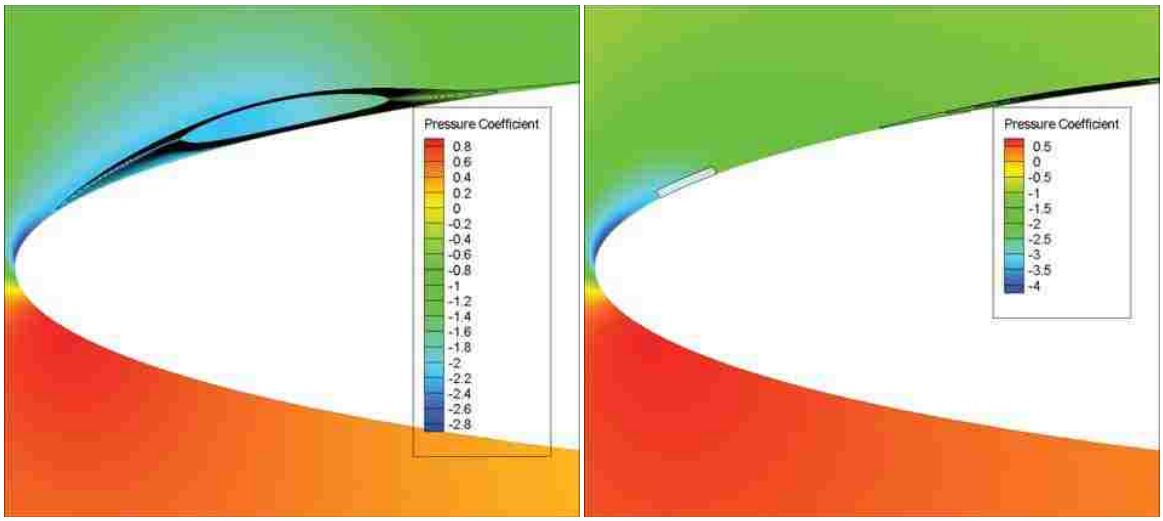

(a) f_{nd}=0 (ref. case) (b) f_{nd}=20, X_s=0.0119

Figure 3.10. Comparison between stream-traces and pressure coefficient contour plots for control and optimal performance case

The lift and drag coefficients obtained from this solution were 0.9591 and 0.0370, corresponding to a lift to drag ratio of 25.90. By comparison, in the reference case, the airfoil had a lift coefficient of 0.8486, a drag coefficient of 0.0528, and a lift to drag ratio of 16.08. The actuator had the effect of increasing the lift of the airfoil by 13 percent over the nominal case, and reducing the drag by 30 percent, improving the lift to drag ratio by 61 percent. Presumably, this boost in lift can be explained by the actuator induced acceleration of the flow over the upper surface of the airfoil. The drag reduction can be explained by the restoration of the leading edge suction peak of the airfoil, as previously established.

As a second actuator performance barometer, a high Reynolds number case, under which an LSB is not observed, can be examined. Here, a case identical to the control case, but with a Reynolds number of 2 million is observed. The lift coefficient, drag coefficient, and lift-to-drag ratio of this case are computed to be 0.7530, 0.0256, and 29.44, respectively. As Figure 3.11 shows, the actuator has the effect of restoring the pressure distribution over the leading edge of the airfoil to something roughly similar to that attained at a Reynolds number of 2 million without an actuator. In fact, the leading edge suction peak of the optimized case is superior to that observed at higher Reynolds numbers. Compared with the high Reynolds number case, the optimal solution featured

27 percent greater lift, and 45 percent greater drag (compared with the 106 percent increase in drag associated with reference case). The lift to drag ratio was merely 12 percent lower than that attained at a Reynolds number of 2 million. The actuator has the effect of marginally increasing the lift of the airfoil (already inflated due to the low Reynolds number), while drastically reducing the drag associated with the LSB.

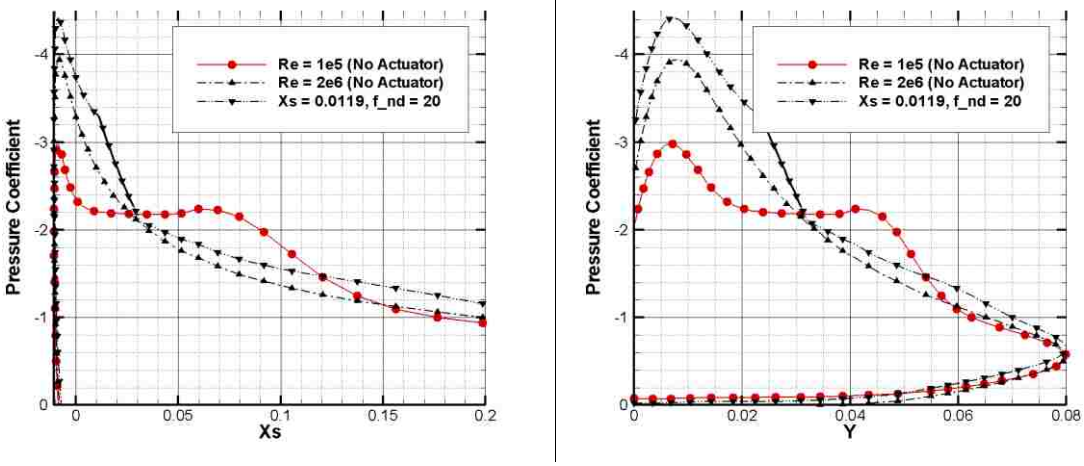

(a) C_p vs. X_s (b) C_p *vs. Y*

Figure 3.11. Comparison between pressure distributions of optimal performance case and control case with *Re* = 2 million

3.5. OBSERVATION OF ACTUATOR INDUCED LSB BREAKUP AND INSTABILITY

As previously mentioned, erratic LSB behavior is observed as the actuator is moved significantly downstream of the laminar separation point. This appears to be the result of an LSB breakup induced by the actuator. As shown in Figure 3.12, as the actuator is progressively shifted downstream of the nominal separation point, additional clockwise circulatory regions appear upstream of the primary LSB core. These separate circulations ultimately interact, inducing secondary counter-rotational flow between them. This behavior results in progressively increasing flow-field complexity, rendering the applied method of measuring LSB size inadequate, and ultimately resulting in flow-field instability. This behavior was noted in each of the f_{nd} = 5, 10, and 15 cases. As

suggested, the stability of the LSB is highly sensitive to the location of the actuator, when located downstream of the laminar separation point.

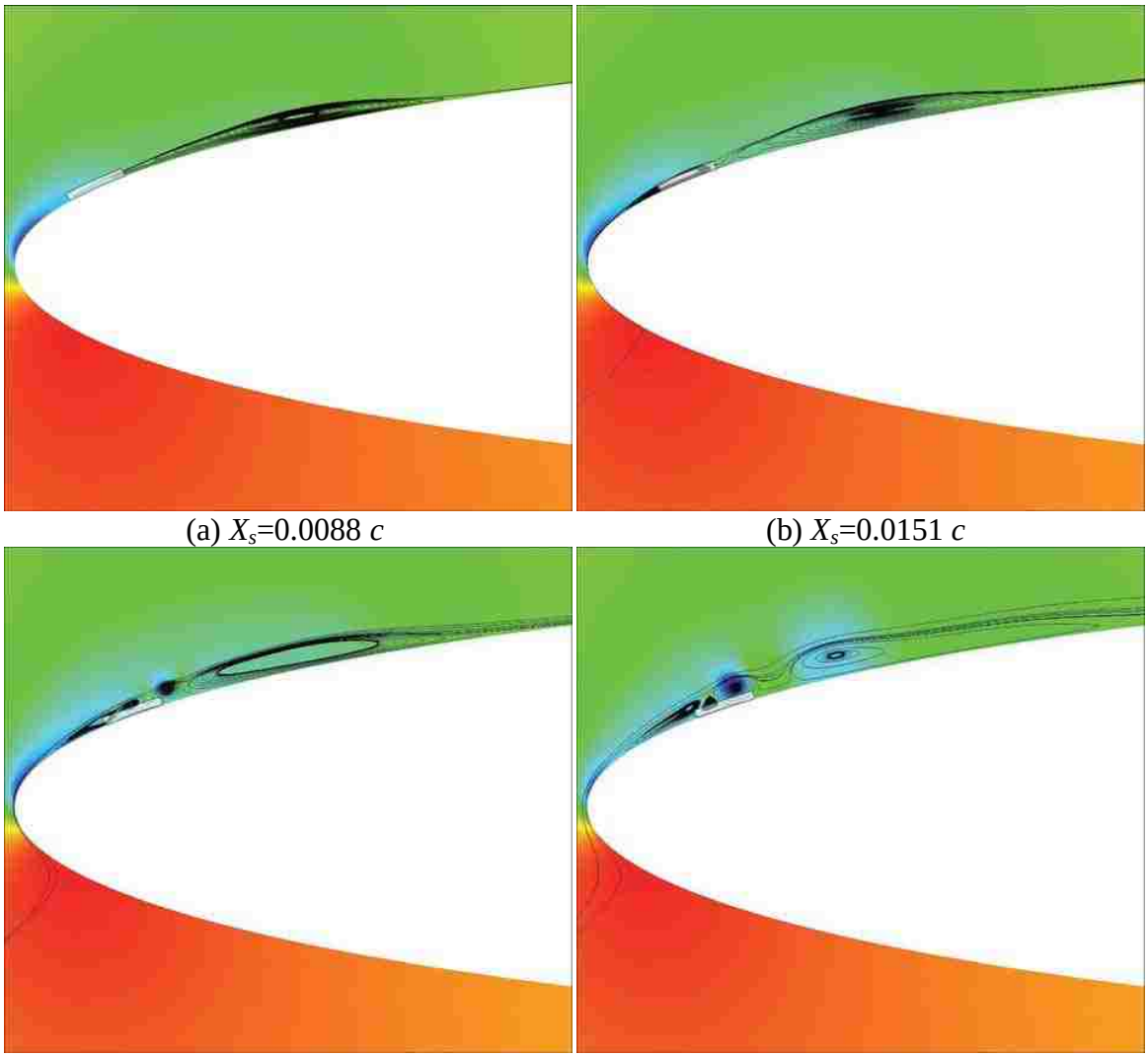

(a) X_s=0.0088 c (b) X_s=0.0151 c

(c) X_s=0.0215 c (d) X_s=0.0281 c

Figure 3.12. Evolution of LSB structure as actuator is shifted downstream of nominal separation point (f_{nd}=15)

4. RESULTS AND DISCUSSION: PARAMETRIC STUDY OF EFFECTS OF PULSED ACTUATOR ON LSB AND AIRFOIL PERFORMANCE

The purpose of this analysis is to investigate the effects of 'pulsing' an actuator on the LSB flow structure and the corresponding effects on airfoil aerodynamic performance. In this analysis, the actuator is pulsed at various frequencies and duty cycles, while the magnitude of the applied dimensionless body force f_{nd} is held constant at 20. The overarching goal of this portion of the study is to determine whether pulsing an actuator can result in any performance enhancement with respect to a steadily operated device.

4.1. QUALITATIVE INVESTIGATION OF ACTUATOR INDUCED UNSTEADY EFFECTS

Streamline and pressure coefficient plots are examined at various time intervals to develop a conceptual understanding of the unsteady flow physics resulting from pulsed actuation and how those physics relate to the aerodynamic performance of the airfoil.

To understand the quasi-steady state aerodynamic behavior exhibited by the airfoil, it is necessary to understand the unsteady flow developments over the course of a single actuation period. Figure 4.1, Figure 4.4, Figure 4.6, and Figure 4.8 are streamline distribution and pressure coefficient contour plots showing the flow developments present at specific points within the actuation period for a non-dimensional frequency of 2.0 and duty cycles ranging from 20 to 80 percent. The 'snapshots' shown in each figure were taken after the initial transient response of the flow-field to the actuator had dissipated, and the lift and drag of the airfoil had reached quasi-equilibrium. Figure 4.3, Figure 4.5, Figure 4.7, and Figure 4.9 show the time-dependent airfoil pressure distributions over the upper leading edge region of the airfoil corresponding to Figure 4.1, Figure 4.4, Figure 4.6, and Figure 4.8.

4.1.1. f = 2.0 case. Figure 4.1 shows the periodic flow-field developments corresponding to a frequency f of 2.0 and a 20 percent duty cycle, once the flow-field has reached a quasi-equilibrium state. Frame (a) corresponds to the snapshot in time directly

preceding the actuator pulse. Frames (b) through (f) show the response of the flow field up to the point of the next actuator pulse in dimensionless time increments of 0.1. Because the dimensionless actuation period T corresponding to f=2.0 is 0.5, frame (f) also corresponds to the instance in time directly preceding the following actuator pulse.

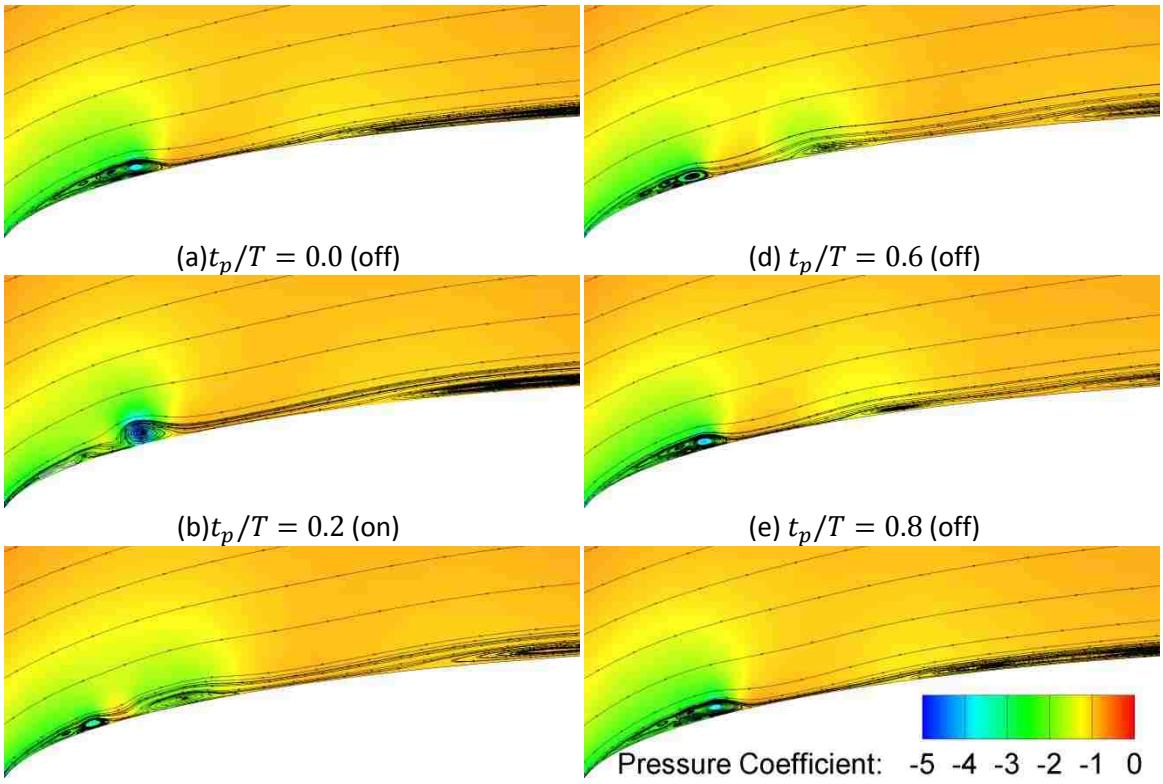

Figure 4.1. Pressure coefficient contour and streamline distributions over 1 duty cycle (f=2.0, D=0.2)

As shown in frame (b), the LSB has been "split" into three distinct bubbles, a small, "flat" bubble separating upstream of the actuator and reattaching between the leading and trailing edges of the actuator, a smaller bubble just downstream of the actuator trailing edge, and a taller, better developed bubble further downstream of the actuator trailing edge. All three bubbles rotate clockwise. Also shown in Figure 4.1 is the leading edge of a fourth bubble located far downstream of the actuator, which does not noticeably change with time. As shown, there is a very pronounced low pressure

peak associated with the third bubble (as indicated by the blue color), and a smaller peak associated with the second. As time progresses, several trends are observed. The second bubble is observed to quickly grow, eventually merging with the first bubble, and forming an increasingly strong suction peak, as indicated in frames (b) through (e). As time progresses, the leading edge bubble extends further downstream, more closely resembling the steady-state reference solution, as expected. The previously mentioned third bubble is observed to propagate downstream with time. The bubble is observed to "flatten" and the pressure peak is shown to dissipate. Ultimately, the bubble merges with the fourth downstream bubble, strengthening it, as shown in frame (f). It is noted that the apparently stable fourth bubble was found to be present in all *f*=2.0 cases, but never in the lower frequency cases. As will be shown later, this bubble does not seem to have an appreciable effect on the aerodynamic performance of the airfoil.

Figure 4.2 shows the effects of the actuator on the airfoil surface pressure distribution over the course of a single actuation period. As shown, directly following the actuator pulse (t_p/T = 0.2), there are three low pressure peaks over the leading edge of the airfoil: the natural suction peak of the airfoil (*x/c* = 0), that corresponding to the previously mentioned second bubble near the trailing edge of the actuator (*x/c* = 0.05), and that of the third and most developed bubble (*x/c* = 0.08). As shown, the natural suction peak pressure coefficient reaches approximately -3.4, and remains relatively constant with time. This is a modest improvement over the reference natural peak of -3.0. The second peak magnifies with time, and shifts slowly downstream. As shown, from t_p/T = 0.2 to t_p/T = 1.0, the peak shifts from *x/c* = 0.05 to *x/c* = 0.07, while the pressure coefficient decreases from -2.2 to approximately -3.5. It is fairly clear from Figure 4.3 that the actuator pulse results in further enhancement of this peak to -4.2, where it transitions to the third pressure peak, while another peak forms at *x/c* = 0.05 to replace the second. After the pulse, the third peak quickly dissipates and moves downstream with the previously mentioned third bubble. As shown, from t_p/T = 0.2 to t_p/T = 0.4, this pressure coefficient of this peak increases dramatically from -4.2 to -2.0, while shifting downstream from *x/c* = 0.08 to 0.1. From this point, the peak continues to dissipate and move downstream until the third and fourth bubbles merge at t_p/T = 1.0.

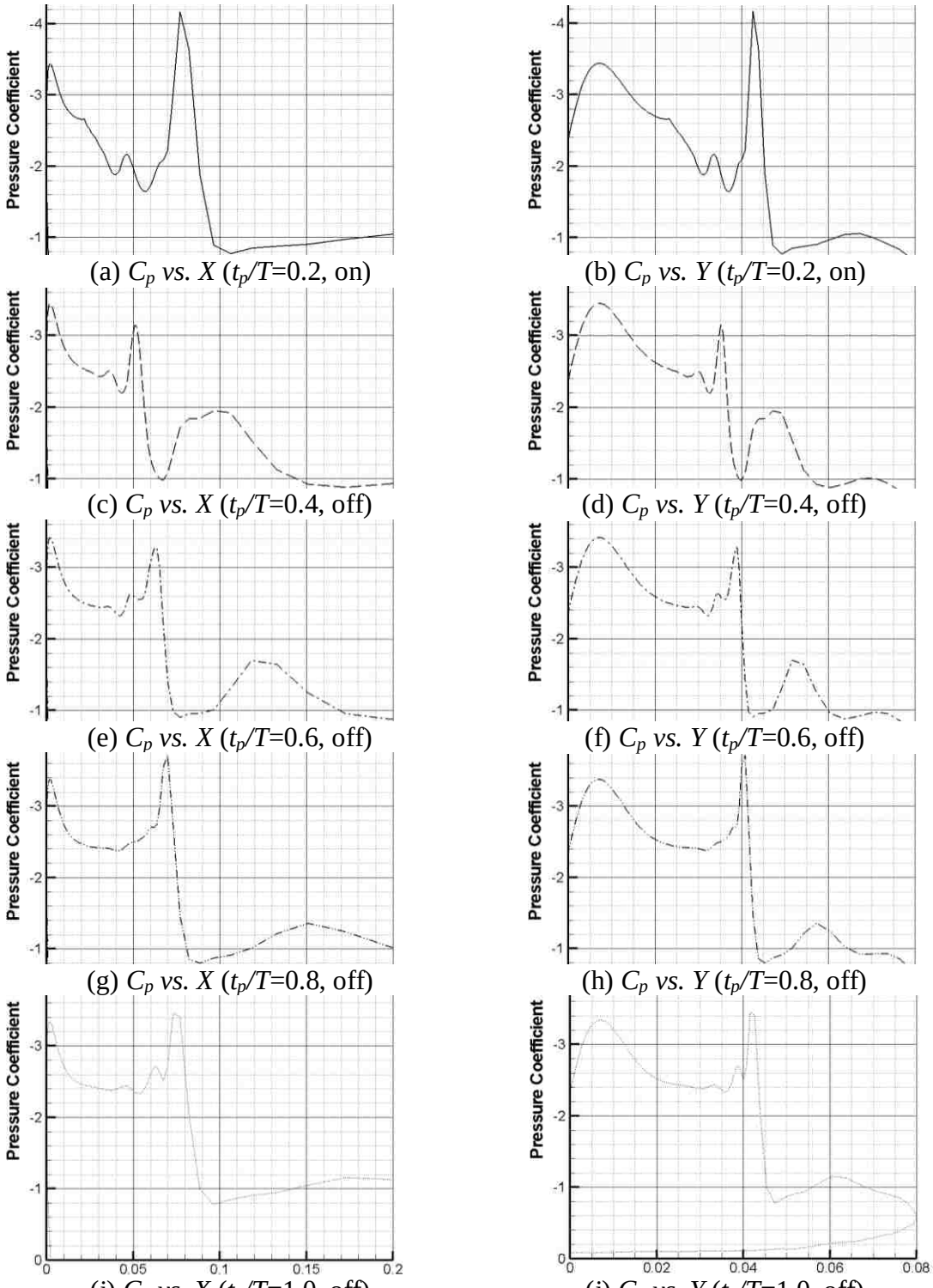

(a) C_p *vs. X* (t_p/T=0.2, on) (b) C_p *vs. Y* (t_p/T=0.2, on)

(c) C_p *vs. X* (t_p/T=0.4, off) (d) C_p *vs. Y* (t_p/T=0.4, off)

(e) C_p *vs. X* (t_p/T=0.6, off) (f) C_p *vs. Y* (t_p/T=0.6, off)

(g) C_p *vs. X* (t_p/T=0.8, off) (h) C_p *vs. Y* (t_p/T=0.8, off)

(i) C_p *vs. X* (t_p/T=1.0, off) (j) C_p *vs. Y* (t_p/T=1.0, off)

Figure 4.2. Influence of pulsed actuator on airfoil pressure distribution (f=2.0, D=0.2)

Figure 4.3 compresses the data from Figure 4.2 into single C_p vs. X and C_p vs. Y plots. To save space, all following pressure distribution data will be presented in this fashion.

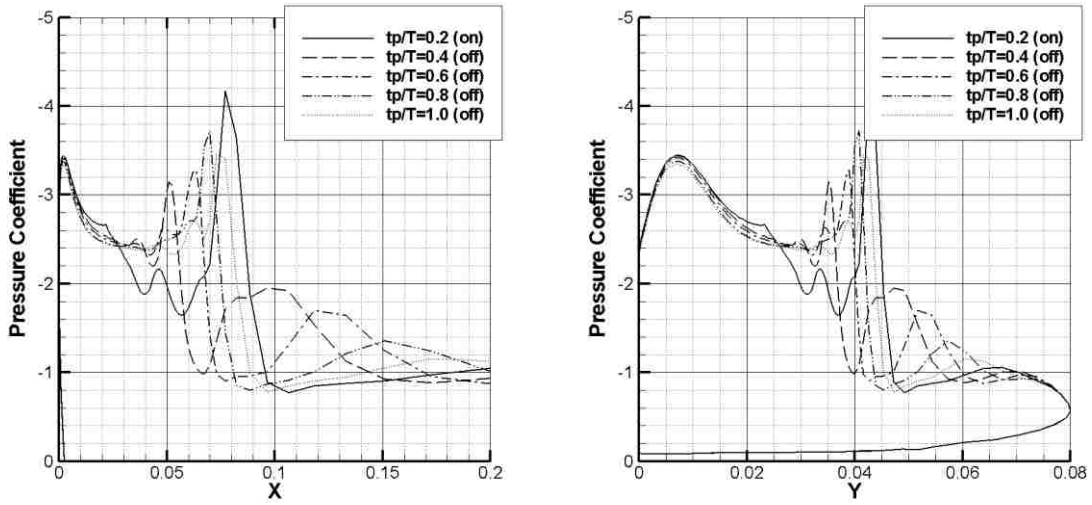

(a) C_p *vs.* X (b) C_p *vs.* Y

Figure 4.3. Influence of pulsed actuator on airfoil pressure distribution (f=2.0, D=0.2)

Figure 4.4 shows the flow-field developments corresponding to f=2.0 and D = 0.4. As shown, the flow developments over the course of an actuation period are slightly different than those seen in the D = 0.2 case. As shown, at t_p/T = 0.2, three clockwise circulation cores are observed near the leading edge of the airfoil, and a sharp pressure peak is observed near the third bubble. Whereas in the D = 0.2 case in which the first and second bubbles are found to merge, in this case, mergence of the second and third bubbles is observed as time progresses, leaving only two circulation cores. Once this mergence has occurred, the flow behaves similarly to that of the t_p/T = 0.2 case. Notably, the third bubble begins dissipating before the actuator is turned "off" (t_p/T = 0.4), indicating that the behavior of the third bubble is not *directly* driven by the actuator, but is rather the natural fluid response of the second bubble (which is generated during each pulse as a result of a break-up of the first), as it transitions into "becoming" the third.

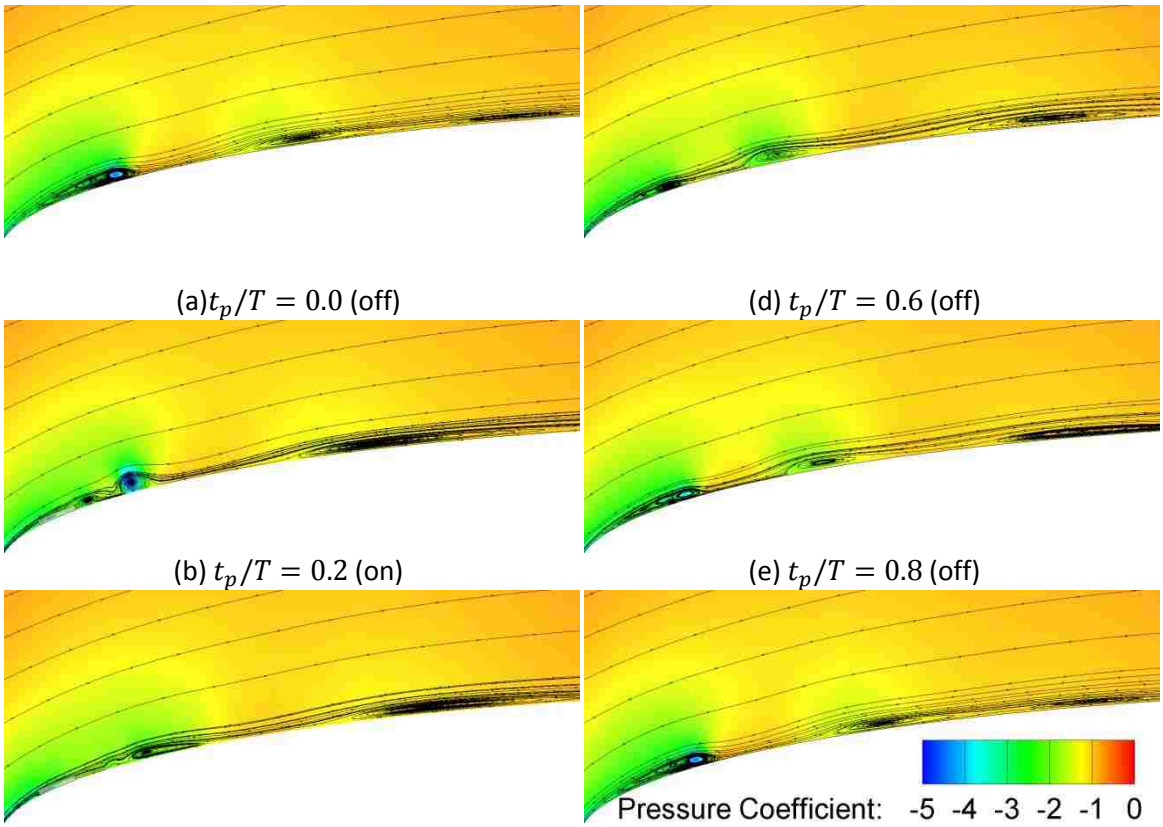

Figure 4.4. Pressure coefficient contour and streamline distributions over 1 duty cycle (*f*=2.0, *D*=0.4)

As shown in Figure 4.5, the time-dependant behavior of the pressure distribution over the airfoil is slightly different than that shown in Figure 4.3. As shown, a small secondary suction peak forms at *x/c* = 0.05 after the actuator is "turned on" at t_p/T = 0.2. However, it quickly moves downstream until merging with the third suction peak at t_p/T = 0.6. However, another suction peak simultaneously reappears at *x/c* = 0.5. From comparison with Figure 4.4, this corresponds to the first bubble growing and shifting downstream. This peak, rather than degrading and disappearing, grows until the next actuator pulse, at which point, the bubble breaks up. In terms of overall aerodynamic effect, it appears that the primary effect of the increased duty cycle with respect to the *D* = 0.2 case above is to enhance the natural suction peak of the airfoil. As shown, the

natural pressure coefficient peak varies between -3.6 and -3.8 over the course of a period, 0.2-0.4 lower than the corresponding peak of the D = 0.2 case and 0.6-0.8 lower than that of the reference case.

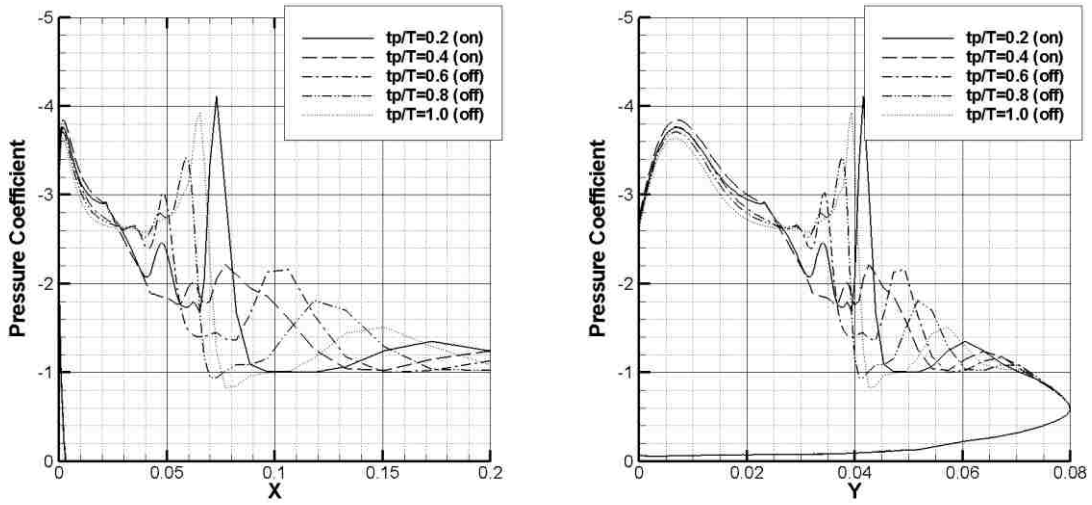

(a) C_p *vs. X* (b) C_p *vs. Y*

Figure 4.5. Influence of pulsed actuator on airfoil pressure distribution (f=2.0, D=0.4)

Figure 4.6 and Figure 4.7 show the flow-field developments and surface pressure coefficient distribution changes over the course of an actuation period with D = 0.6. The flow-field development is similar to that of the D = 0.4 case. This observation is confirmed in Figure 4.7. However, in contrast to the D = 0.4 case, the growth of the first suction peak to replace the disappeared second peak is delayed until t_p/T = 0.8. In contrast, this event took place at t_p/T = 0.6 in the D = 0.4 case. Intuitively, this observation indicates that the expansion of the first bubble is suppressed by the actuator while "on," thus limiting the eventual size of the bubble when the next actuation cycle begins. As shown in Figure 4.7, in the D = 0.6 case, the natural suction peak pressure coefficient of the airfoil is enhanced to approximately -4.0.

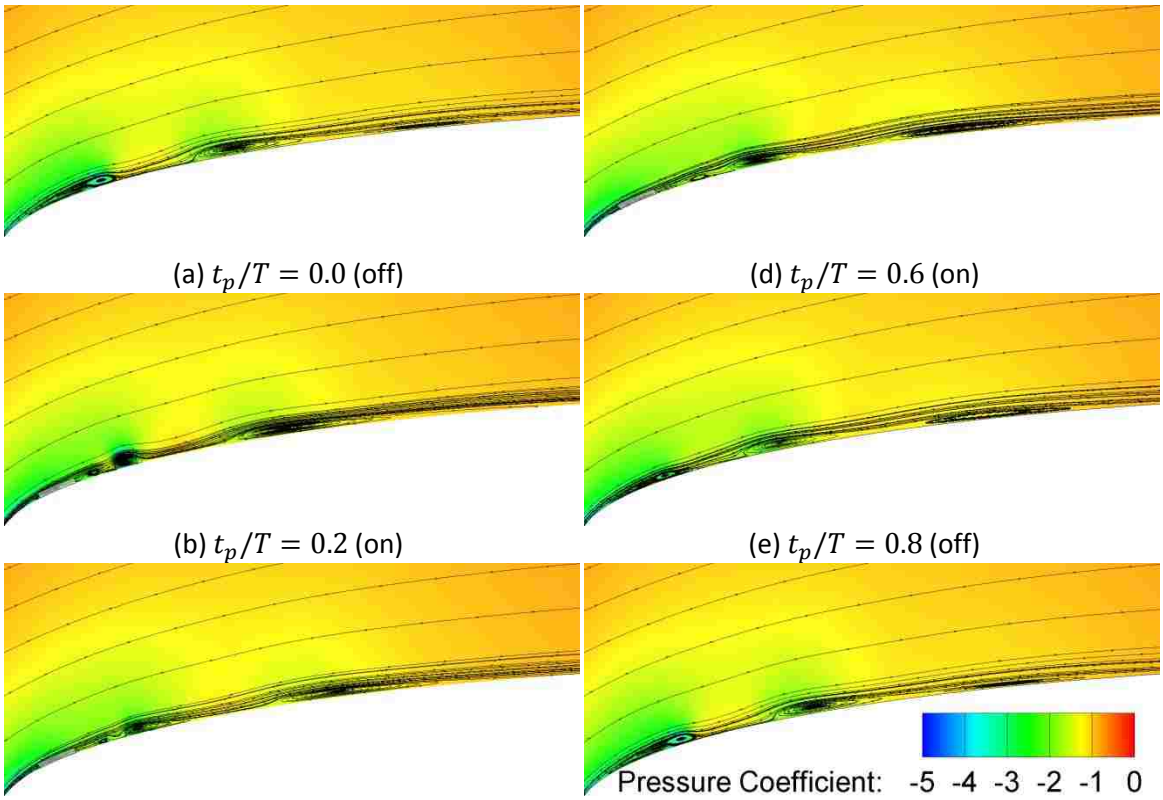

(a) $t_p/T = 0.0$ (off) (d) $t_p/T = 0.6$ (on)

(b) $t_p/T = 0.2$ (on) (e) $t_p/T = 0.8$ (off)

(c) $t_p/T = 0.4$ (on) (f) $t_p/T = 1.0$ (off)

Figure 4.6. Pressure coefficient contour and streamline distributions over 1 duty cycle (*f*=2.0, *D*=0.6)

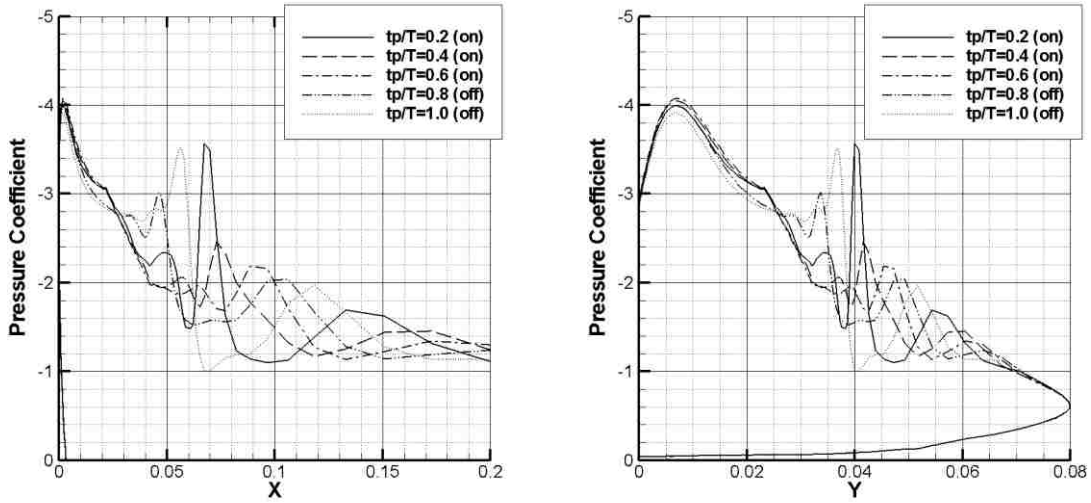

(a) C_p *vs. X* (b) C_p *vs. Y*

Figure 4.7. Influence of pulsed actuator on airfoil pressure distribution (*f*=2.0, *D*=0.6)

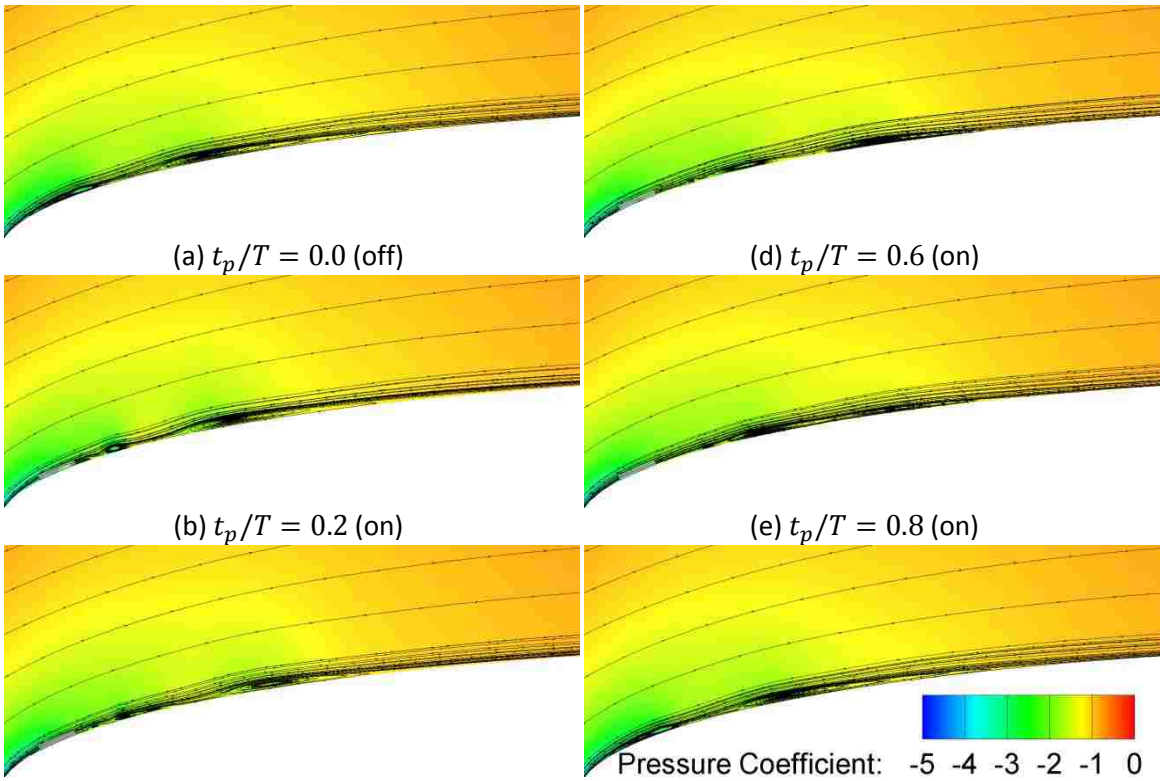

Figure 4.8. Pressure coefficient contour and streamline distributions over 1 duty cycle (f=2.0, D=0.8)

Figure 4.8 and Figure 4.9 show the flow development and airfoil pressure distribution corresponding to the case with f = 2.0 and D = 0.8. As shown in Figure 4.8, the flow-development is fundamentally similar to the D = 0.4 and D = 0.6 cases. As shown, in comparison to the other cases, the bubble features are much less pronounced than in any of the previous cases, with all features "squeezed" to the airfoil surface. Because, in this case, the actuator is "on" for most of the actuation period, there is little time available for the growth of the first bubble during the "off" portion of the period. Consequently, the surface pressure peaks corresponding to the aft bubbles are much less pronounced with respect to the previous cases, as shown in Figure 4.9. However, the natural suction peak of the airfoil in this case is enhanced to a pressure coefficient of -4.2 to -4.4, which would be expected to enhance the aerodynamic performance of the airfoil with respect to the previously discussed cases.

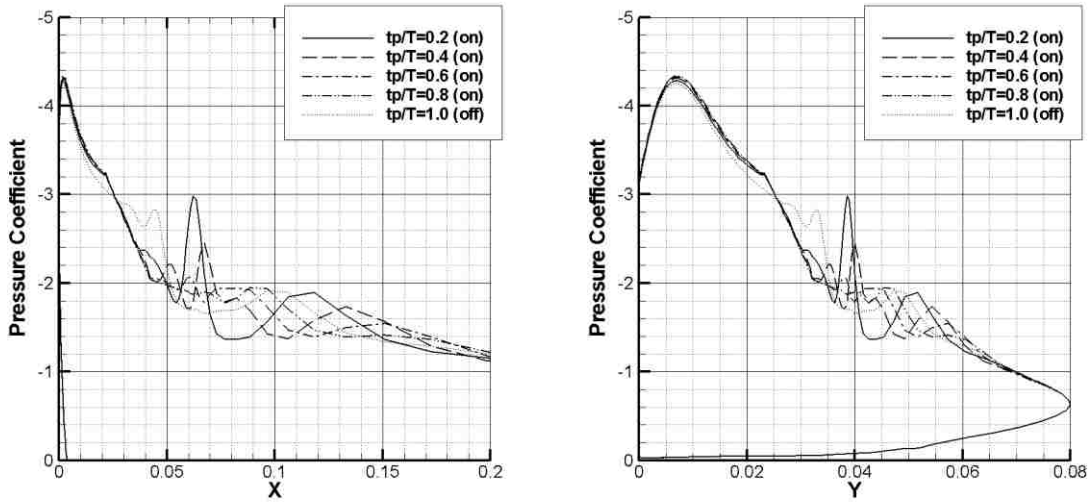

(a) C_p *vs. X* (b) C_p *vs. Y*

Figure 4.9. Influence of pulsed actuator on airfoil pressure distribution (f=2.0, D=0.8)

Figure 4.10, Figure 4.11, and Figure 4.12 plot the temporal responses of the airfoil lift coefficient, drag coefficient, and lift-to-drag ratio for f = 2.0 and D from 0 (reference case) to 1 (steady actuation) in increments of 0.2, corresponding to all of the cases discussed above. As shown in Figure 4.10, as the duty cycle is increased, the quasi-equilibrium lift coefficient increases. This is to be expected, given the greater amount of time spent in the active state, and hence power requirements. However, the degree of improvement over the baseline case clearly does not increase linearly with the duty cycle. For instance, the improvement in the average lift coefficient of the D=0.2 case and the reference case is marginal (approximately 0.01). However, the D=0.4 case exhibits a C_l improvement of approximately 0.06, despite only double the duty cycle of the previous case, making the actuator of D=0.4 roughly 3 times as effective as an actuator of D=0.2 in terms of lift enhancement.

Further examination of Figure 4.10 reveals that the time required to reach quasi-equilibrium after initialization is dependent upon the duty cycle. From visual observation, the time required for initial large-scale flow-field instabilities to damp out decreases as the duty cycle increases. For instance, it takes more than twice as long for the instabilities in the D=0.2 case to become negligible than for the D=1.0 case. The

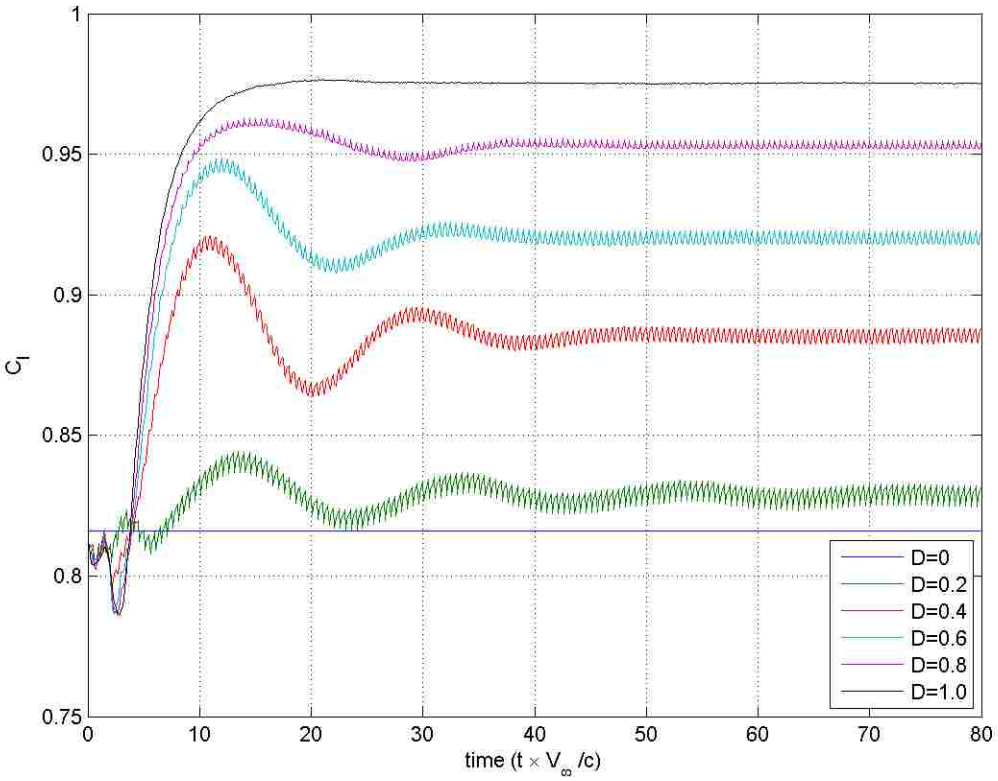

Figure 4.10. Transient response of lift coefficient to pulsed actuator (f = 2.0)

amplitude of the quasi-equilibrium oscillations resulting from pulsing is also shown to be dependent upon duty cycle. As shown, the amplitude of the equilibrium waveform of the D=0.2 case is clearly greater than that of any of the higher D cases. Presumably, this results from the previously mentioned dependence of the aft-bubble peak amplitude on the length of the "off" portion of the actuation period.

As shown in Figure 4.11, the time-averaged drag coefficient in the D=0.2 case is approximately 0.046, significantly lower than that of the reference case (0.056). Subsequent increases in the duty cycle result in further reductions in the drag coefficient. As with the lift coefficient, this trend is to be expected, given the larger fraction of time spent in the active state as D is increased.

The amplitude of the C_d waveform with respect to the average values is relatively high. In the most severe example (D=0.4), the peak-to-peak amplitude of the waveform is approximately 4 percent of the average value. By comparison, the most severe variations in the lift coefficient at f=2.0 (D=0.2) is about 1 percent of the mean C_l at that

case. However, the absolute magnitudes of the drag amplitudes are significantly smaller than those of the lift. As shown, the cases with mild duty cycles (D=0.4 and D=0.6) exhibit larger amplitudes than the cases with either "high" or "low" duty cycles.

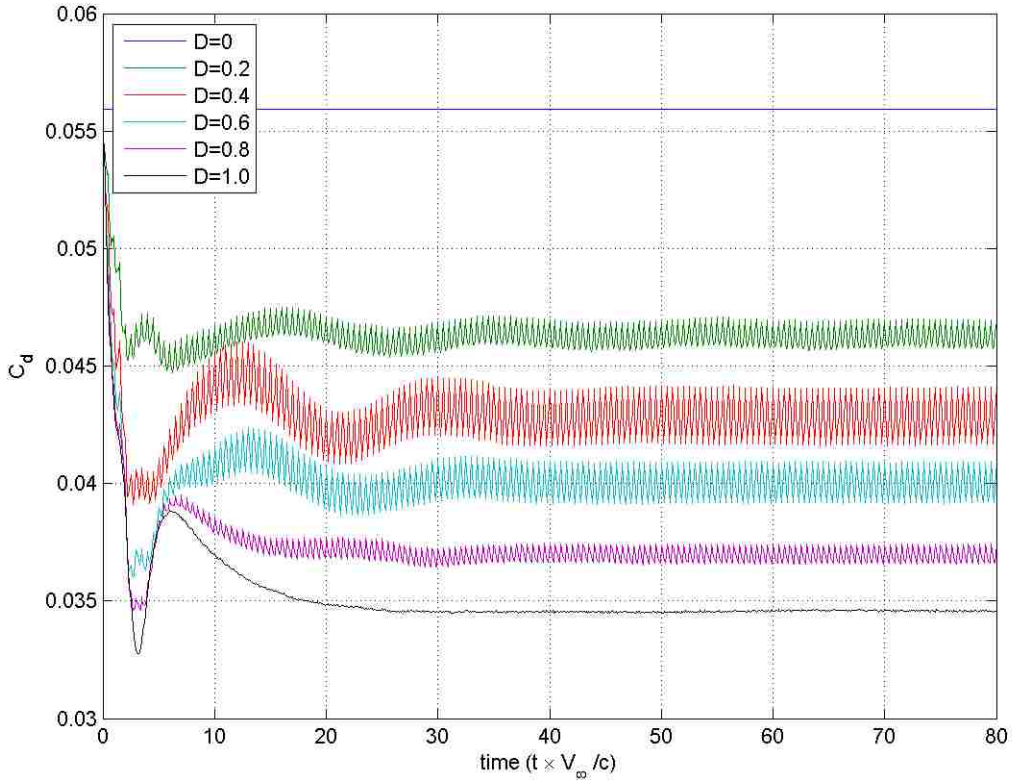

Figure 4.11. Transient response of drag coefficient to pulsed actuator (f = 2.0)

Figure 4.12 shows the temporal response of the lift to drag ratio of the airfoil at a frequency f of 2.0 and various duty cycles. In agreement with the previous results, the quasi-steady average lift-to-drag ratio increases with D. Also in agreement with the previous results, the time required for the airfoil to reach quasi-steady operation decreases as D is increased. In agreement with Figure 4.11, the largest steady-state waveform amplitudes are observed at mild duty cycles (D=0.4 and D=0.6).

4.1.2. *f*=1.0 case. Figure 4.13 shows the flow-field developments over one quasi-steady actuation period. Note that the time increment between frames is double that of the figures in the previous section. As shown, the bubble features are far more

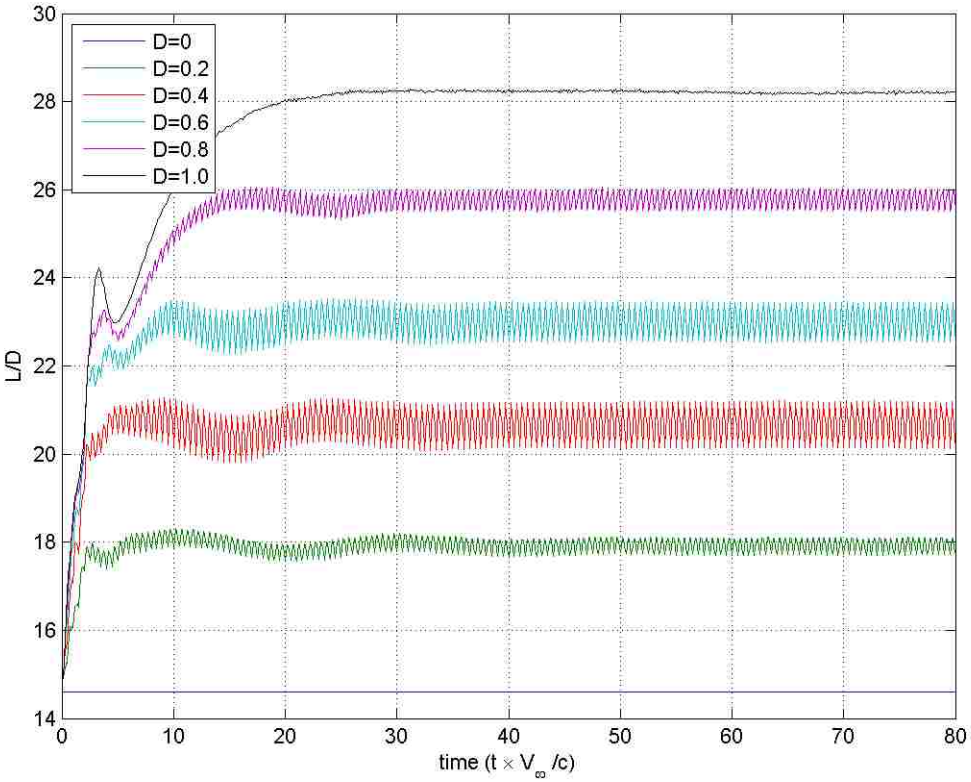

Figure 4.12. Transient response of lift to drag ratio to pulsed actuator (f = 2.0)

pronounced in this case than any of the previously presented cases. This is a result of the longer sustained inactive state associated with the lower actuation frequency (longer period). Put another way, within each period, the fluid has a longer time to respond after the actuator pulse. It logically follows that the fluid would tend, in this state, to approach the reference solution. As explained in the previous section, the greater time allowed for the flow-field development would also tend to result in greatly enhanced pressure peaks associated with the bubble flow structures. This trend is also observed when comparing Figure 4.14 with the comparable figures from the previous section. In terms of net aerodynamic effects, this would also be expected to result in larger peak-to peak amplitudes in the lift coefficient, drag coefficient, and lift-to-drag ratio.

The flow and pressure distribution trends for this case, and all cases with f = 1.0 are the same as those observed for the D = 0.4, 0.6, and 0.8 cases for f = 2.0, so they will not be discussed in great detail here. For reference, Figure 4.15 through Figure 4.20 are provided, which contain the same data for the D = 0.4, 0.6, and 0.8 cases.

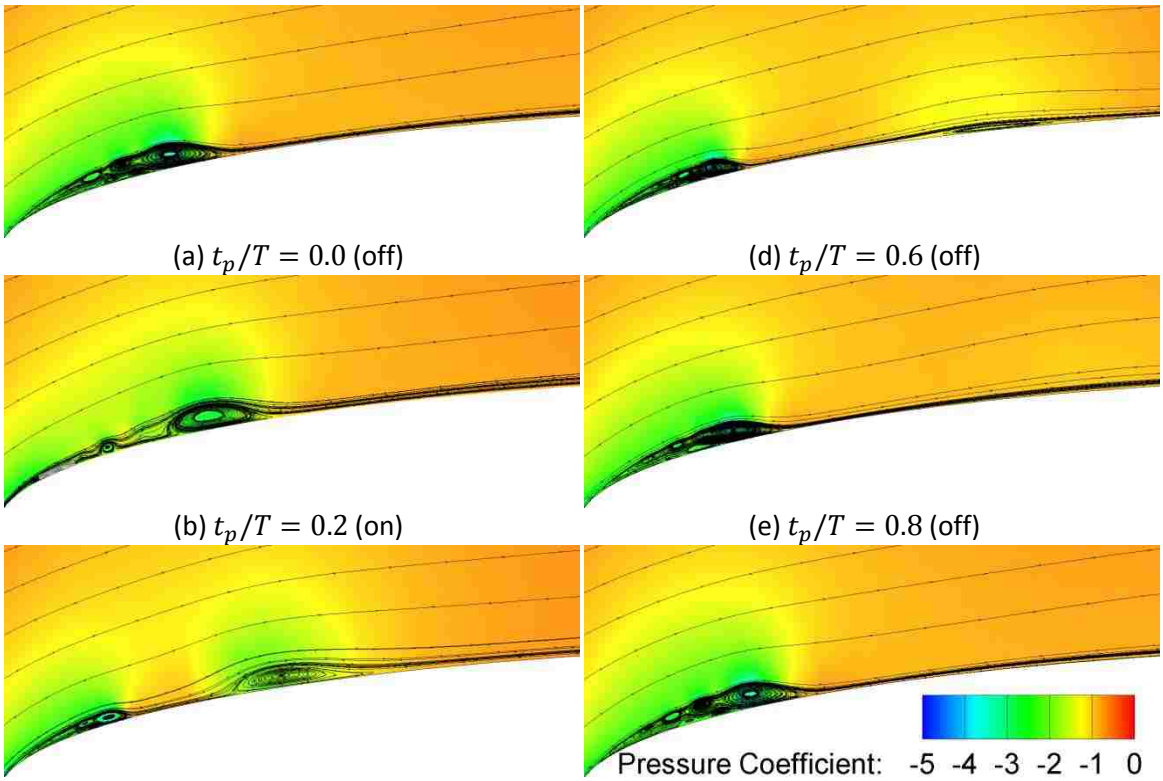

(a) $t_p/T = 0.0$ (off) (d) $t_p/T = 0.6$ (off)

(b) $t_p/T = 0.2$ (on) (e) $t_p/T = 0.8$ (off)

(c) $t_p/T = 0.4$ (off) (f) $t_p/T = 1.0$ (off)

Figure 4.13. Pressure coefficient contour and streamline distributions over 1 duty cycle (f=1.0, D=0.2)

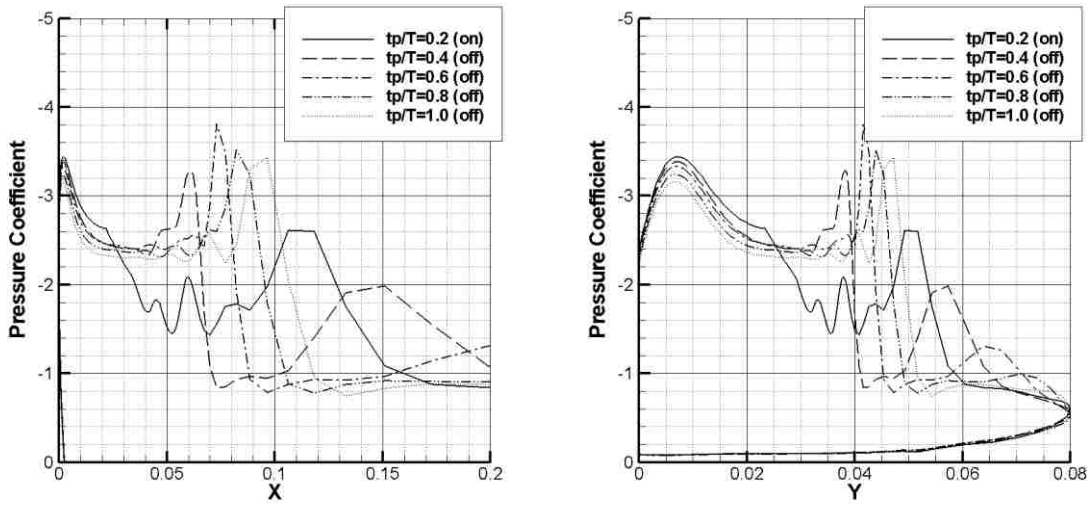

(a) C_p *vs. X* (b) C_p *vs. Y*

Figure 4.14. Influence of pulsed actuator on airfoil pressure distribution (f=1.0, D=0.2)

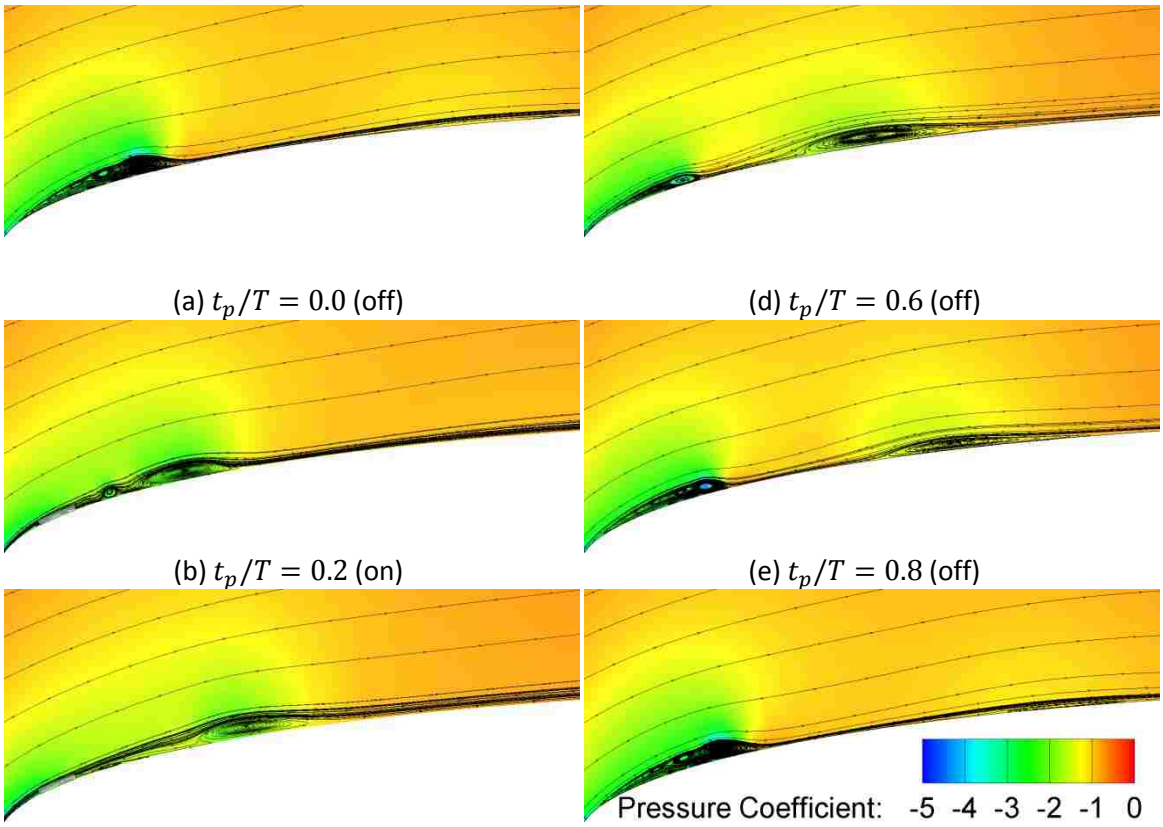

(a) $t_p/T = 0.0$ (off) (d) $t_p/T = 0.6$ (off)

(b) $t_p/T = 0.2$ (on) (e) $t_p/T = 0.8$ (off)

(c) $t_p/T = 0.4$ (on) (f) $t_p/T = 1.0$ (off)

Figure 4.15. Pressure coefficient contour and streamline distributions over 1 duty cycle (f=1.0, D=0.4)

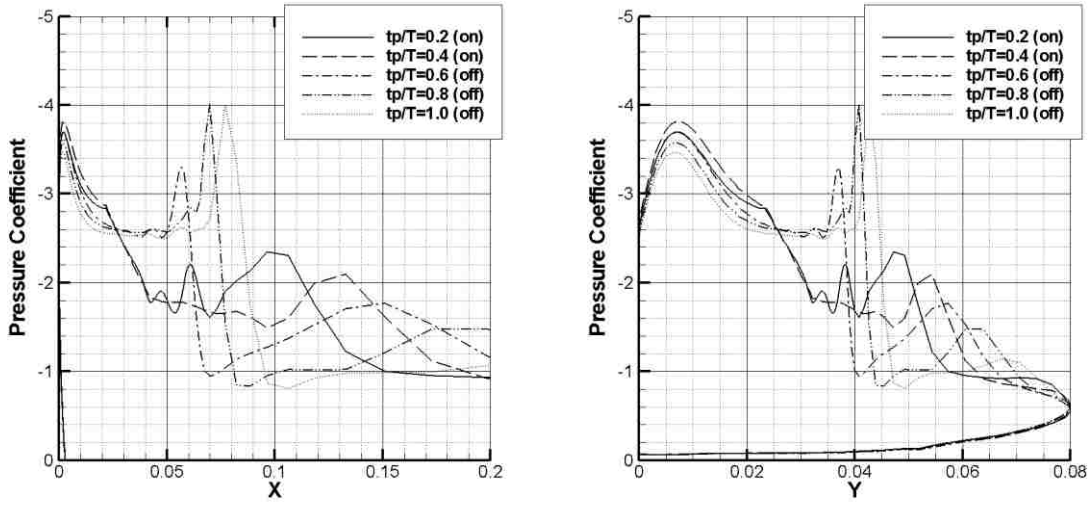

(a) C_p *vs. X* (b) C_p *vs. Y*

Figure 4.16. Influence of pulsed actuator on airfoil pressure distribution (f=1.0, D=0.4)

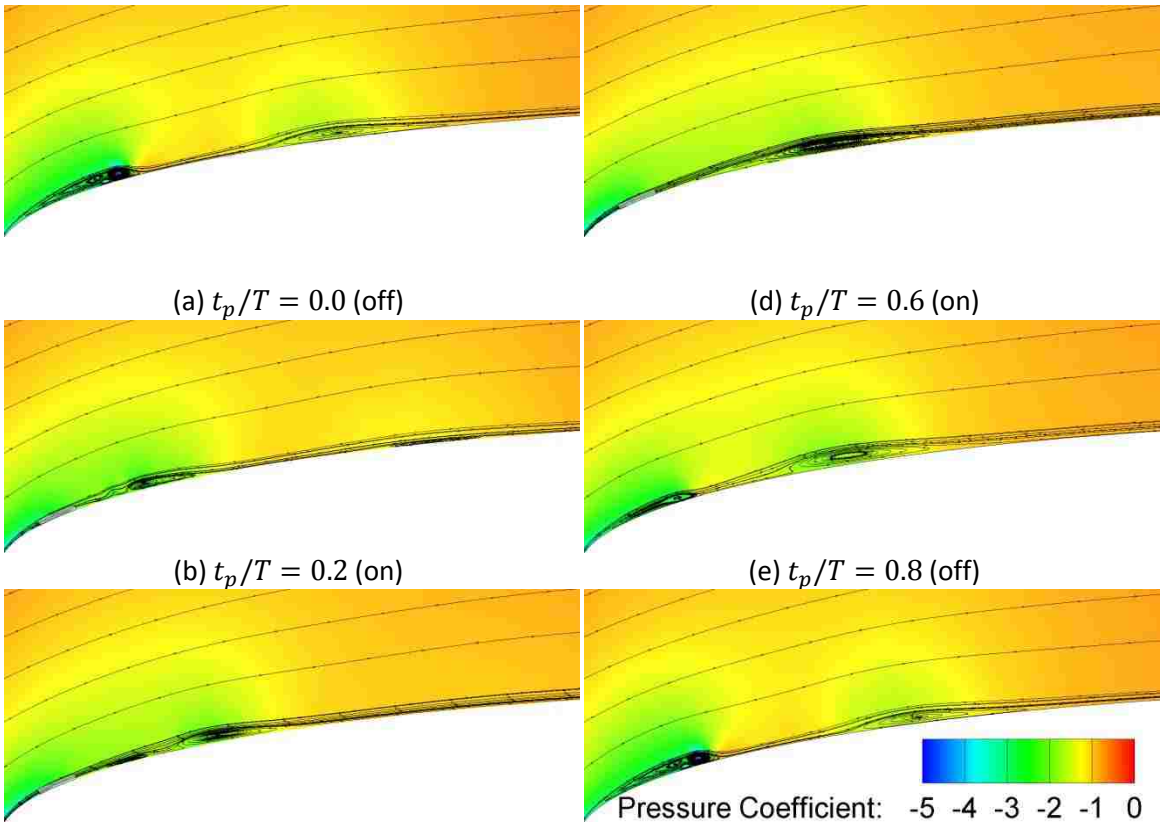

(a) $t_p/T = 0.0$ (off) (d) $t_p/T = 0.6$ (on)

(b) $t_p/T = 0.2$ (on) (e) $t_p/T = 0.8$ (off)

(c) $t_p/T = 0.4$ (on) (f) $t_p/T = 1.0$ (off)

Figure 4.17. Pressure coefficient contour and streamline distributions over 1 duty cycle (f=1.0, D=0.6)

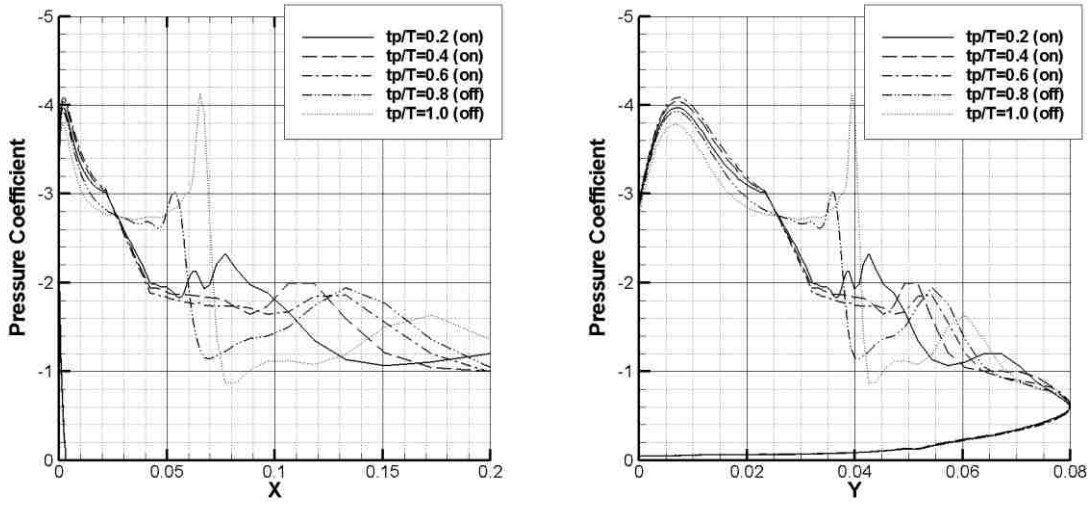

(a) C_p *vs. X* (b) C_p *vs. Y*

Figure 4.18. Influence of pulsed actuator on airfoil pressure distribution (f=1.0, D=0.6)

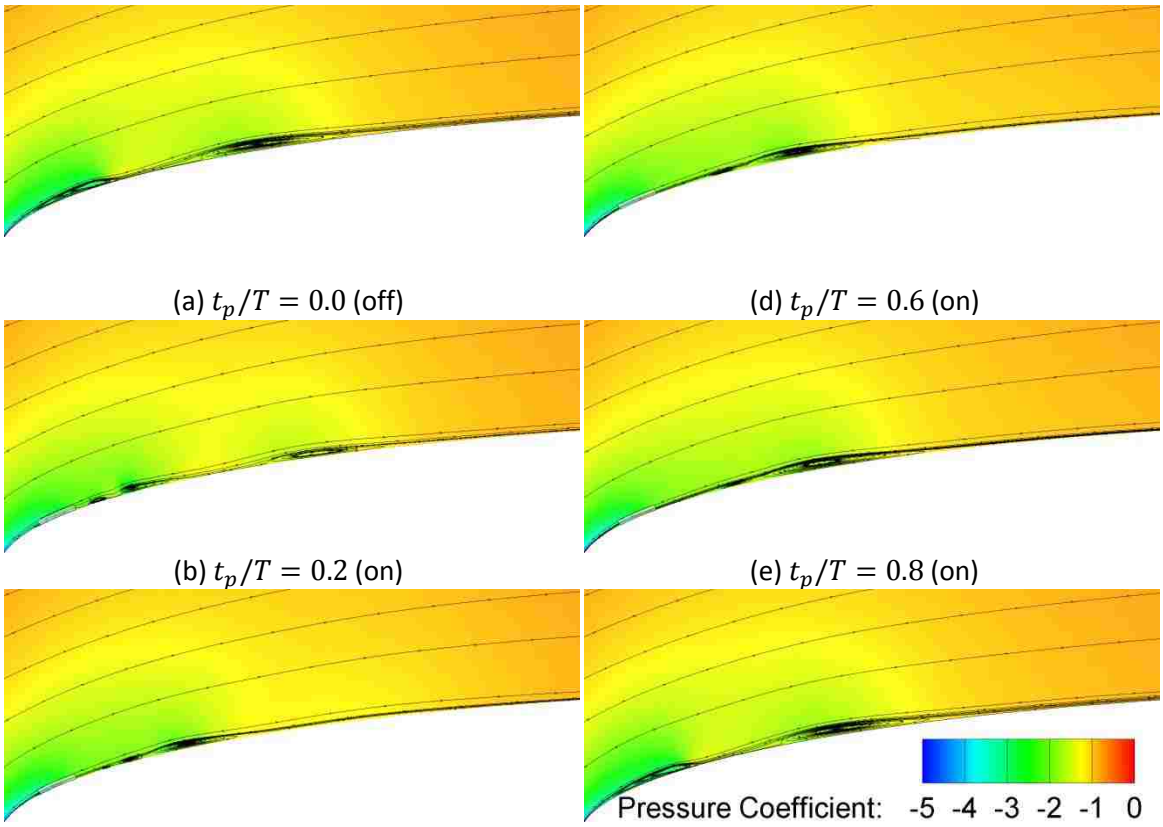

(a) $t_p/T = 0.0$ (off) (d) $t_p/T = 0.6$ (on)

(b) $t_p/T = 0.2$ (on) (e) $t_p/T = 0.8$ (on)

(c) $t_p/T = 0.4$ (on) (f) $t_p/T = 1.0$ (off)

Figure 4.19. Pressure coefficient contour and streamline distributions over 1 duty cycle (*f*=1.0, *D*=0.8)

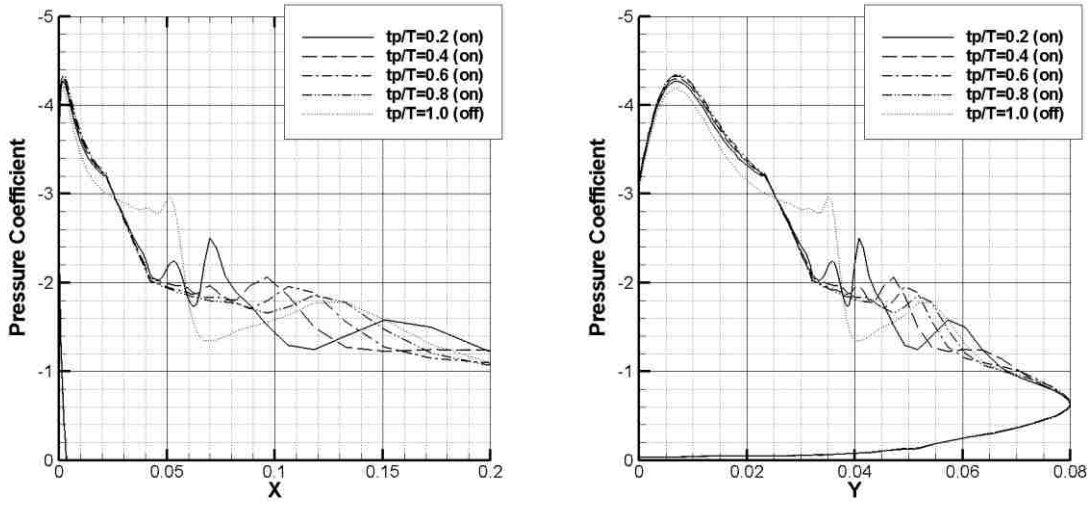

(a) C_p *vs. X* (b) C_p *vs. Y*

Figure 4.20. Influence of pulsed actuator on airfoil pressure distribution (*f*=1.0, *D*=0.8)

Figure 4.21 shows the transient response of the lift coefficient to an actuator operated at a non-dimensional frequency of 1.0. As shown, many of the trends observed in Figure 4.10 are also present in Figure 4.21. There exists a non-linear dependence of actuator effectiveness on duty cycle as well as shorter damping times and smaller amplitude oscillations associated with increased duty cycle. As was observed in Figure 4.10, there exists a dependence of C_l amplitude upon frequency. As shown, the oscillation amplitudes in Figure 4.21 are clearly greater than those present in Figure 4.10. This is in agreement with the previous comments regarding the effects of frequency on waveform amplitude.

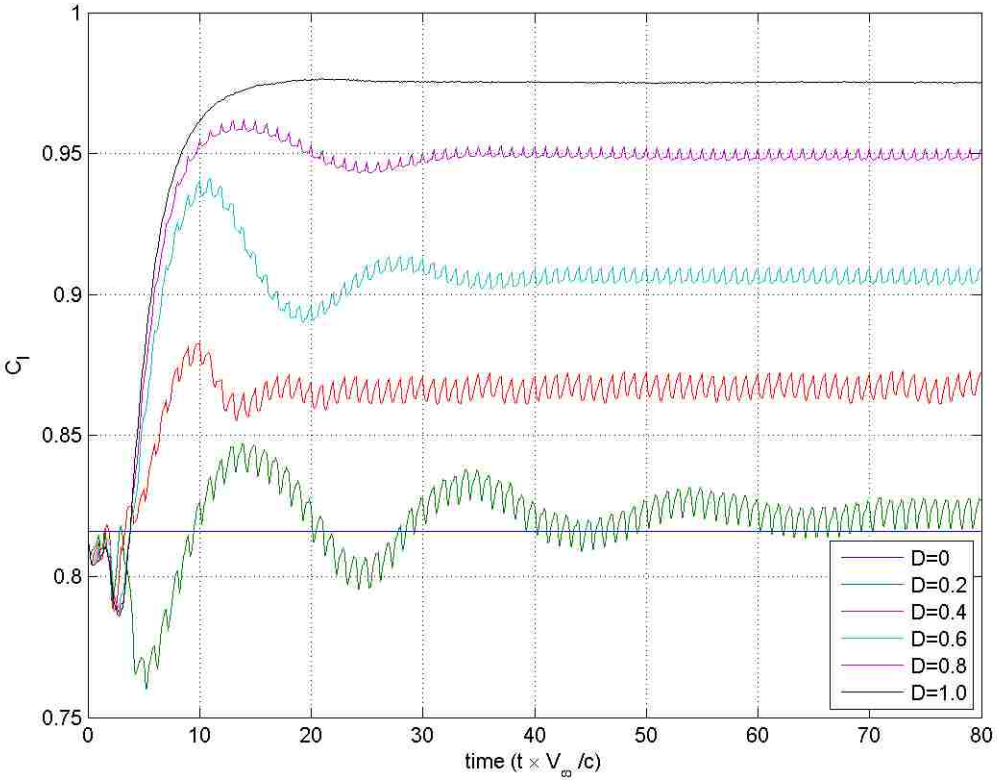

Figure 4.21. Transient response of lift coefficient to pulsed actuator (f = 1.0)

Figure 4.22 shows the C_d response of the airfoil under an actuation frequency f of 1.0. As shown, the general trends discussed above regarding the mean C_d and amplitude dependence upon duty cycle are still present. There is no appreciable change in the mean

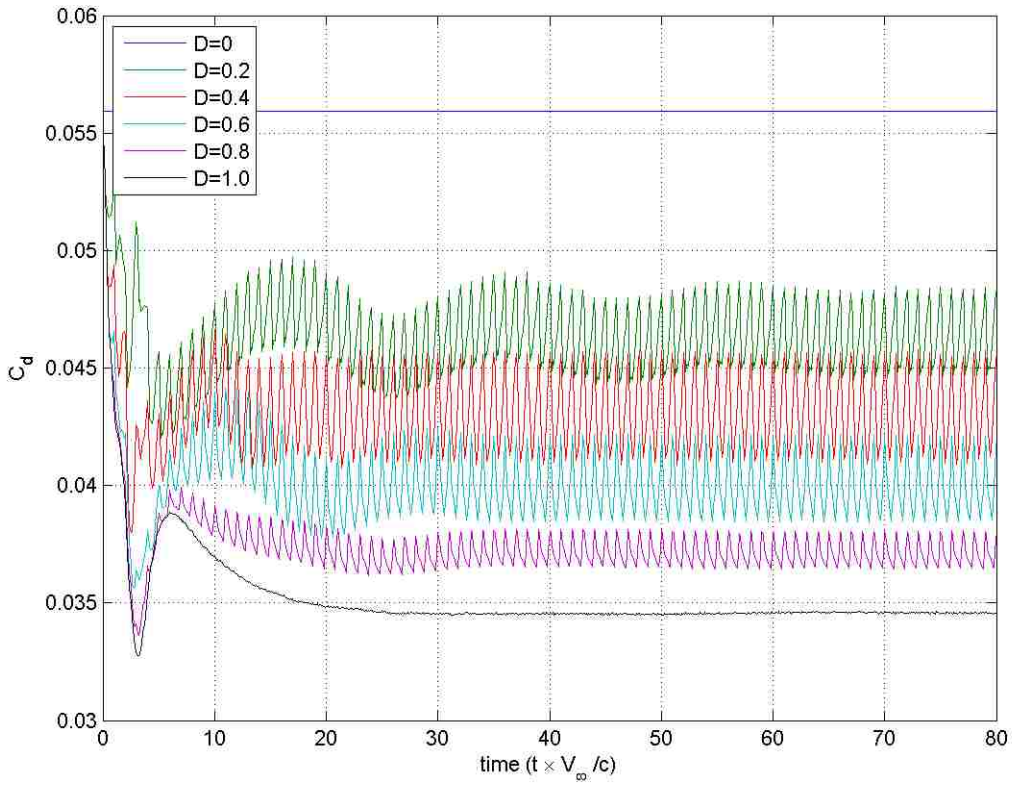

Figure 4.22. Transient response of drag coefficient to pulsed actuator (f = 1.0)

drag coefficient with respect to the f=2.0 case. However, the amplitudes under each duty cycle are noticeably greater than those at f=2.0. This again was expected as a result of the longer fluid response times over the course of each period. As the frequency is further decreased, as will be shown in Figure 4.32, Figure 4.33, and Figure 4.34, the amplitudes increase dramatically, to the point where the peaks in the D=0.4 and D=0.6 waveforms exceed the reference C_d and the trough values fall below the equilibrium steady-state C_d over the course of a single period in the f=0.125 case. In these cases, the drag coefficient is observed to fluctuate by over 50% of the respective average values.

Figure 4.23, Figure 4.34, Figure 4.45, and Figure 4.56show the transient response of the lift-to-drag ratio for frequencies f=1.0 through f=0.125. The trends regarding peak-to-peak amplitude in drag as frequency is decreased are also present in the lift-to-drag ratio. As shown, as the actuator frequency is decreased, the waveform amplitudes are noticeable increased. In the most severe cases, the lift-to-drag ratio is found to fluctuate by greater than 50 percent of the respective mean, which may be undesirable in most practical applications for obvious reasons.

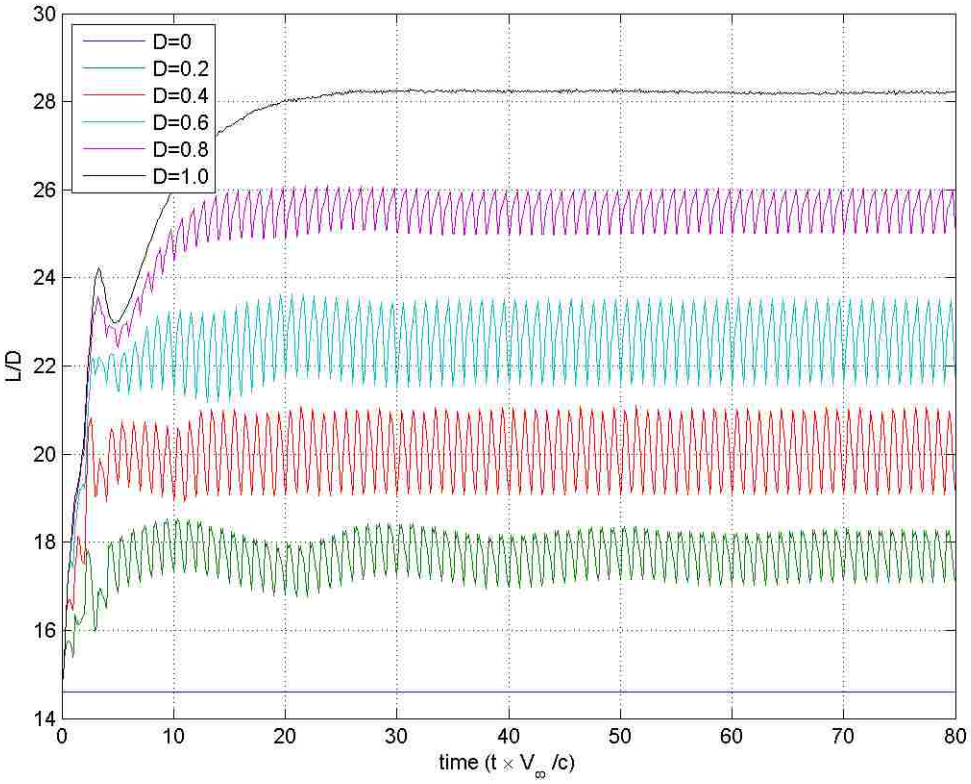

Figure 4.23. Transient response of lift to drag ratio to pulsed actuator (f = 1.0)

4.1.3. f = 0.5 case. Figure 4.24 through Figure 4.31 give the periodic flow-field and pressure distribution developments for f = 0.5 and duty cycles between 0.2 and 0.8. The flow physics are fundamentally the same as those previously discussed, and will not be discussed here. However, the figures are provided as a reference.

Figure 4.32, Figure 4.33, and Figure 4.34 show the temporal response of the lift coefficient, drag coefficient, and lift-to-drag ratio at f=0.5. Of note in Figure 4.33 is that the effectiveness of the actuator in enhancing lift at low duty cycles is clearly superior to that predicted at higher frequencies (f = 1.0 and 2.0). For instance, for a 20% duty cycle, the actuator was more than twice as effective in C_l enhancement at f=0.5 (improvement of ~0.03) than at f=2.0 (improvement of ~0.01). However, as will be shown, this trend does not extrapolate to lower frequencies.

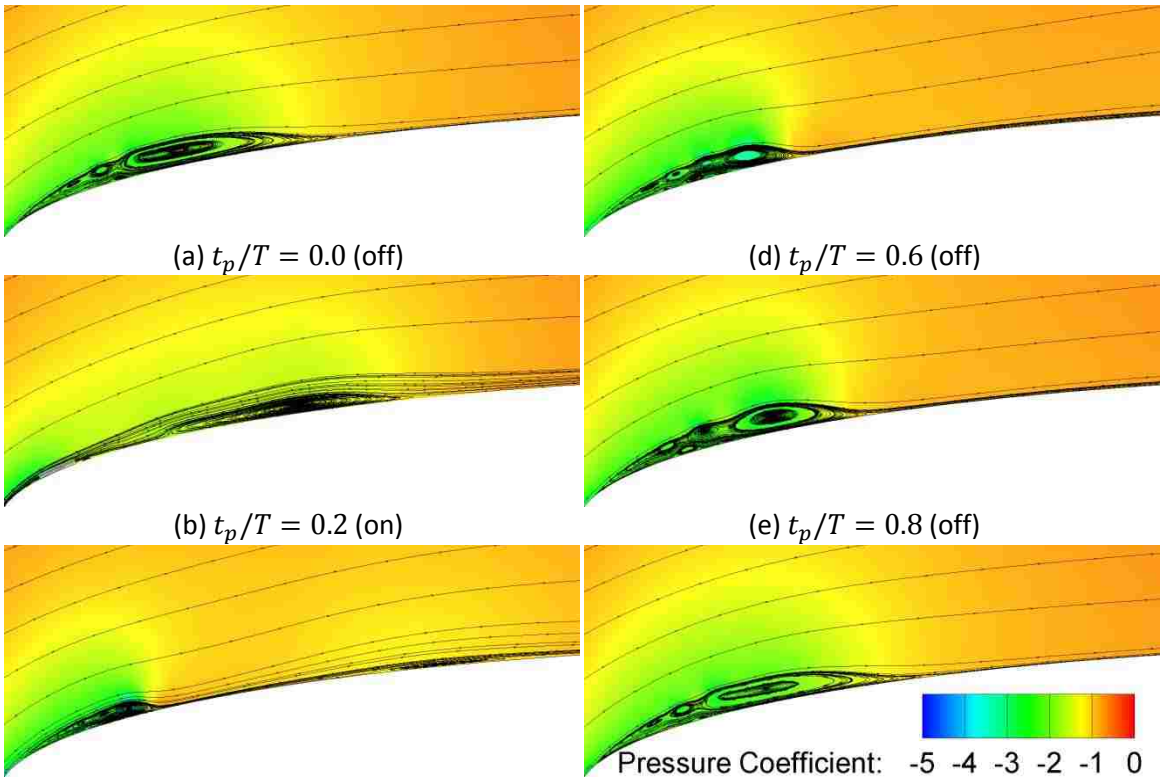

(a) $t_p/T = 0.0$ (off) (d) $t_p/T = 0.6$ (off)

(b) $t_p/T = 0.2$ (on) (e) $t_p/T = 0.8$ (off)

(c) $t_p/T = 0.4$ (off) (f) $t_p/T = 1.0$ (off)

Figure 4.24. Pressure coefficient contour and streamline distributions over 1 duty cycle (f=0.5, D=0.2)

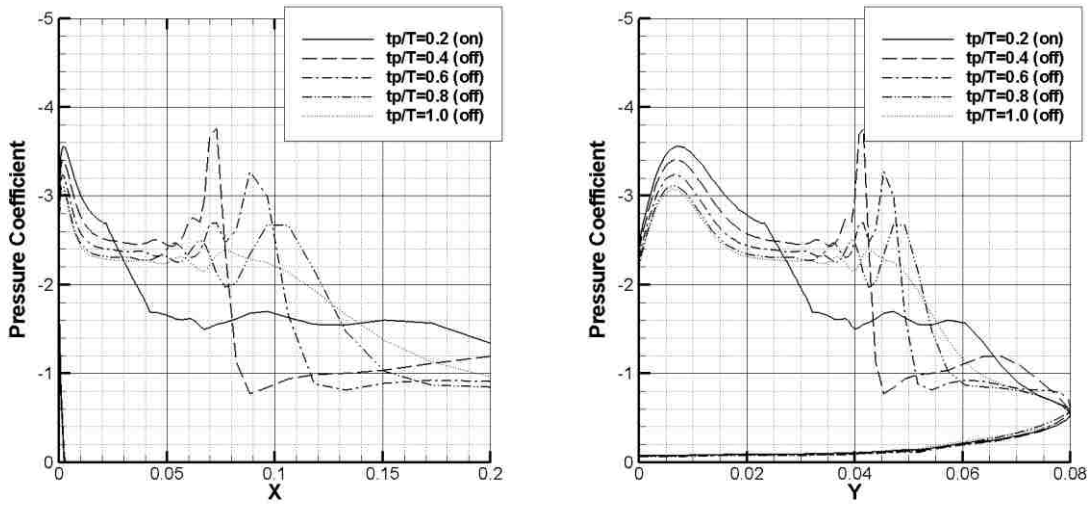

(a) C_p *vs. X* (b) C_p *vs. Y*

Figure 4.25. Influence of pulsed actuator on airfoil pressure distribution (f=0.5, D=0.2)

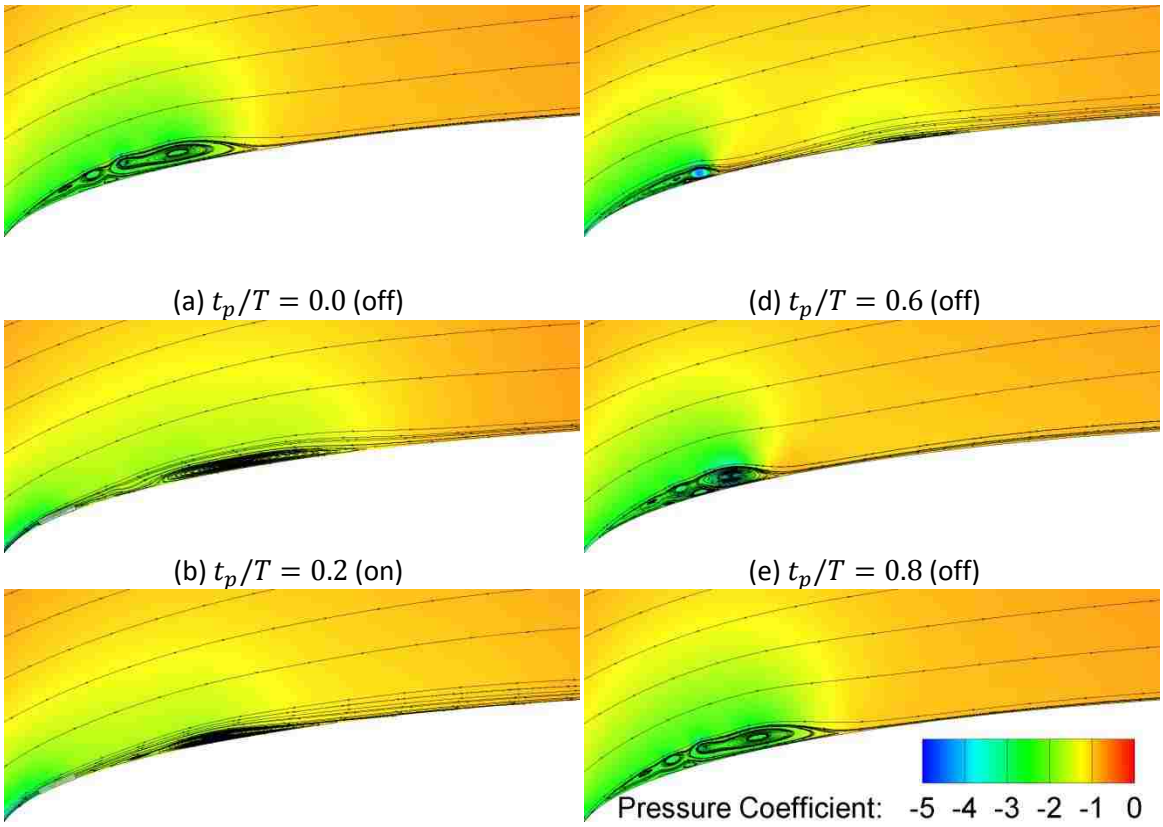

(a) $t_p/T = 0.0$ (off) (d) $t_p/T = 0.6$ (off)

(b) $t_p/T = 0.2$ (on) (e) $t_p/T = 0.8$ (off)

(c) $t_p/T = 0.4$ (on) (f) $t_p/T = 1.0$ (off)

Figure 4.26. Pressure coefficient contour and streamline distributions over 1 duty cycle (f=0.5, D=0.4)

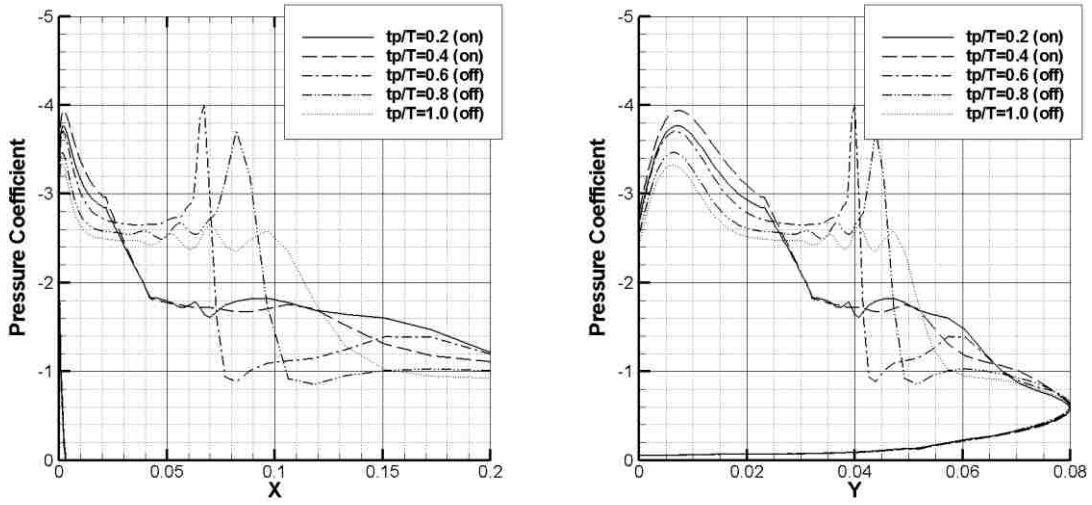

(a) C_p *vs. X* (b) C_p *vs. Y*

Figure 4.27. Influence of pulsed actuator on airfoil pressure distribution (f=0.5, D=0.4)

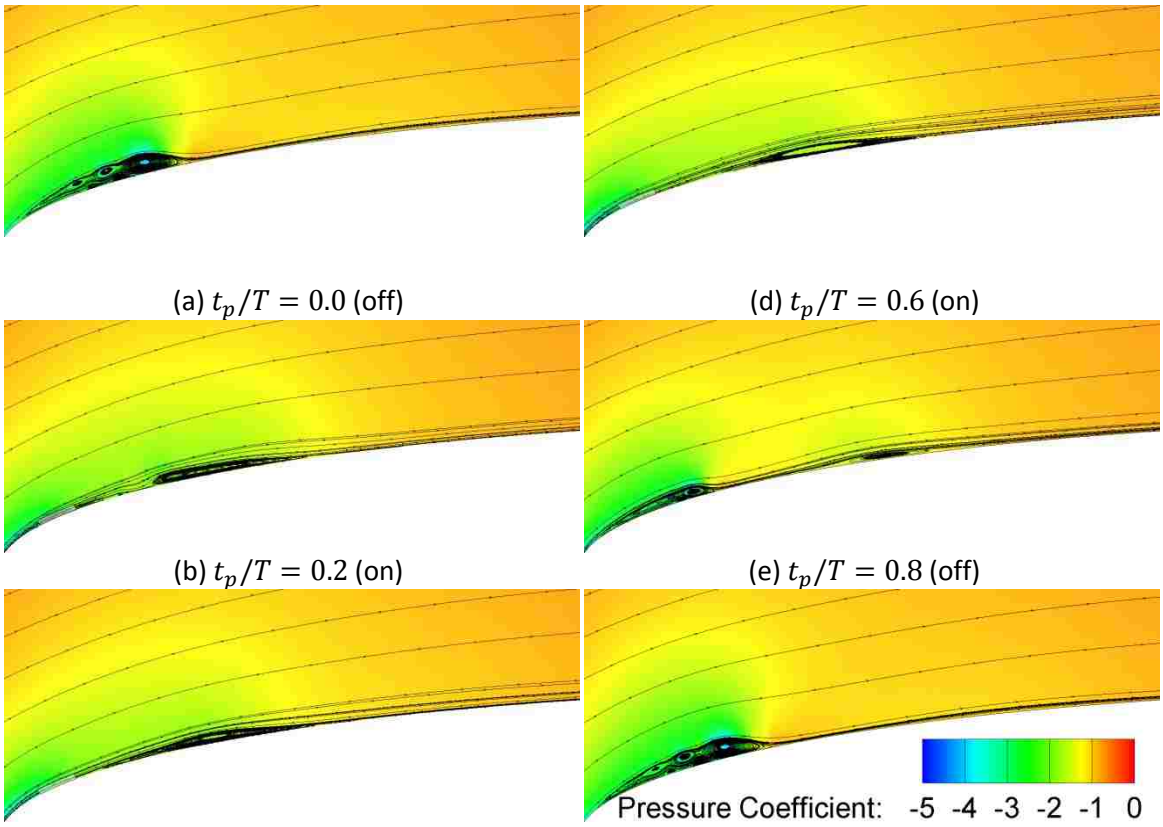

(a) $t_p/T = 0.0$ (off) (d) $t_p/T = 0.6$ (on)

(b) $t_p/T = 0.2$ (on) (e) $t_p/T = 0.8$ (off)

(c) $t_p/T = 0.4$ (on) (f) $t_p/T = 1.0$ (off)

Figure 4.28. Pressure coefficient contour and streamline distributions over 1 duty cycle (f=0.5, D=0.6)

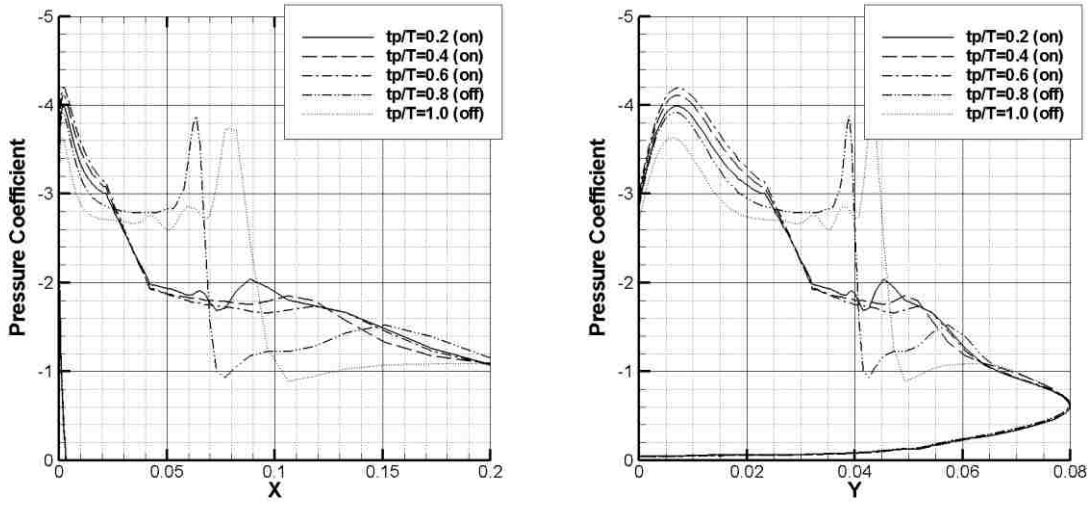

(a) C_p *vs. X* (b) C_p *vs. Y*

Figure 4.29. Influence of pulsed actuator on airfoil pressure distribution (f=0.5, D=0.6)

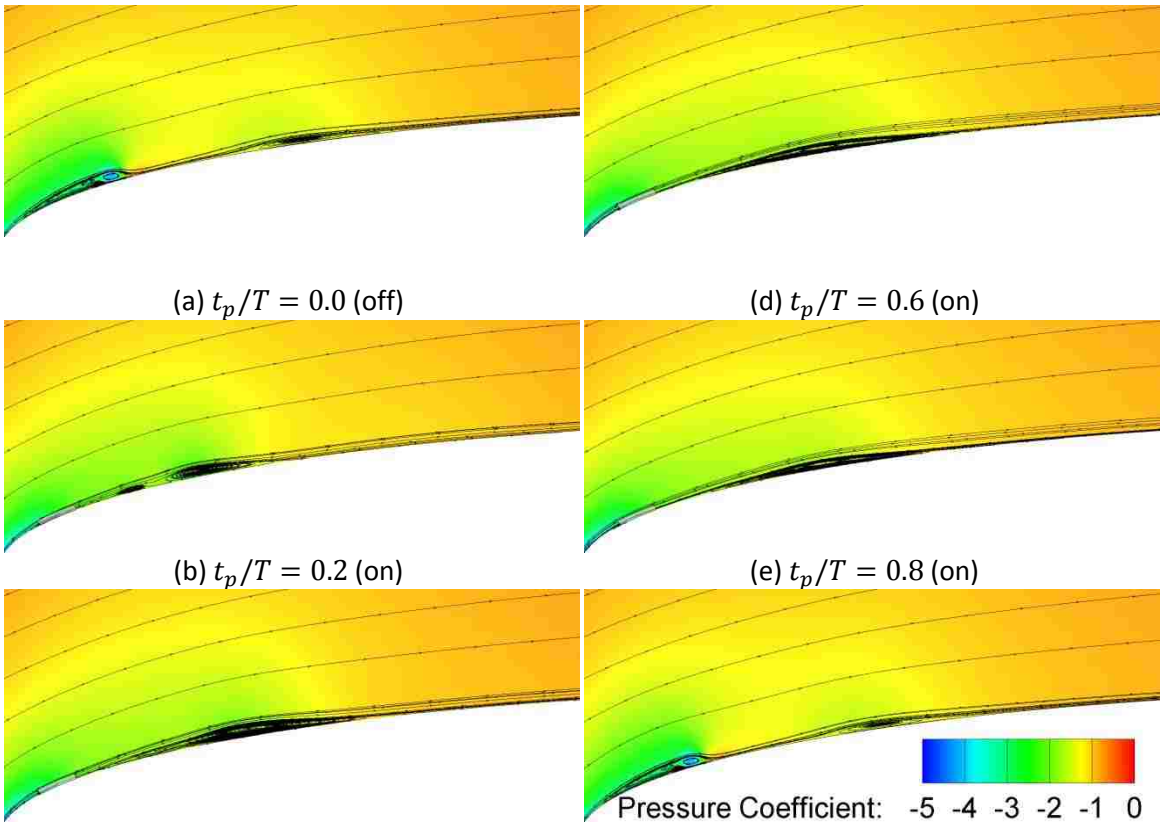

(a) $t_p/T = 0.0$ (off) (d) $t_p/T = 0.6$ (on)

(b) $t_p/T = 0.2$ (on) (e) $t_p/T = 0.8$ (on)

(c) $t_p/T = 0.4$ (on) (f) $t_p/T = 1.0$ (off)

Figure 4.30. Pressure coefficient contour and streamline distributions over 1 duty cycle (f=0.5, D=0.8)

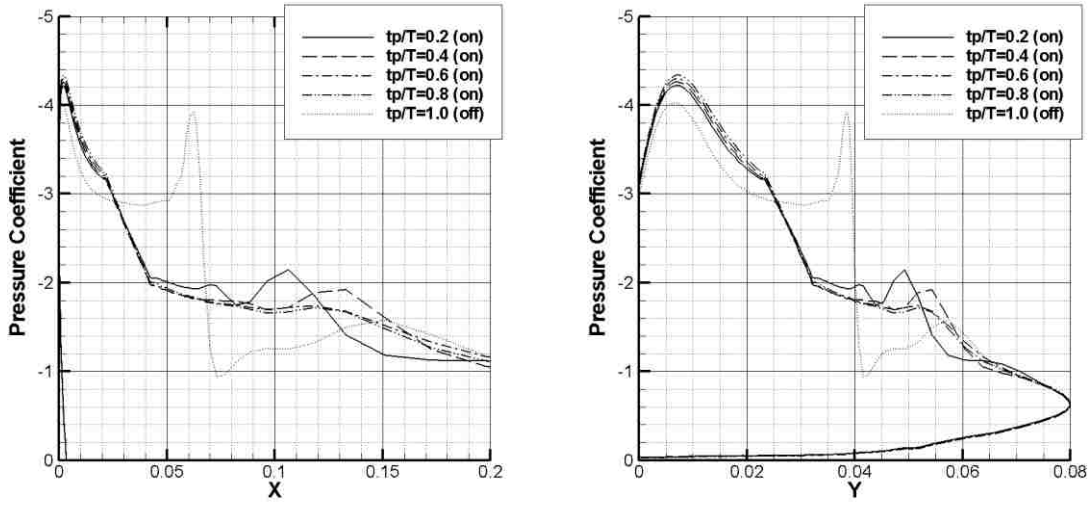

(a) C_p *vs. X* (b) C_p *vs. Y*

Figure 4.31. Influence of pulsed actuator on airfoil pressure distribution (f=0.5, D=0.8)

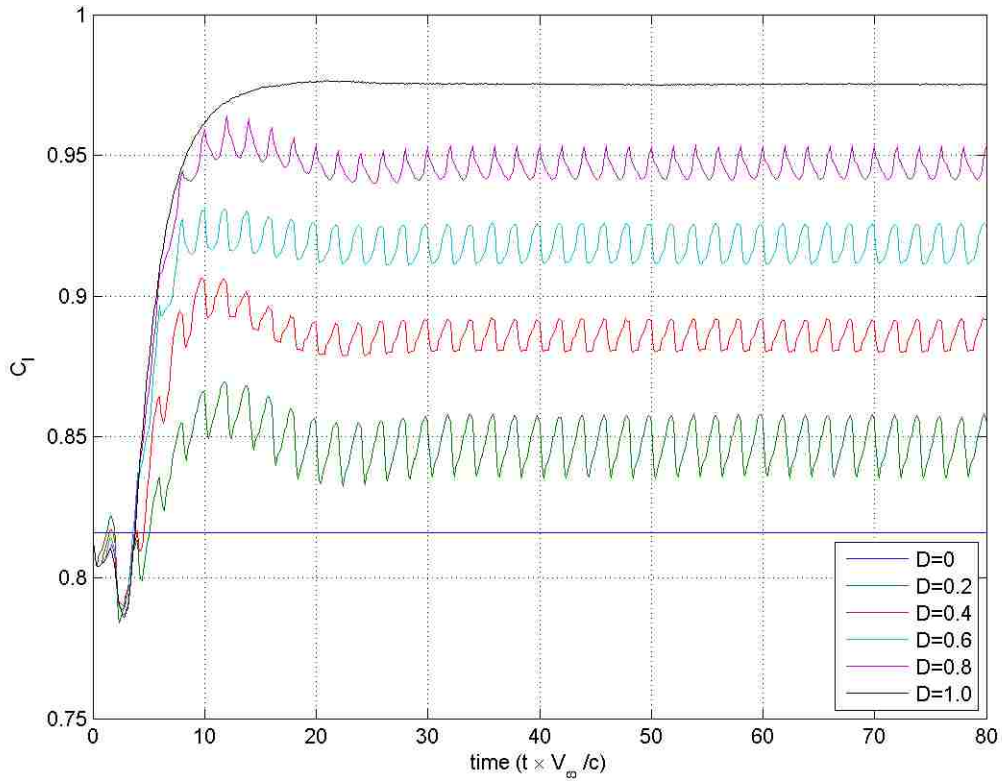

Figure 4.32. Transient response of lift coefficient to pulsed actuator (f = 0.5)

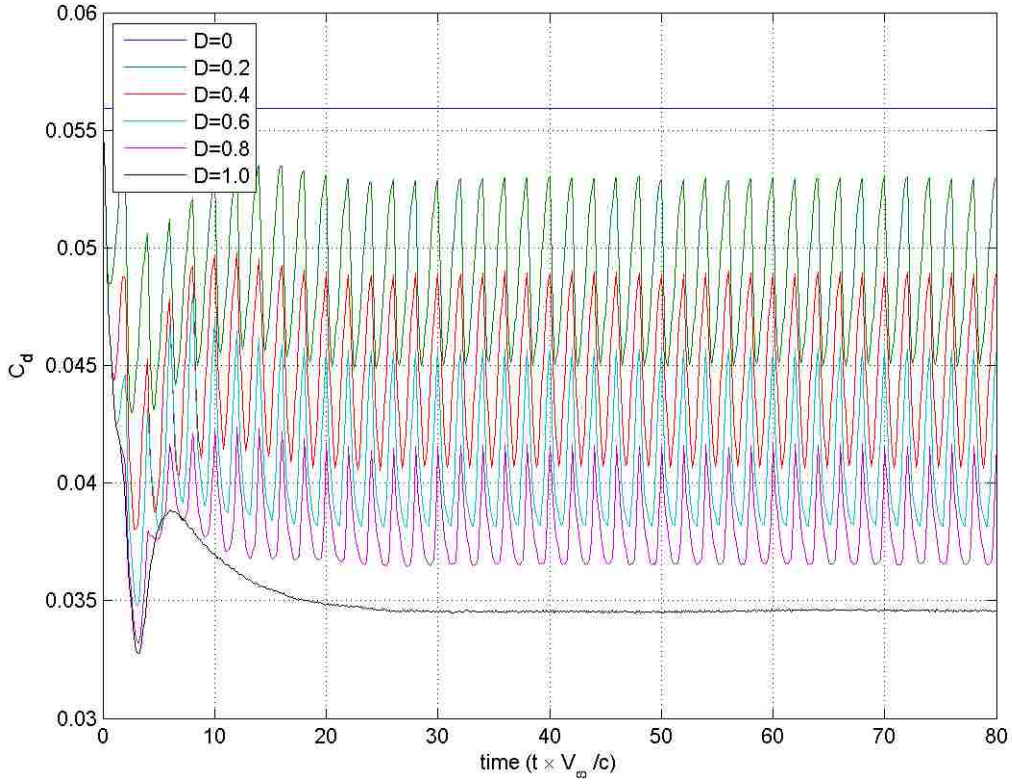

Figure 4.33. Transient response of drag coefficient to pulsed actuator (f = 0.5)

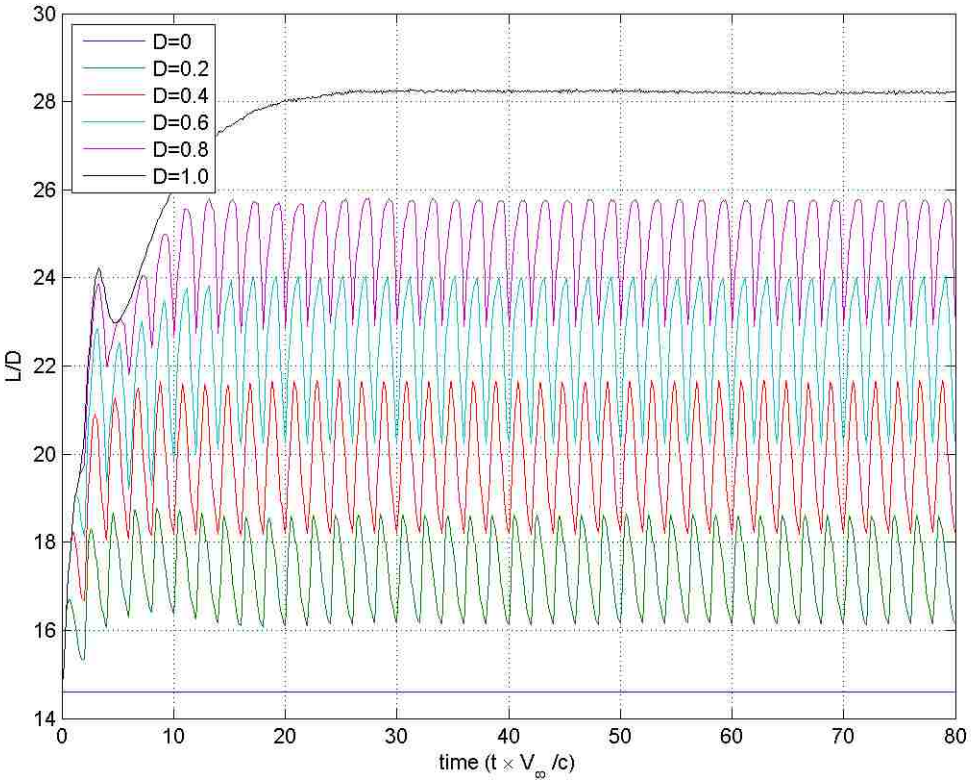

Figure 4.34. Transient response of lift to drag ratio to pulsed actuator (f = 0.5)

4.1.4. f = 0.25 case. Figure 4.35 through Figure 4.42 give the flow-field and pressure coefficient distribution developments for a frequency f = 0.25 and duty cycles D between 0.2 and 0.8. As with the figures previously discussed, the flow developments are similar to those presented previously, and will not be discussed at length.

Figure 4.43 shows the transient response of the lift coefficient for the f=0.25 case. As shown, in contrast to previously presented cases, here, two-peak waveforms are observed for all duty cycles. This behavior is observed in the drag and lift-to-drag ratio as well, as shown in Figure 4.44 and Figure 4.45. This phenomenon is discussed in detail in 4.3.

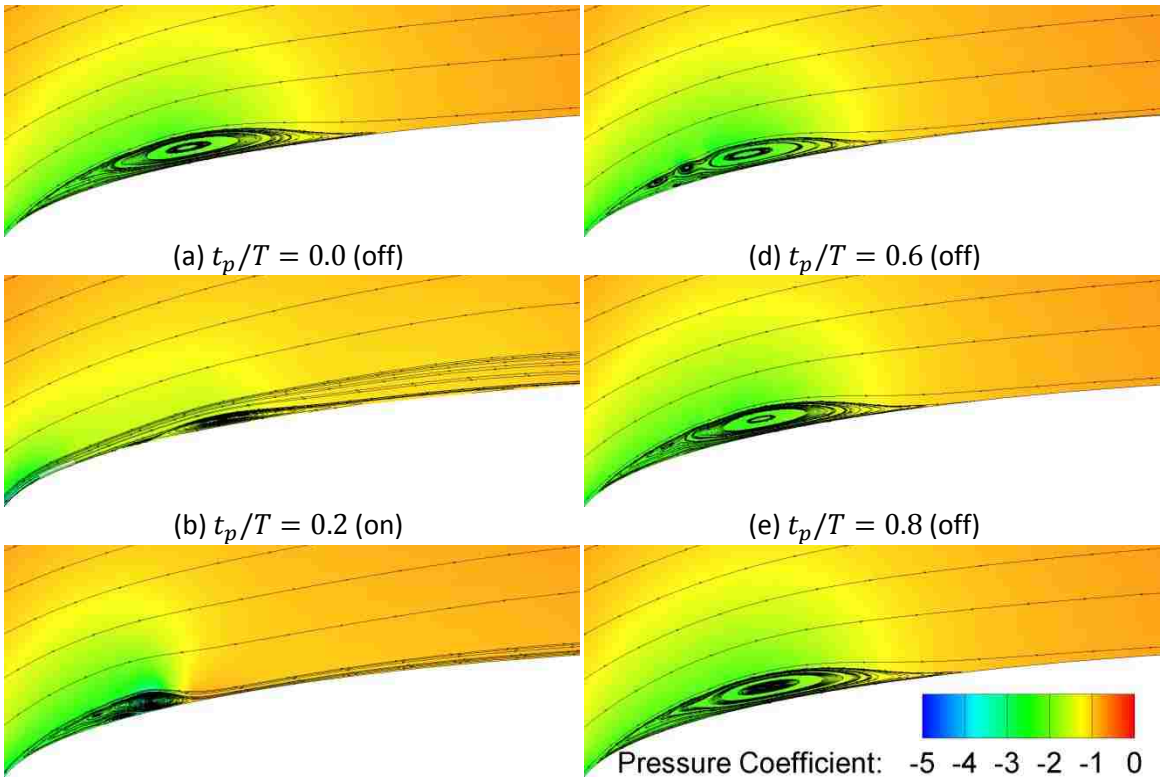

(a) $t_p/T = 0.0$ (off) (d) $t_p/T = 0.6$ (off)

(b) $t_p/T = 0.2$ (on) (e) $t_p/T = 0.8$ (off)

(c) $t_p/T = 0.4$ (off) (f) $t_p/T = 1.0$ (off)

Figure 4.35. Pressure coefficient contour and streamline distributions over 1 duty cycle (*f*=0.25, *D*=0.2)

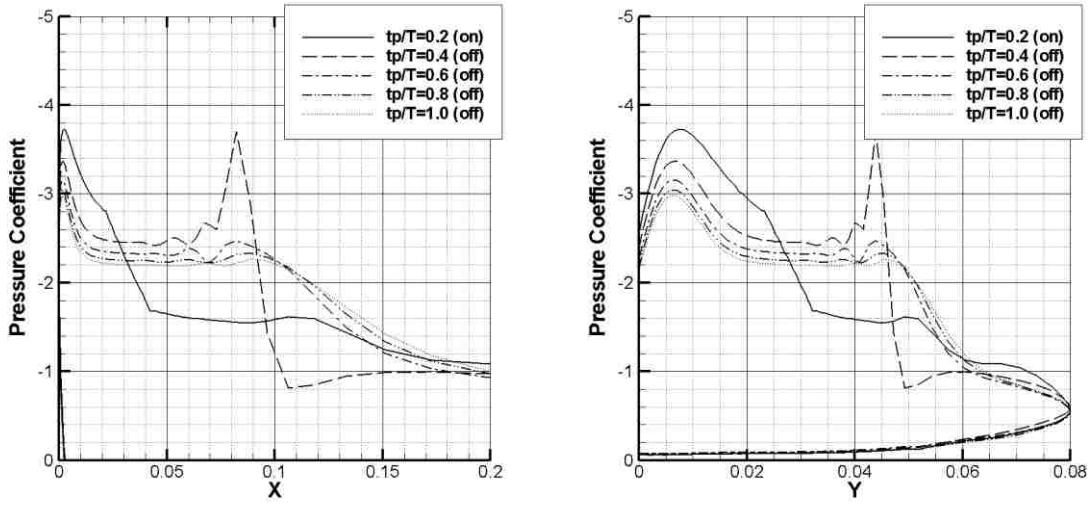

(a) C_p *vs. X* (b) C_p *vs. Y*

Figure 4.36. Influence of pulsed actuator on airfoil pressure distribution (*f*=0.25, *D*=0.2)

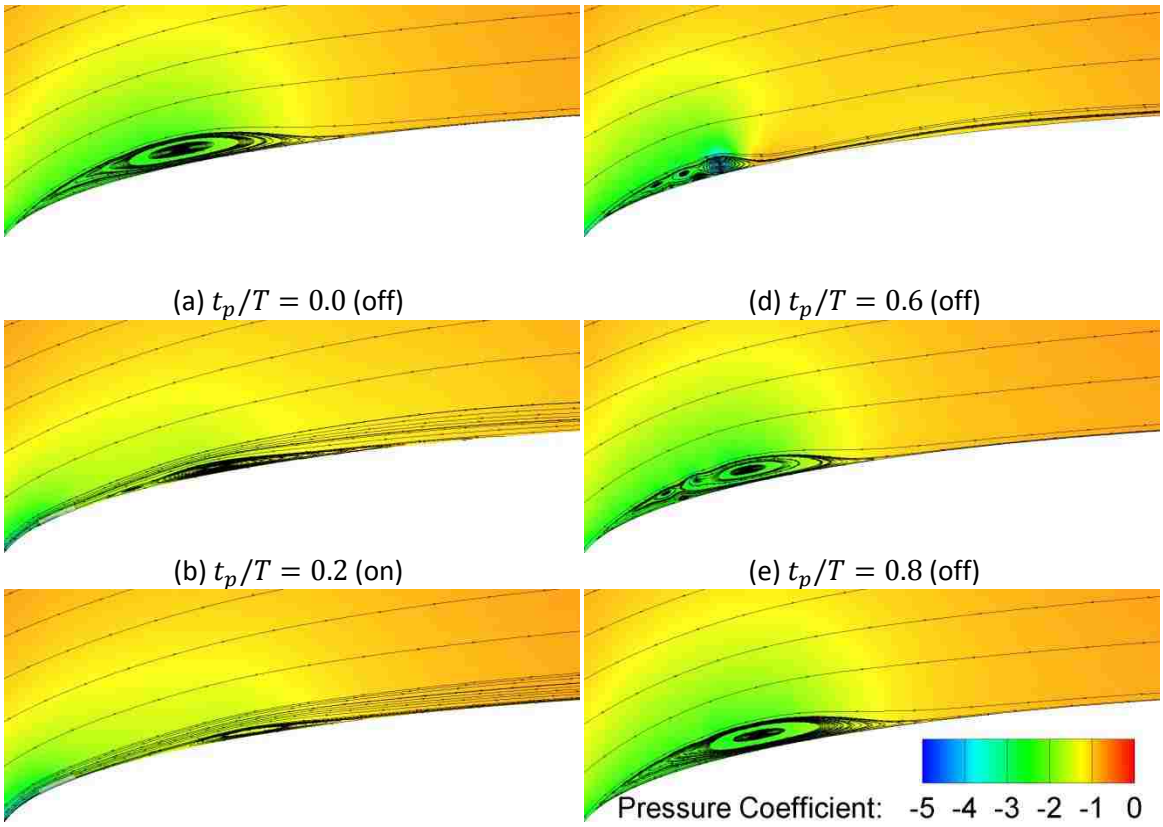

(a) $t_p/T = 0.0$ (off) (d) $t_p/T = 0.6$ (off)

(b) $t_p/T = 0.2$ (on) (e) $t_p/T = 0.8$ (off)

(c) $t_p/T = 0.4$ (on) (f) $t_p/T = 1.0$ (off)

Figure 4.37. Pressure coefficient contour and streamline distributions over 1 duty cycle (f=0.25, D=0.4)

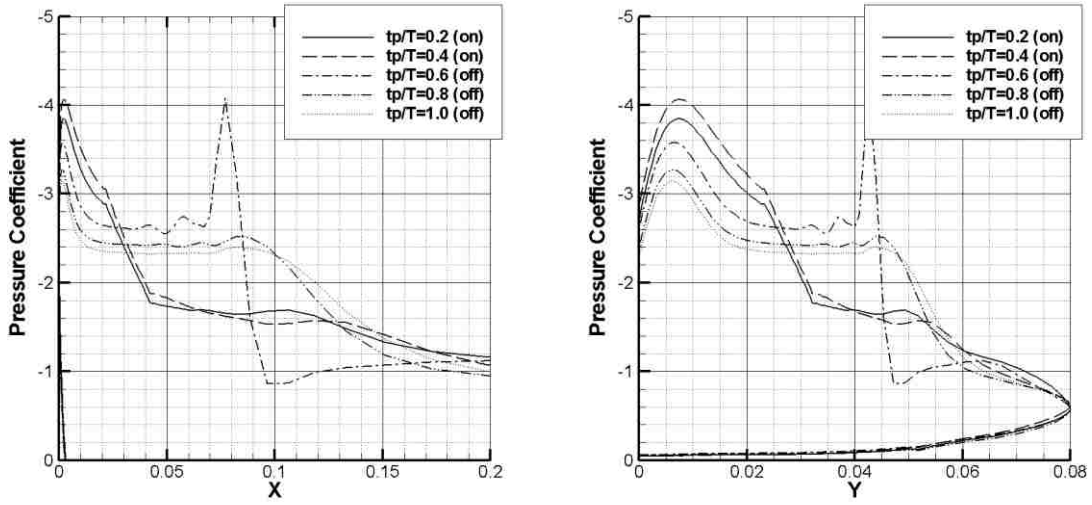

(a) C_p *vs. X* (b) C_p *vs. Y*

Figure 4.38. Influence of pulsed actuator on airfoil pressure distribution (f=0.25, D=0.4)

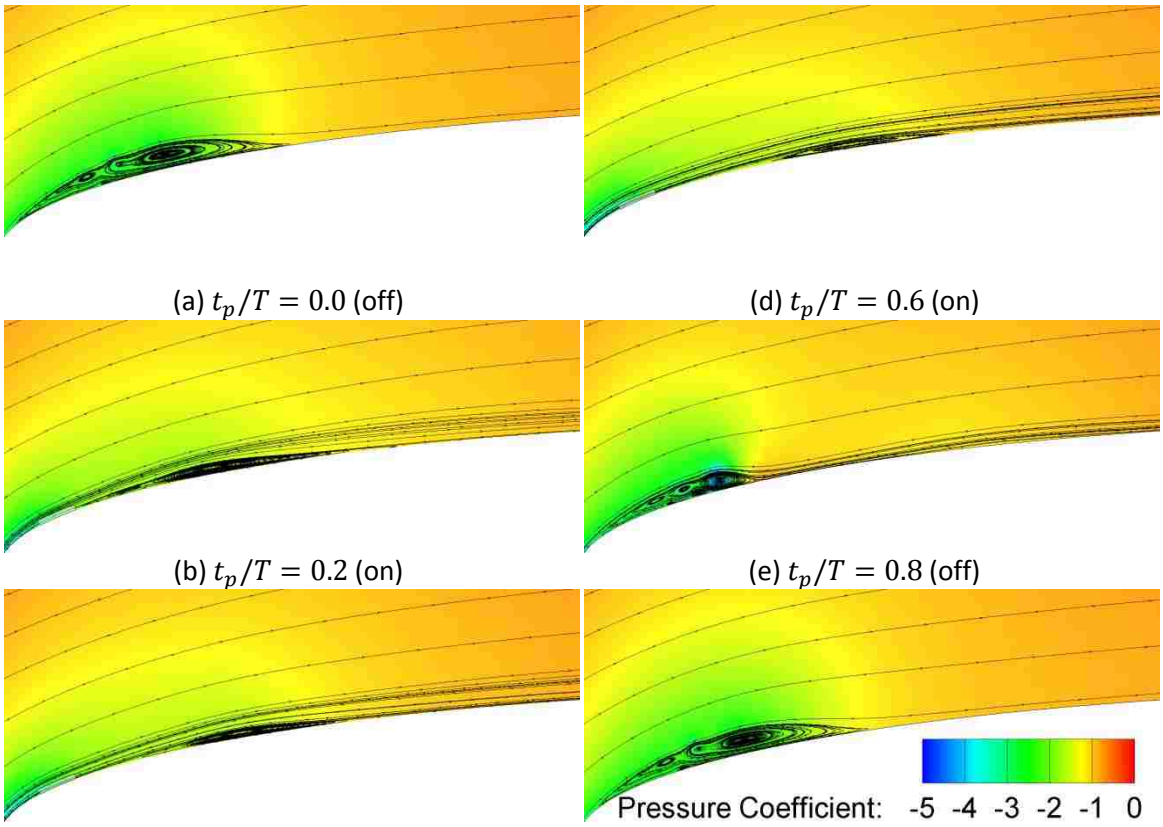

(a) $t_p/T = 0.0$ (off) (d) $t_p/T = 0.6$ (on)

(b) $t_p/T = 0.2$ (on) (e) $t_p/T = 0.8$ (off)

(c) $t_p/T = 0.4$ (on) (f) $t_p/T = 1.0$ (off)

Figure 4.39. Pressure coefficient contour and streamline distributions over 1 duty cycle (f=0.25, D=0.6)

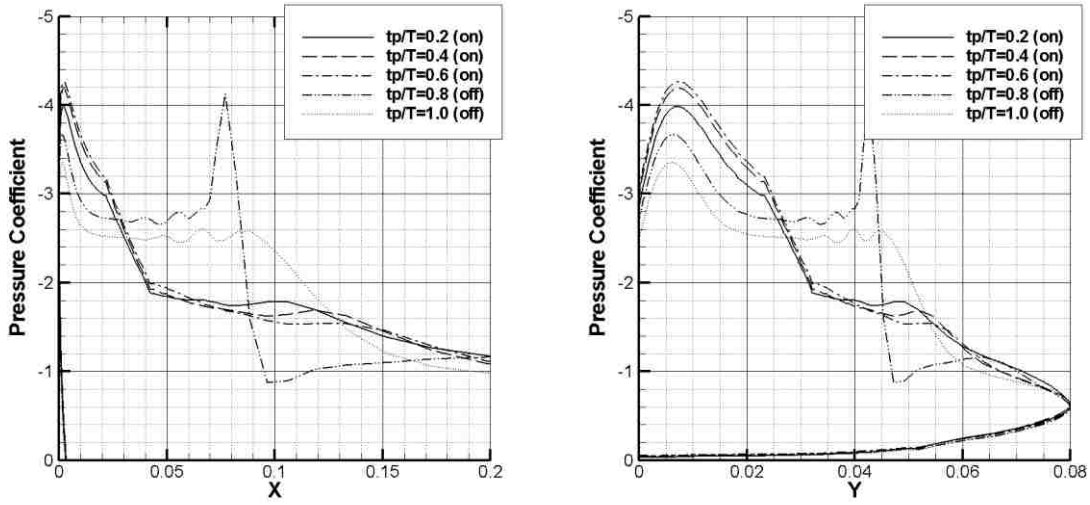

(a) C_p *vs. X* (b) C_p *vs. Y*

Figure 4.40. Influence of pulsed actuator on airfoil pressure distribution (f=0.25, D=0.6)

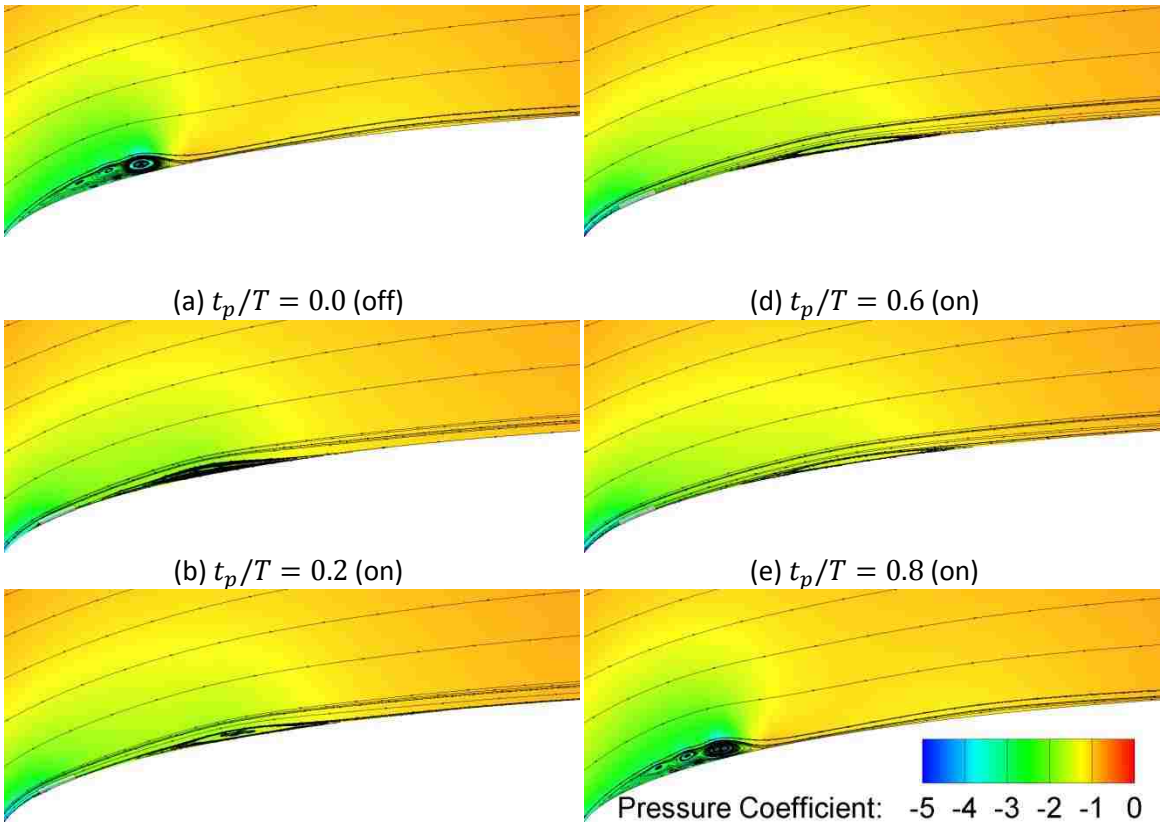

(a) $t_p/T = 0.0$ (off) (d) $t_p/T = 0.6$ (on)

(b) $t_p/T = 0.2$ (on) (e) $t_p/T = 0.8$ (on)

(c) $t_p/T = 0.4$ (on) (f) $t_p/T = 1.0$ (off)

Figure 4.41. Pressure coefficient contour and streamline distributions over 1 duty cycle (*f*=0.25, *D*=0.8)

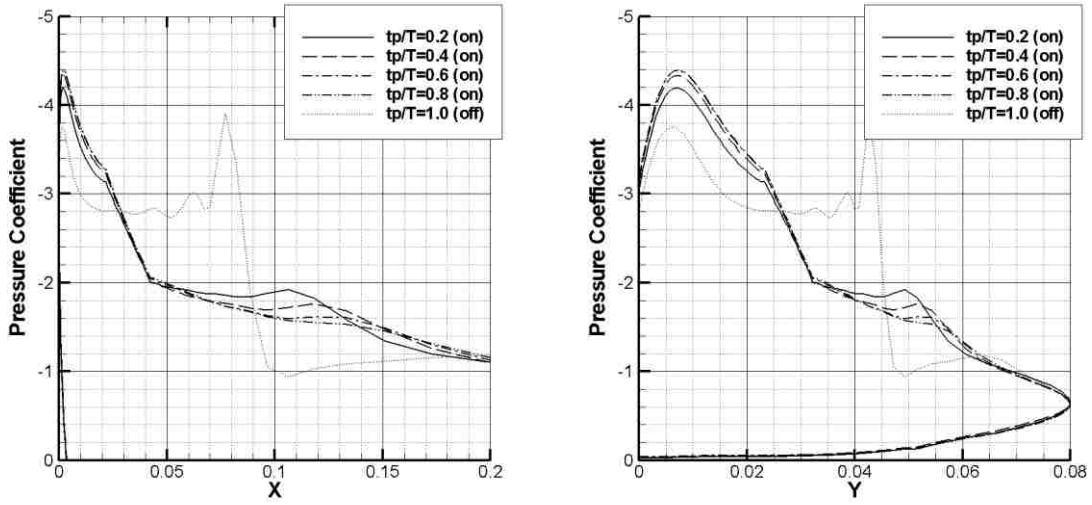

(a) C_p *vs. X* (b) C_p *vs. Y*

Figure 4.42. Influence of pulsed actuator on airfoil pressure distribution (*f*=0.25, *D*=0.8)

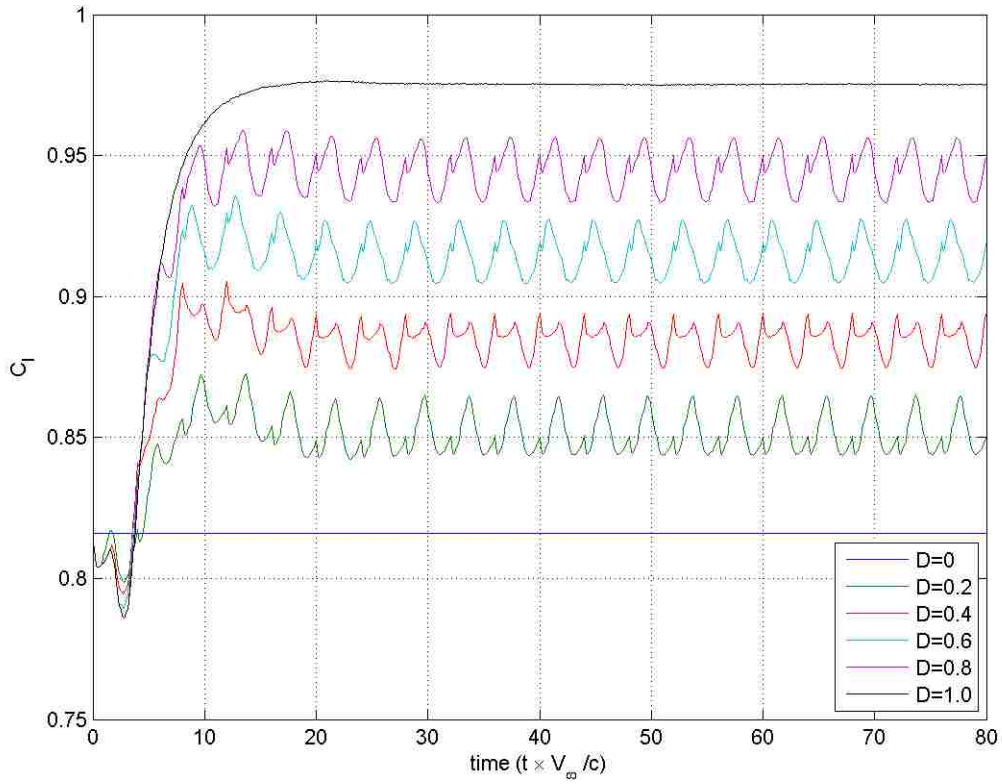

Figure 4.43. Transient response of lift coefficient to pulsed actuator (f = 0.25)

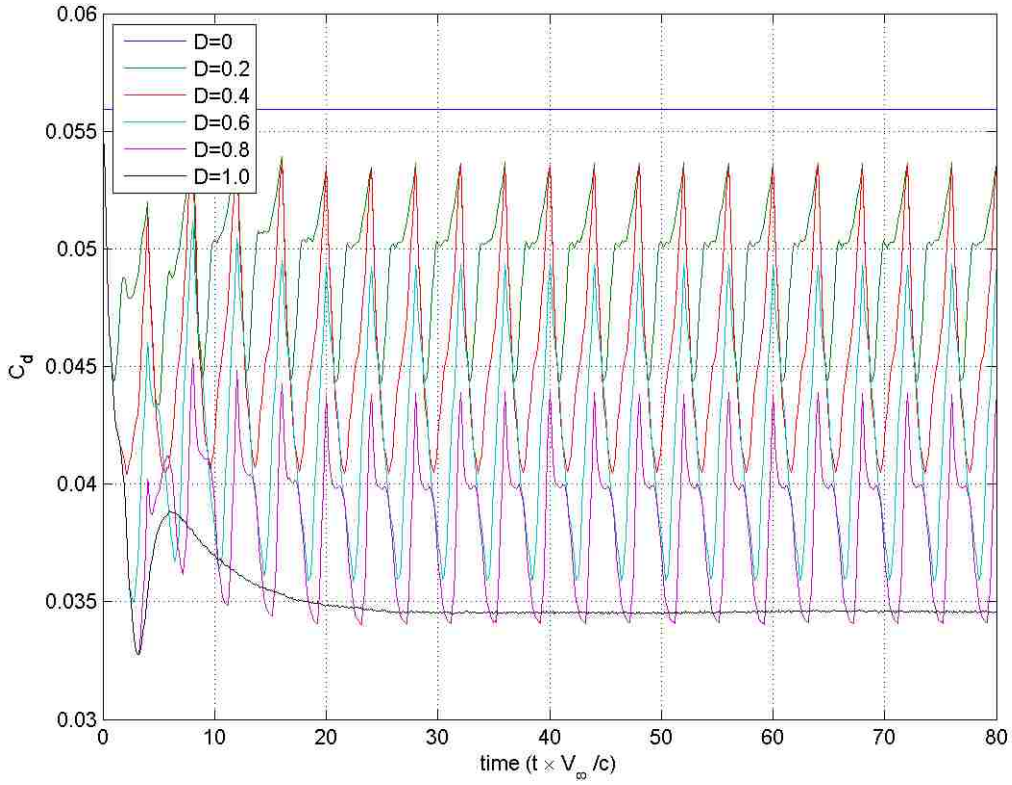

Figure 4.44. Transient response of drag coefficient to pulsed actuator (f = 0.25)

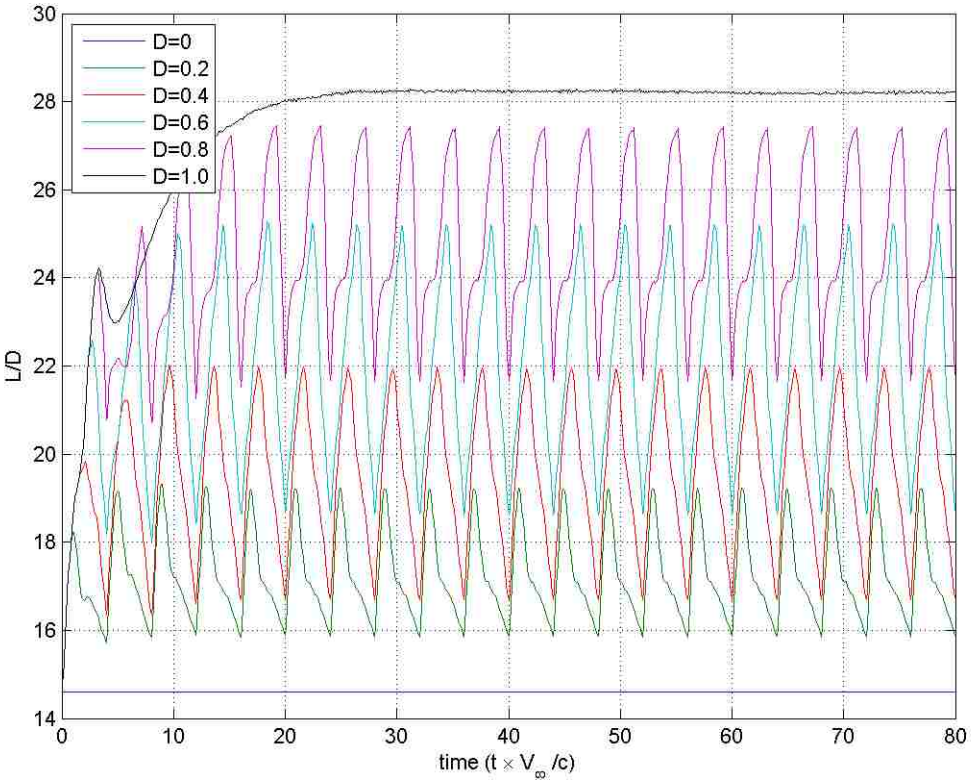

Figure 4.45. Transient response of lift to drag ratio to pulsed actuator (f = 0.25)

4.1.5. f=0.125 case. Figure 4.46 through Figure 4.53 give the flow-field developments and pressure distribution developments for f=0.125 and various duty cycles. As with numerous previous figures, these are provided as a reference, and will not be extensively commented on.

Figure 4.54, Figure 4.55 and Figure 4.56 give the transient response of the lift coefficient, drag coefficient, and lift-to-drag ratio for the f=0.125 case for various duty cycles. As shown, the multi-peak waveform phenomenon observed in 4.1.4 is also present, to a lesser extent in several of these cases. This is more thoroughly discussed in 4.3.

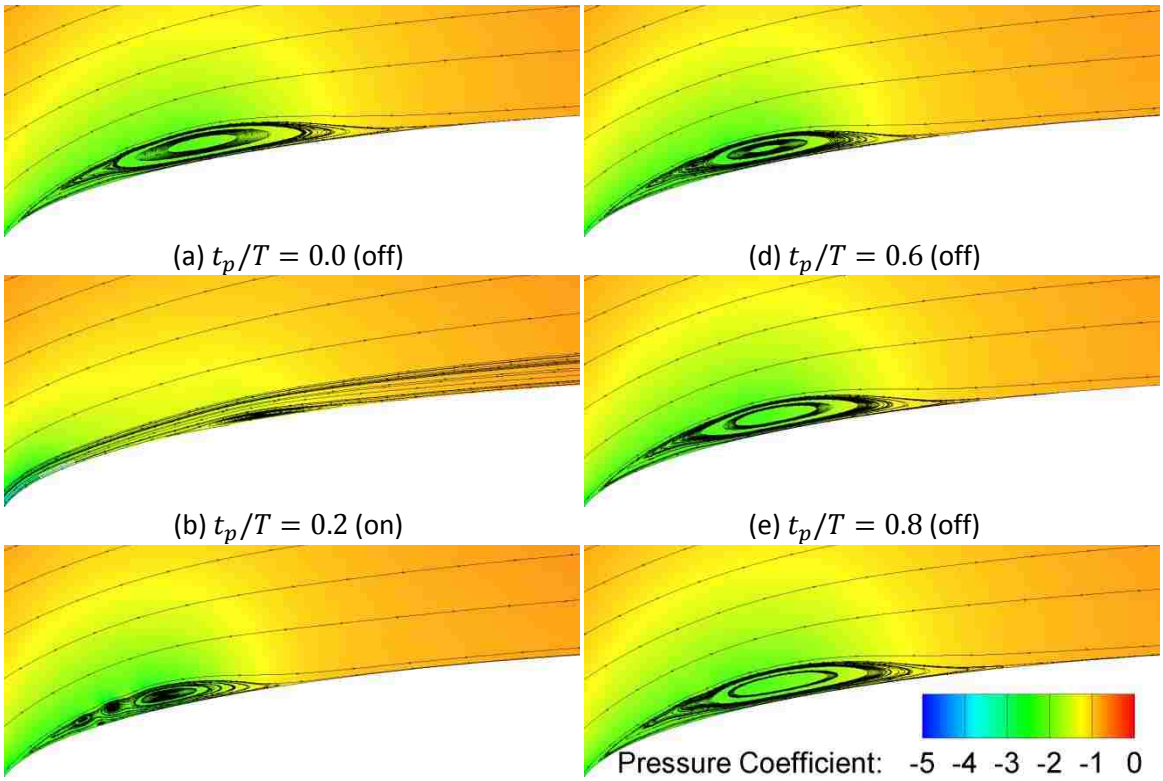

(a) $t_p/T = 0.0$ (off) (d) $t_p/T = 0.6$ (off)

(b) $t_p/T = 0.2$ (on) (e) $t_p/T = 0.8$ (off)

(c) $t_p/T = 0.4$ (off) (f) $t_p/T = 1.0$ (off)

Figure 4.46. Pressure coefficient contour and streamline distributions over 1 duty cycle (f=0.125, D=0.2)

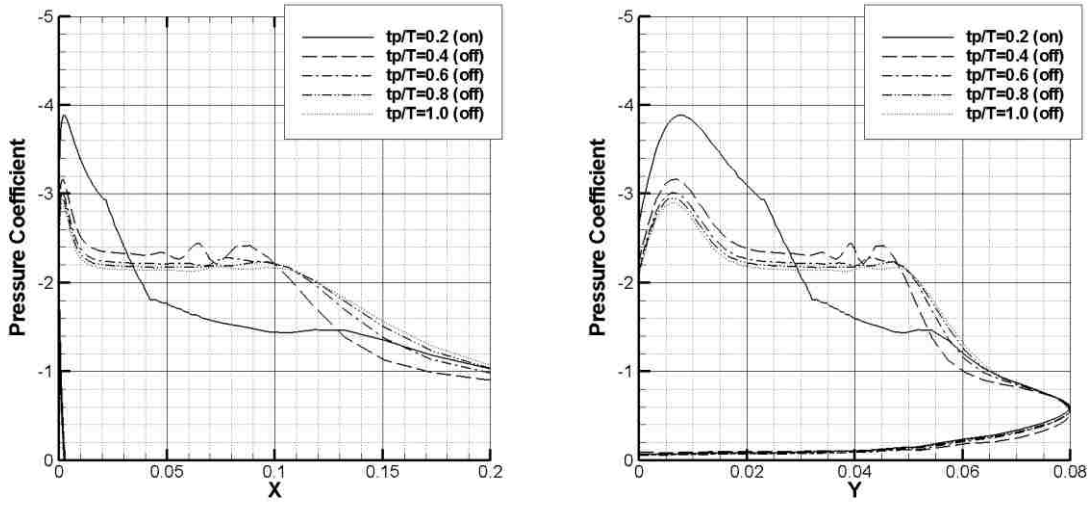

(a) C_p *vs. X* (b) C_p *vs. Y*

Figure 4.47. Influence of pulsed actuator on airfoil pressure distribution (f=0.125, D=0.2)

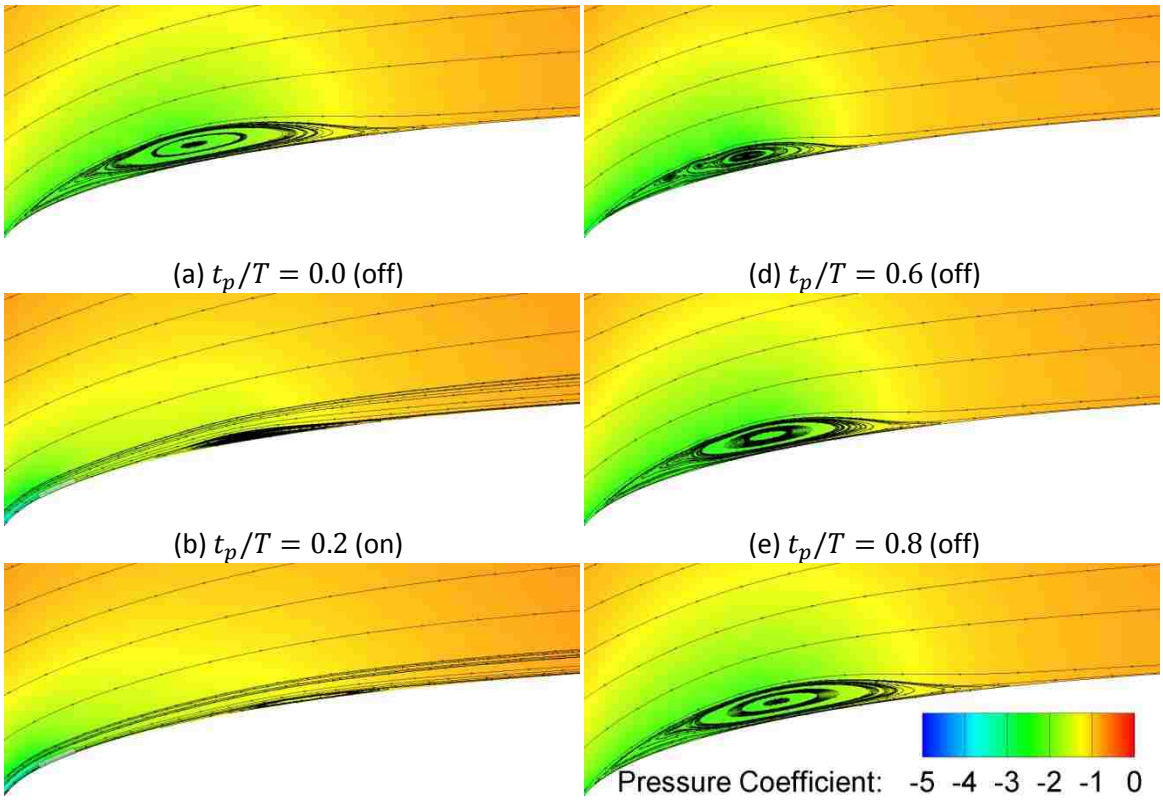

(a) $t_p/T = 0.0$ (off) (d) $t_p/T = 0.6$ (off)

(b) $t_p/T = 0.2$ (on) (e) $t_p/T = 0.8$ (off)

(c) $t_p/T = 0.4$ (on) (f) $t_p/T = 1.0$ (off)

Figure 4.48. Pressure coefficient contour and streamline distributions over 1 duty cycle (f=0.125, D=0.4)

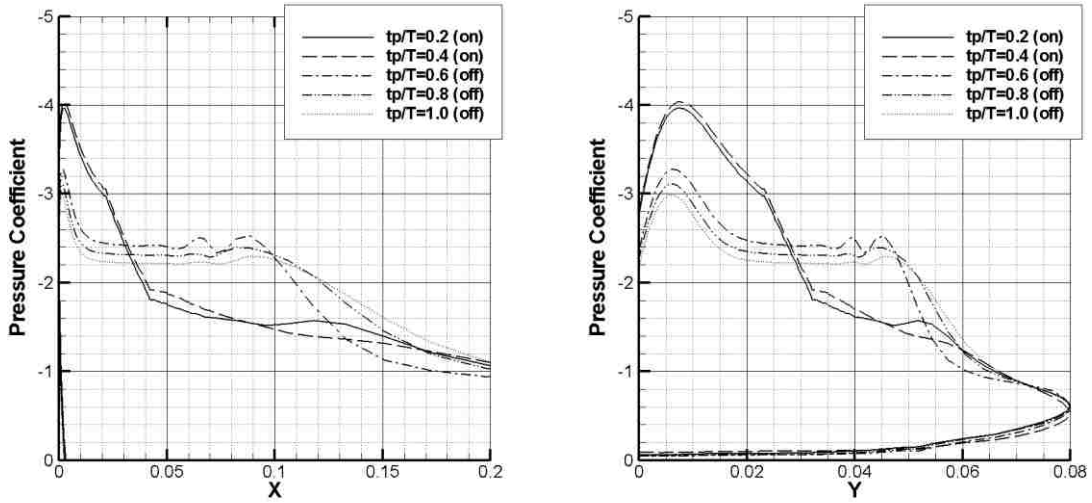

(a) C_p *vs. X* (b) C_p *vs. Y*

Figure 4.49. Influence of pulsed actuator on airfoil pressure distribution (f=0.125, D=0.4)

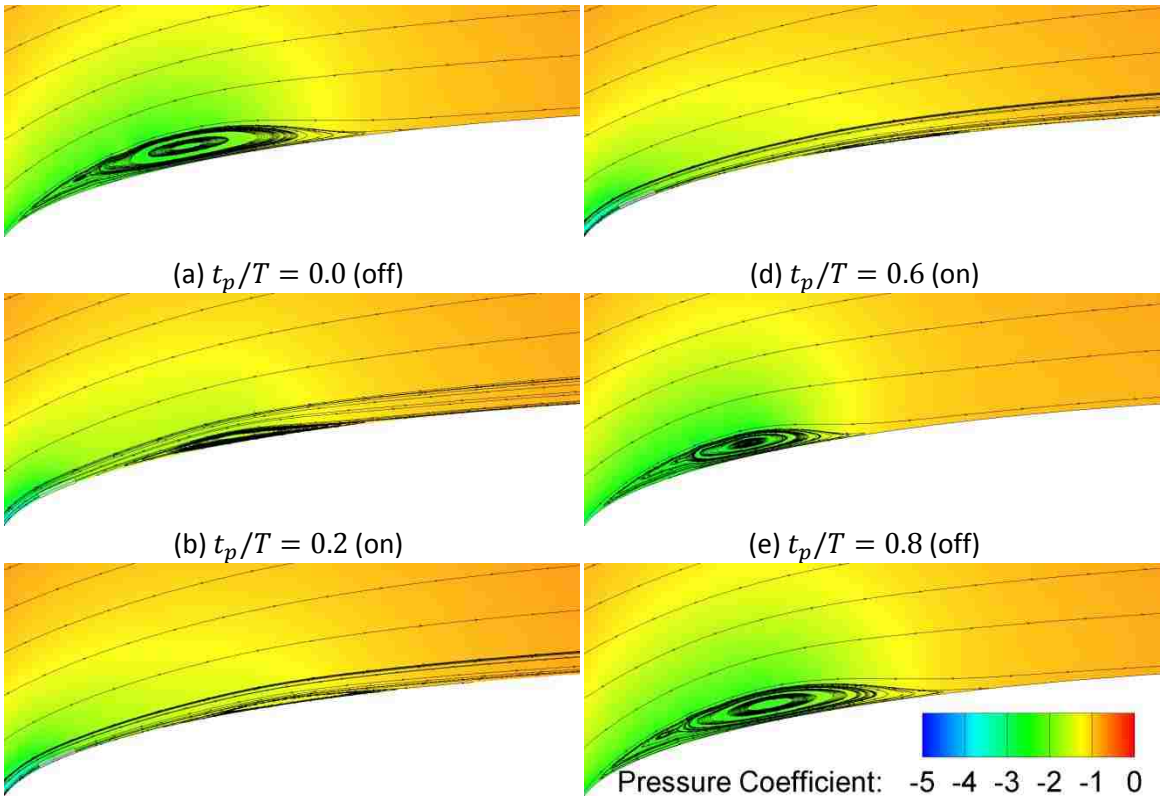

(a) $t_p/T = 0.0$ (off) (d) $t_p/T = 0.6$ (on)

(b) $t_p/T = 0.2$ (on) (e) $t_p/T = 0.8$ (off)

(c) $t_p/T = 0.4$ (on) (f) $t_p/T = 1.0$ (off)

Figure 4.50. Pressure coefficient contour and streamline distributions over 1 duty cycle (f=0.125, D=0.6)

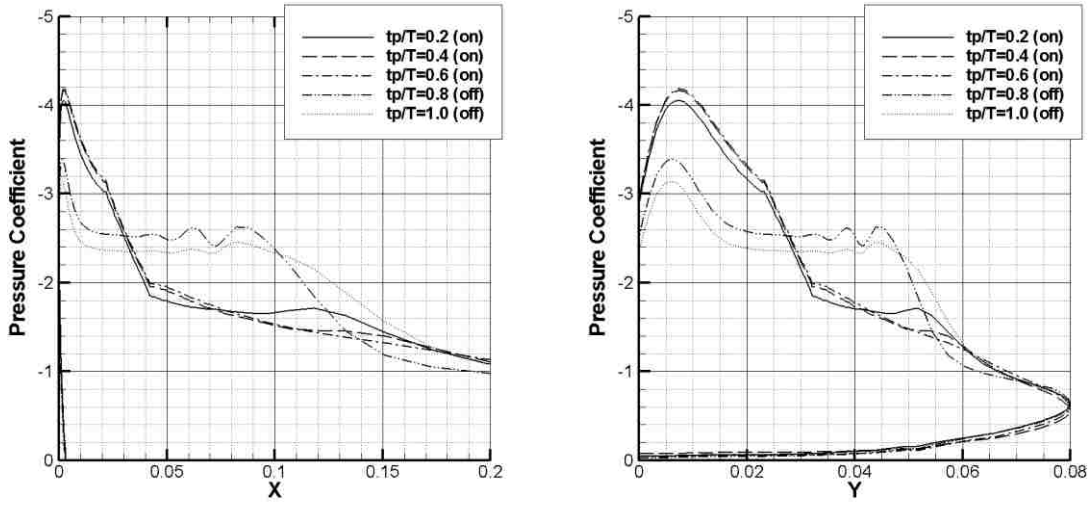

(a) C_p *vs. X* (b) C_p *vs. Y*

Figure 4.51. Influence of pulsed actuator on airfoil pressure distribution (f=0.125, D=0.6)

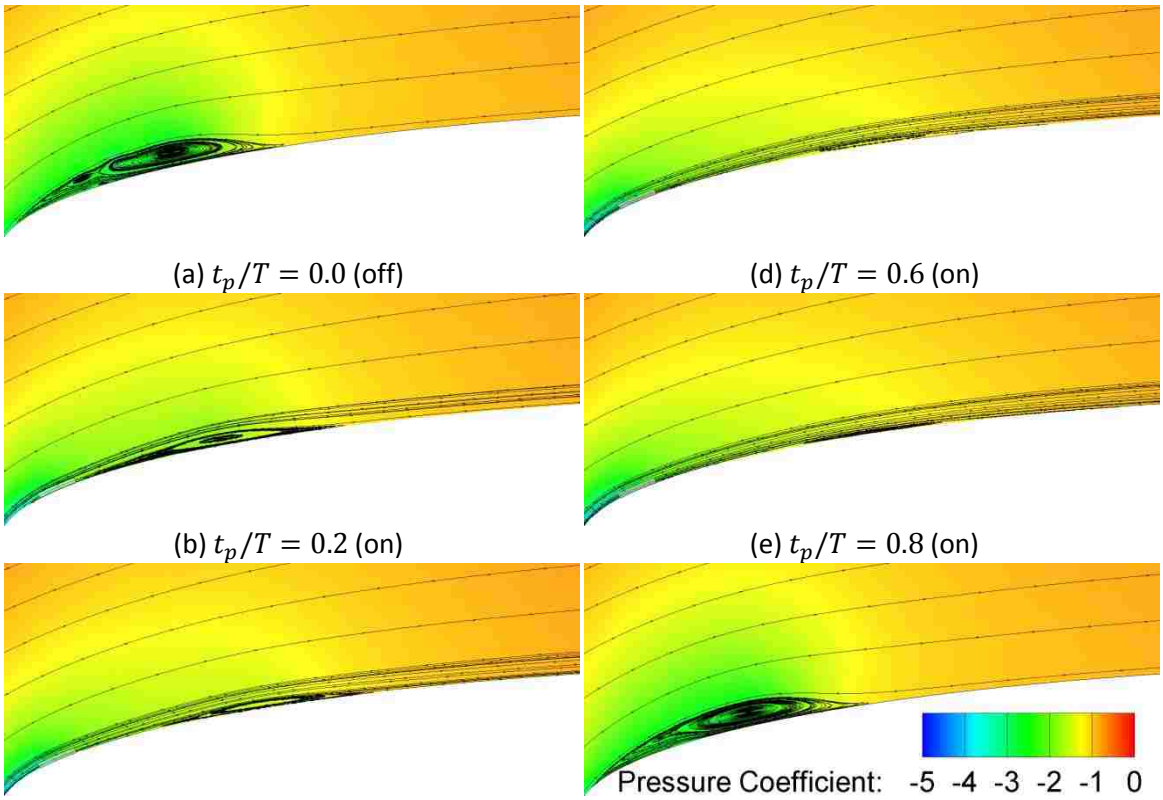

(a) $t_p/T = 0.0$ (off) (d) $t_p/T = 0.6$ (on)

(b) $t_p/T = 0.2$ (on) (e) $t_p/T = 0.8$ (on)

(c) $t_p/T = 0.4$ (on) (f) $t_p/T = 1.0$ (off)

Figure 4.52. Pressure coefficient contour and streamline distributions over 1 duty cycle (f=0.125, D=0.8)

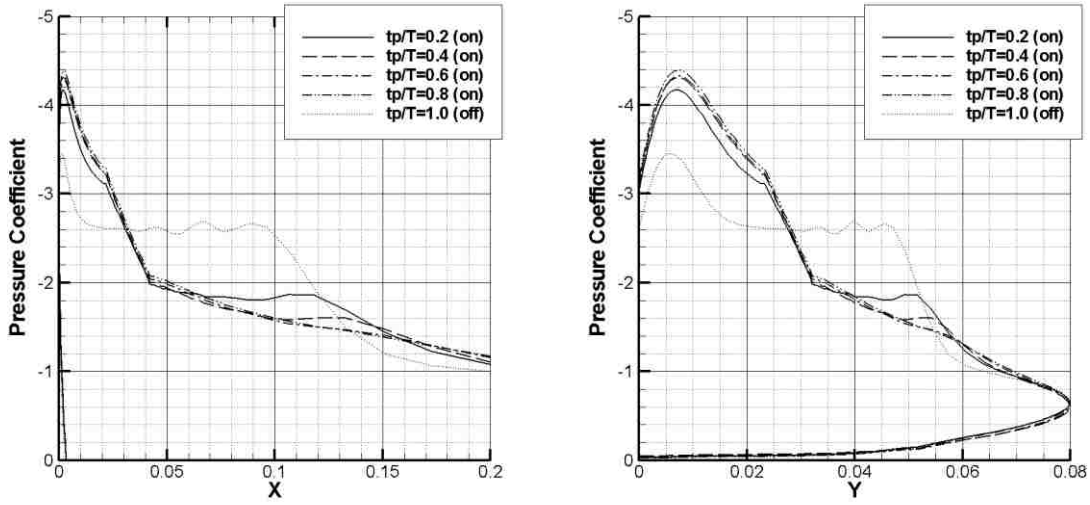

(a) C_p *vs. X* (b) C_p *vs. Y*

Figure 4.53. Influence of pulsed actuator on airfoil pressure distribution (f=0.125, D=0.8)

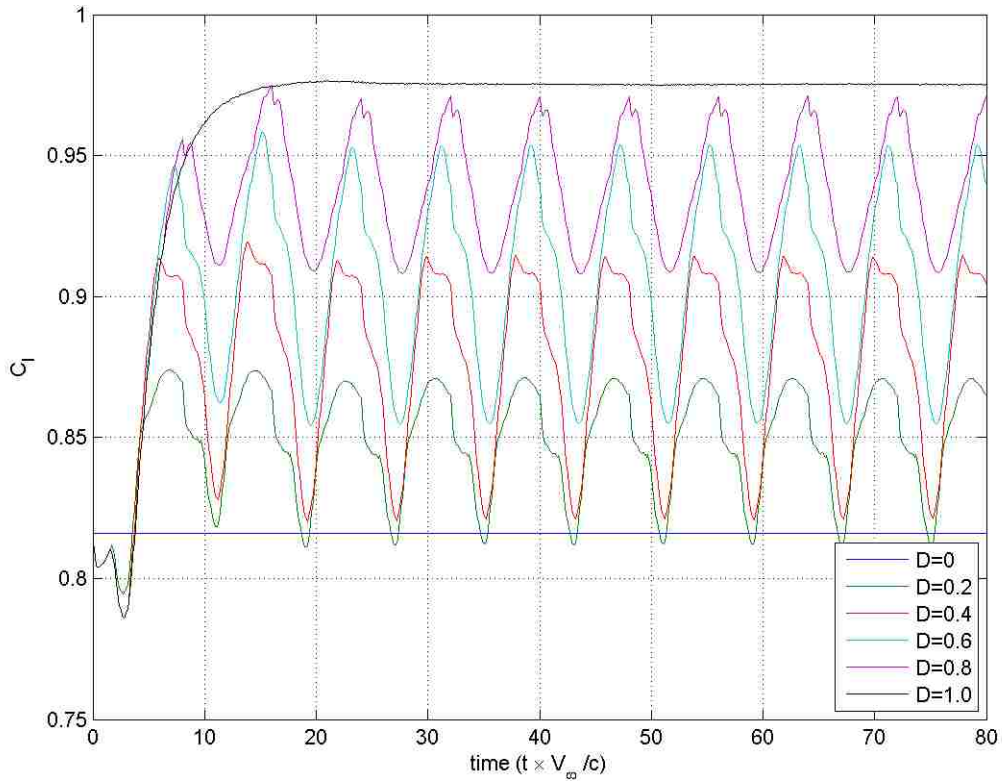

Figure 4.54. Transient response of lift coefficient to pulsed actuator (f = 0.125)

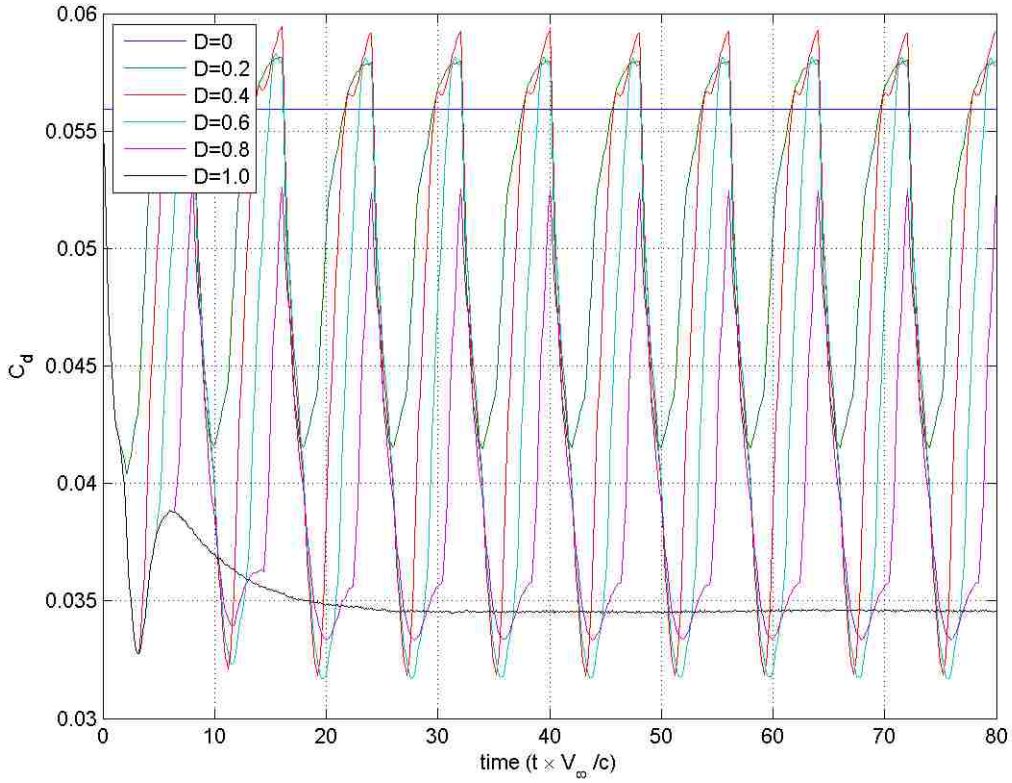

Figure 4.55. Transient response of drag coefficient to pulsed actuator (f = 0.125)

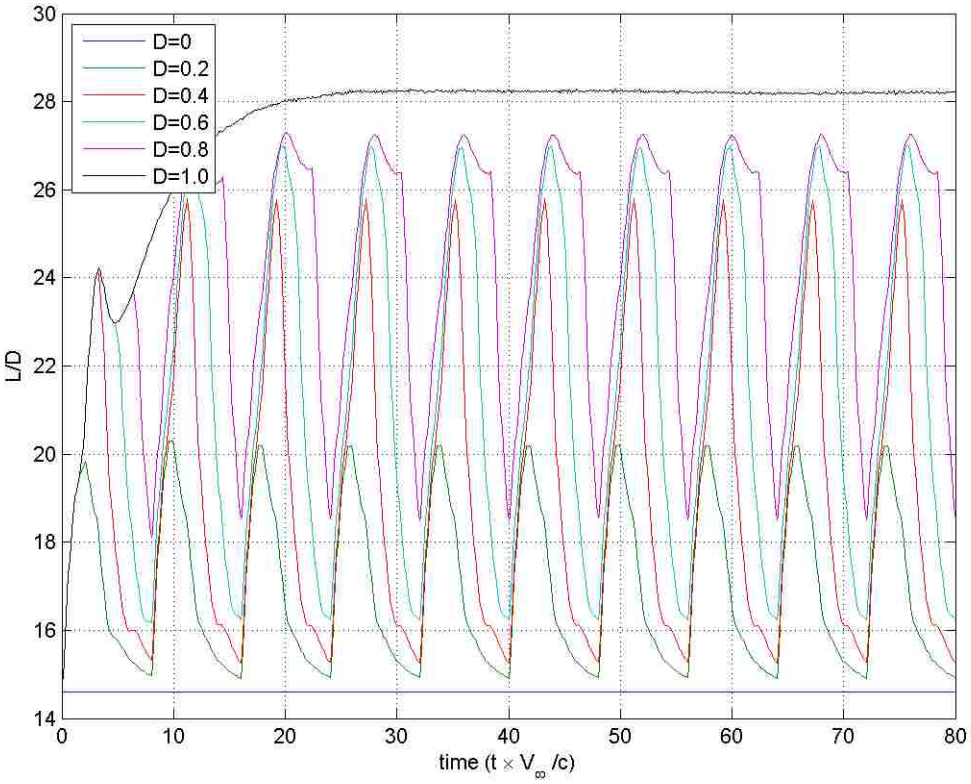

Figure 4.56. Transient response of lift to drag ratio to pulsed actuator (f = 0.125)

4.1.6. Effect of actuator frequency on periodic flow developments.

Figure 4.57 and Figure 4.58 are provided, below, to illustrate how flow-field developments are affected by actuator frequency. The left and right columns of Figure 4.57 compare the flow developments observed over one actuation period for the f=2.0 and f=0.125 cases with D=0.2. The same is shown in Figure 4.58 with D=0.8.

Immediately evident in these figures is the fact that higher frequency actuation results in more successful suppression of the LSB. Unsurprisingly, because the LSB is larger at any given point in the period at lower frequencies, the suction peak associated with the LSB is characteristically broader. However, it is also apparent from visual observation that the *intensity* of the peak is much lower at lower frequencies. Because these two effects counteract each other, it is not clear what relationship exists between frequency and net lift production.

Another effect shown in these figures is that the intensity of the airfoil's leading edge suction peak is higher, on average, at the higher frequency. This suction would be expected to result in lower pressure drag at higher frequencies, which would also be expected to result in higher lift-to-drag ratios. This prediction will be confirmed in chapter 4.2, where the mean lift coefficient, drag coefficient, and lift-to-drag ratio are tabulated as functions of f and D.

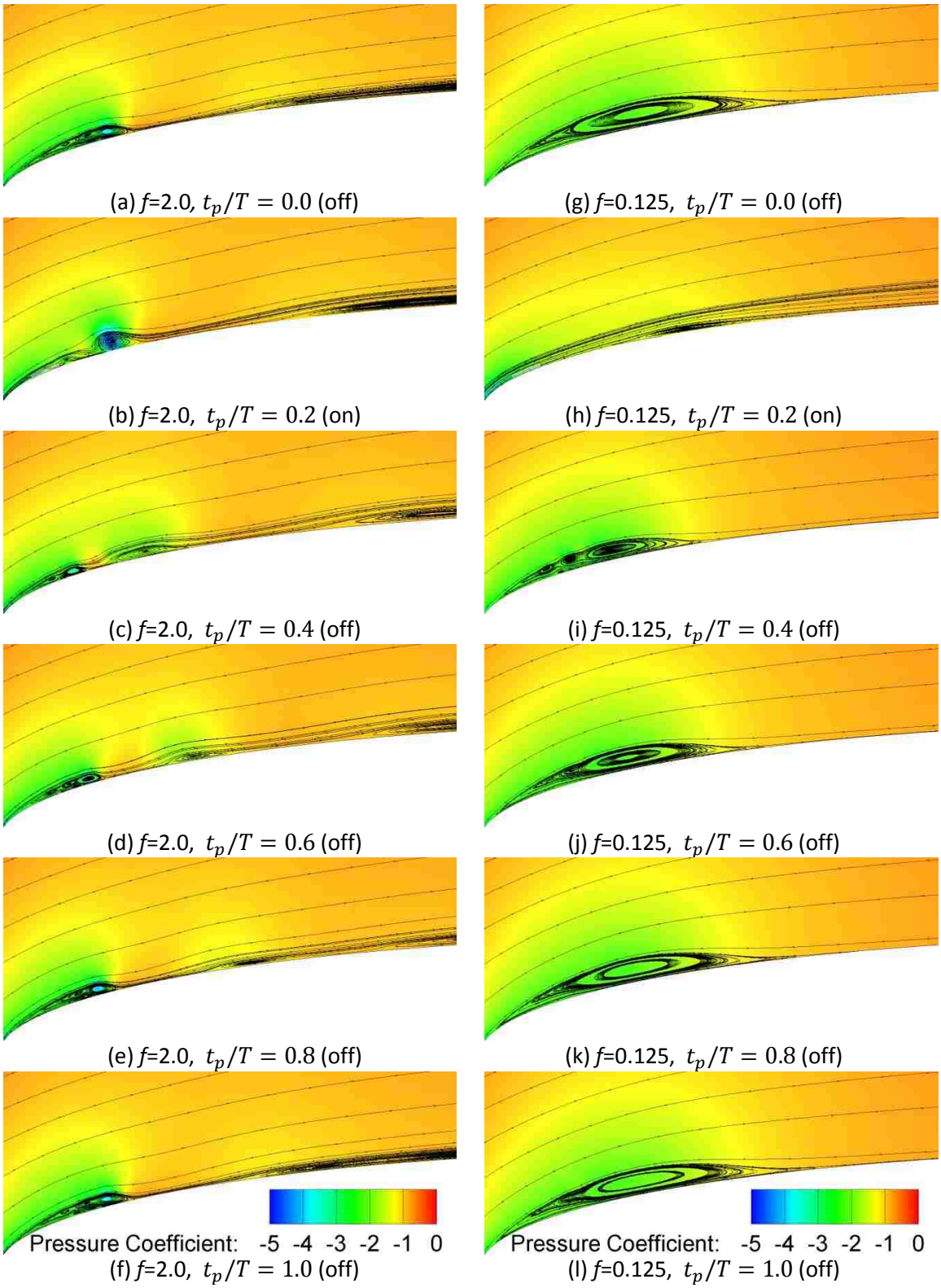

Figure 4.57. Comparison between flow developments of f=2.0 and f=0.125 cases (D=0.2)

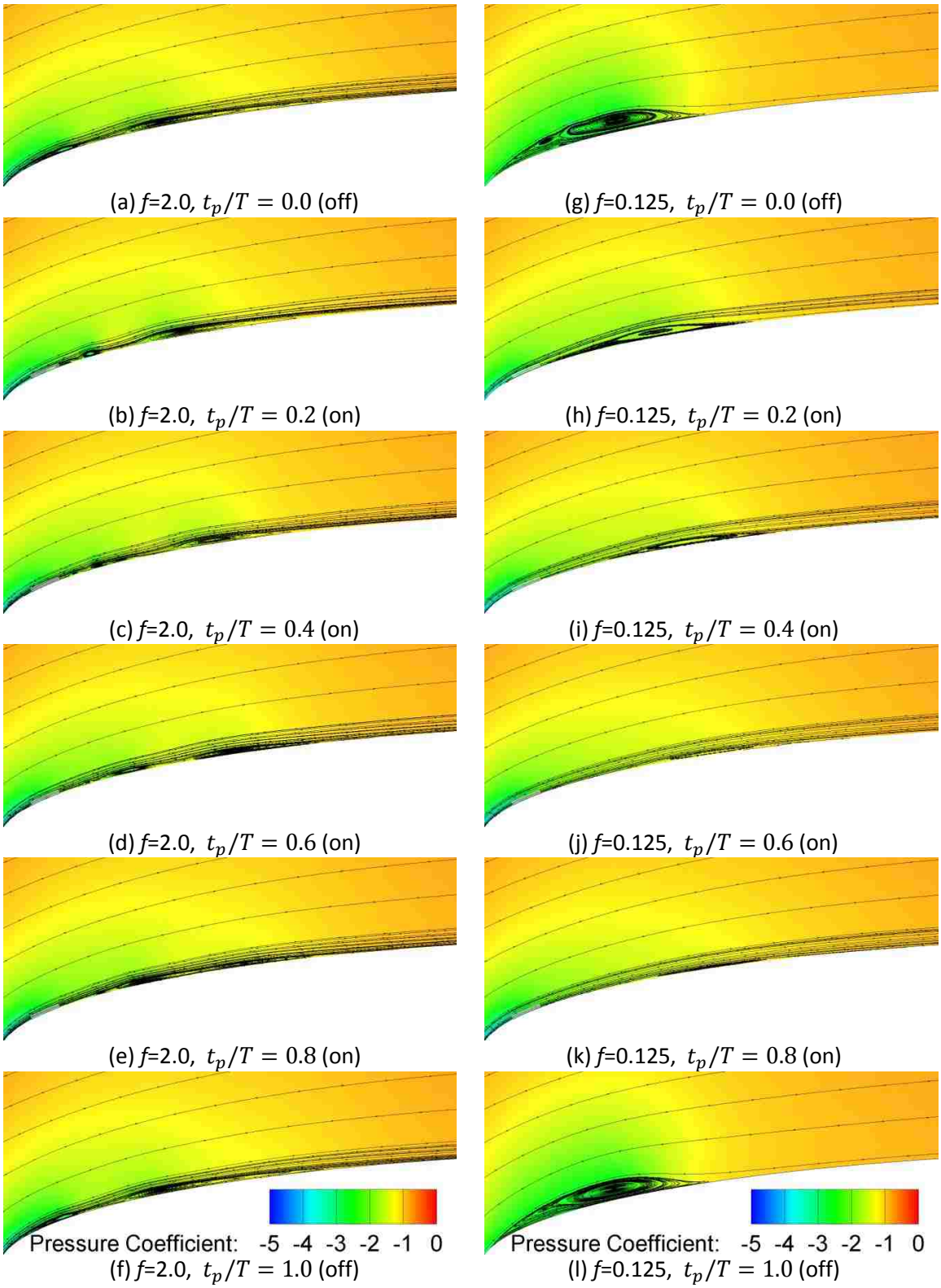

Figure 4.58. Comparison between flow developments of f=2.0 and f=0.125 cases (D=0.8)

4.2. QUANTITATIVE INVESTIGATION OF UNSTEADY EFFECTS OF PULSED ACTUATOR

To examine the effect that the aforementioned flow developments may have on the airfoil aerodynamic characteristics, the unsteady response of the lift, drag, and lift-to-drag ratio of the airfoil are observed. To compare results obtained under different frequencies and duty cycles, the coefficients are averaged over one duty cycle, once quasi-equilibrium has been achieved. The effectiveness of the actuator is then evaluated under a variety of frequencies and duty cycles to find the conditions under which actuator effectiveness is optimized.

4.2.1. Influence of actuator frequency and duty cycle on airfoil lift characteristics. The effectiveness of a pulsed actuator in lift enhancement is discussed here. Figure 4.59 shows the dependence of the time-averaged lift coefficient on actuator frequency for various duty cycles. For reference, the nominal and steady actuator cases are also plotted. As previously mentioned, the average lift coefficient increases as the duty cycle is increased, regardless of frequency. However, the degree of C_l improvement over the reference case is not easily predictable with respect to frequency and duty cycle. As shown, for the D=0.8 case, steady improvement in the lift coefficient is observed as actuator frequency is increased. However, no such trend is exhibited by the other three cases plotted.

To estimate the effectiveness of the actuator based on power requirements, the time-averaged results previously obtained were compared to the steady state cases corresponding to equivalent mean power requirements. According to Mertz [33], a plasma actuator's input power requirement is roughly proportional to the body force the actuator produces for a given actuator. It logically follows that the required power for a pulsed actuator is proportional to the body force magnitude multiplied by the duty cycle. Hence, an actuator with f_{nd}=20 and D=0.2 would be expected to require roughly the same long-term power requirements as a steady actuator of f_{nd}=4, etc. By dividing the time-averaged lift, drag, or lift-to-drag ratio by that of the power-equivalent steady case, we obtain a rough measure of the effectiveness of a pulsing actuator for each unsteady case. This allows the direct comparison between results obtained at all duty cycles. As shown in Figure 4.60, pulsing the actuator does not result in significant lift enhancement

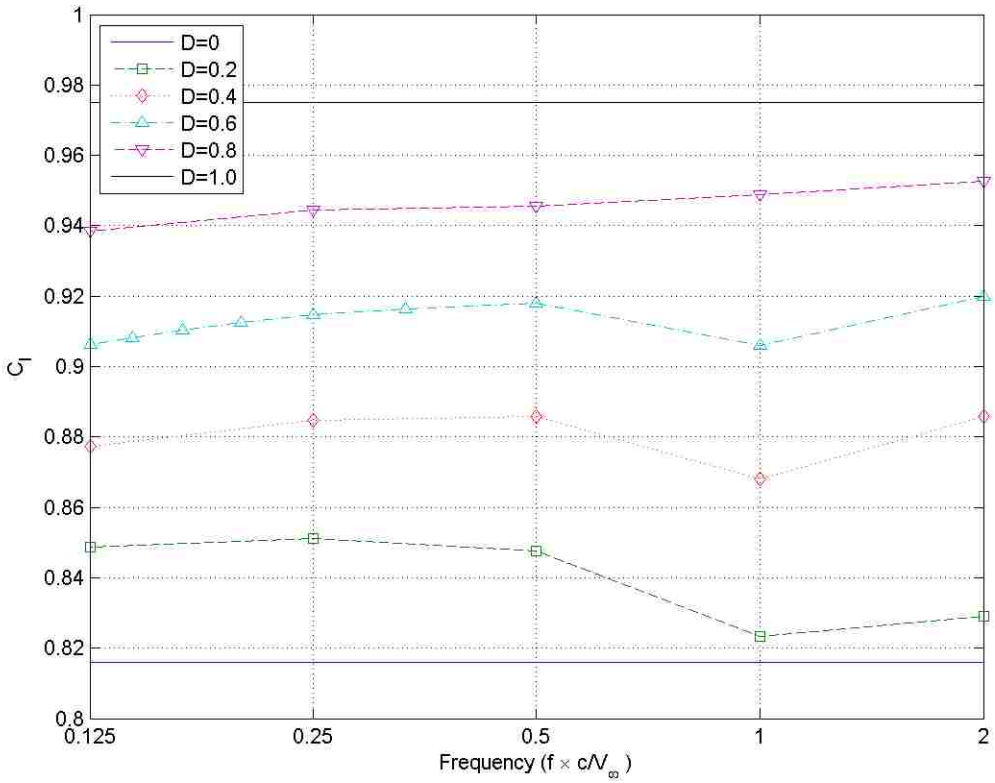

Figure 4.59. Dependence of mean lift coefficient on actuator frequency and duty cycle (f_{nd} = *20)*

(or degradation) under any conditions within the observed parameter space. As shown, the obtained mean lift coefficients generally lie within ±4 percent of the steady power-equivalent values. This indicates that a pulsed actuator may not be appreciably more effective than a steady actuator in terms of lift enhancement.

4.2.2. Influence of actuator frequency and duty cycle on airfoil drag characteristics. The effects of a pulsed actuator on airfoil drag are observed in this section. As was done with the lift coefficient, the average drag coefficient was taken over the course of a single period under each condition. Figure 4.61 shows the dependence of the time-averaged C_d on frequency for various duty cycles. Despite a great deal of variability in the unsteady results shown previously, the time-averaged results are fairly well-behaved. In Figure 4.61, it is clearly shown that as the actuation frequency is increased, the average drag coefficient decreases, regardless of *D*.

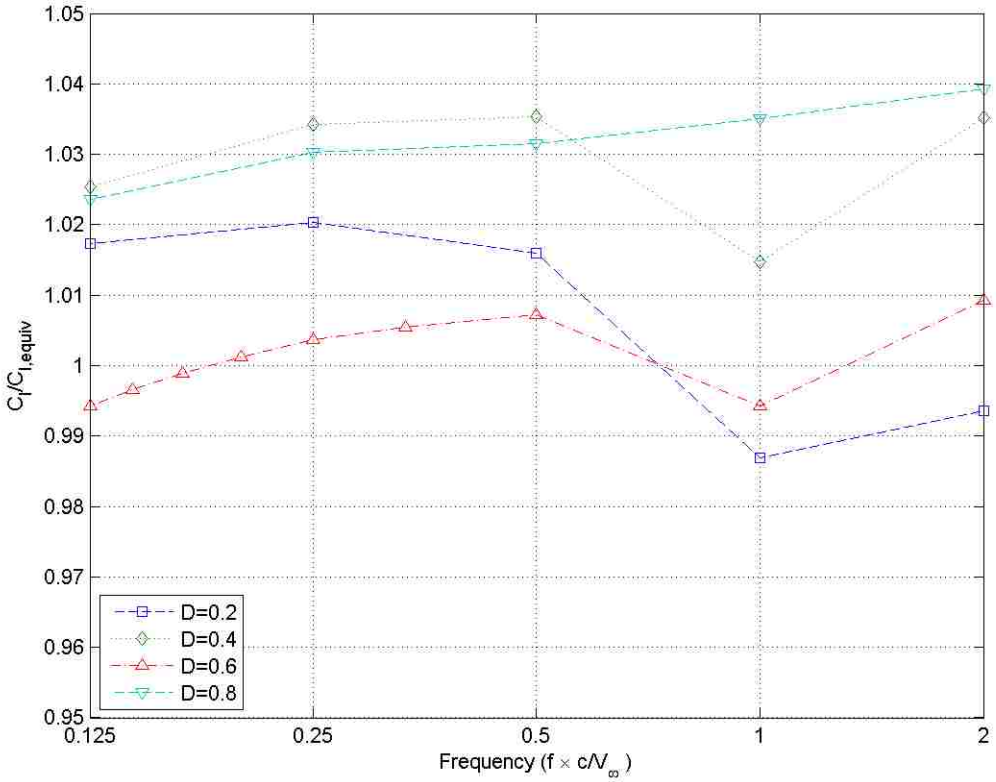

Figure 4.60. Lift enhancement as function of frequency and duty cycle

To evaluate the drag reduction capabilities of the actuator with respect to power requirements and compare results at various duty cycles, the time-averaged drag coefficient was divided by the case's power-equivalent steady drag coefficient, as described previously in 4.2.1, allowing the estimation of actuator effectiveness in drag reduction and comparison between results of various duty cycles. As Figure 4.62 shows, there are clear advantages of pulsed over steady-state actuation. As shown, for the range of duty cycles shown, there exists a 7-13 percent reduction in drag at the f=2.0 case. However, no general trend is observed regarding the dependence of effectiveness on duty cycle. Under the optimal case (f=2.0, D=0.4), the drag is approximately 13 percent lower than the power-equivalent steady value. It is evident that a pulsed actuator may be effective in drag reduction if pulsed at high frequencies, but more work is required to determine the relationship between drag reduction and duty cycle.

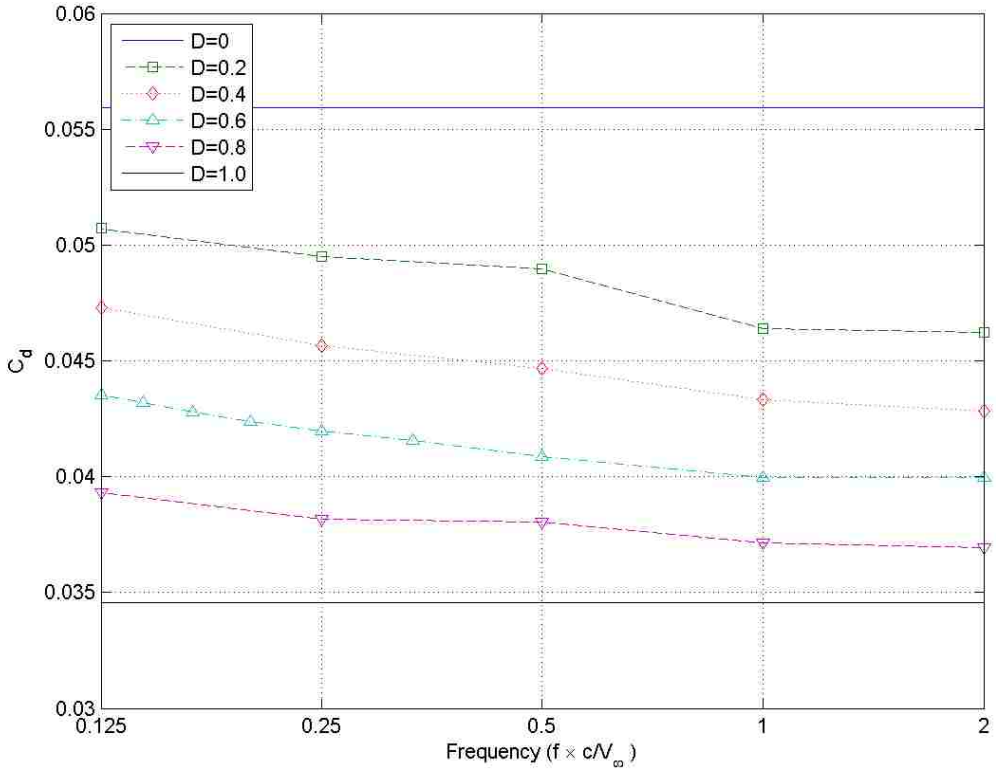

Figure 4.61. Dependence of mean drag coefficient on actuator frequency and duty cycle (f_{nd} =20)

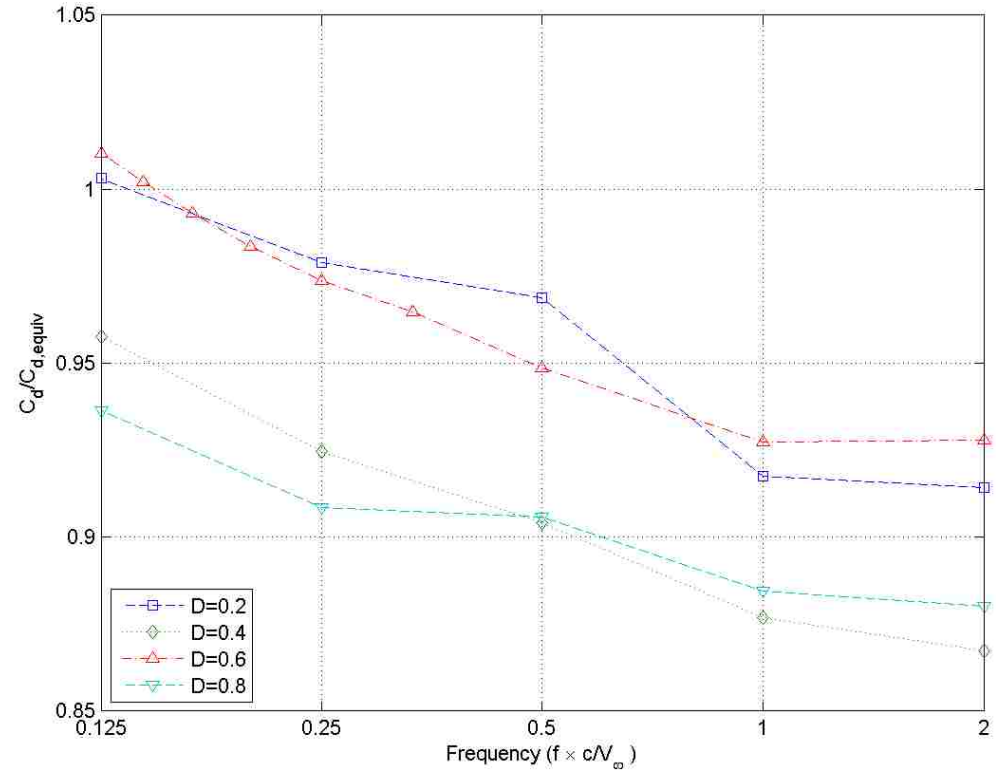

Figure 4.62. Drag enhancement as function of frequency and duty cycle

4.2.3. Influence of actuator frequency and duty cycle on airfoil lift to drag ratio. To quantify the net effect of the actuator on airfoil efficiency, the dependence of the lift-to-drag ratio on actuator frequency and duty cycle is examined. Figure 4.63 shows the dependence of the time-averaged quasi-equilibrium lift-to-drag ratio on frequency for all duty cycles observed in this analysis. As shown, regardless of duty cycle, as the actuation frequency is increased, moderate improvements in the lift-to-drag ratio are observed. This is in line with the observations previously made regarding drag.

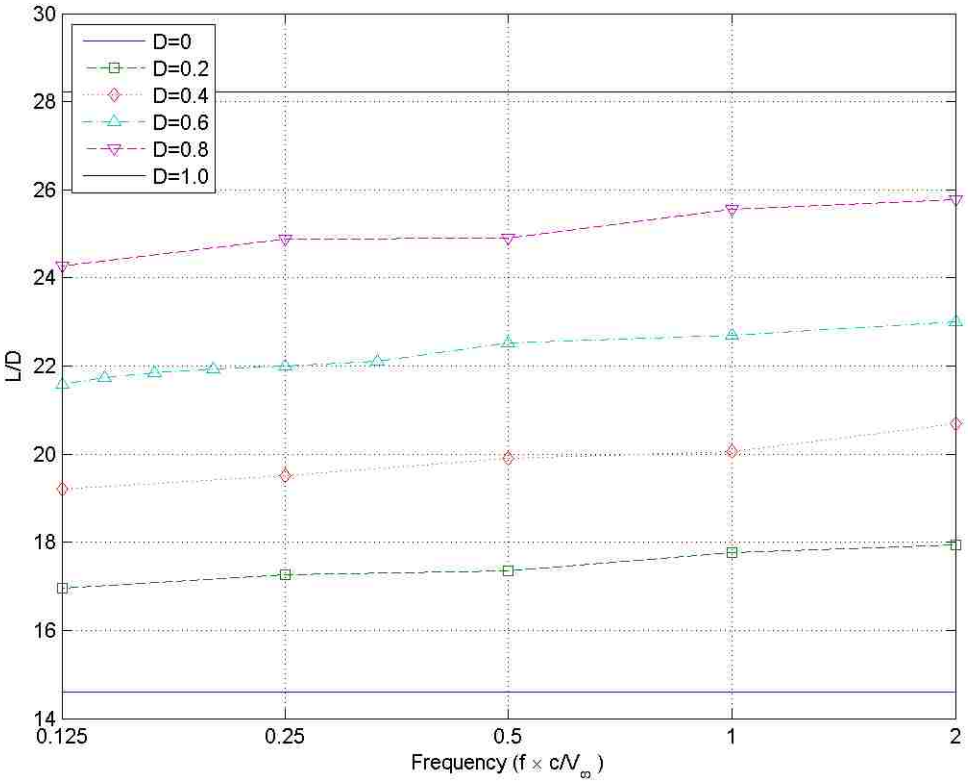

Figure 4.63. Dependence of mean lift-to-drag ratio on actuator frequency and duty cycle (f_{nd} =20)

Finally, to estimate the effectiveness of the actuator with respect to power requirements, the ratio of the obtained L/D values to the corresponding power-equivalent steady values is plotted in Figure 4.64. As shown, a clear dependence of actuator

effectiveness on frequency is observed. Regardless of duty cycle, the effectiveness of the actuator improves as the actuation frequency is increased. The improvement observed in the lift-to-drag ratio for the frequencies strongly correlated to the reductions observed in drag (for comparison, see Figure 4.62). As with the lift and drag, there is no clear relationship between duty cycle and the lift-to-drag ratio. Figure 4.64 indicates that there exist clear potential advantages of a pulsed actuator. However, due to the lack of a clear understanding of the effect of duty cycle on actuator effectiveness, application specific optimization will be required to make use of the concept in practice.

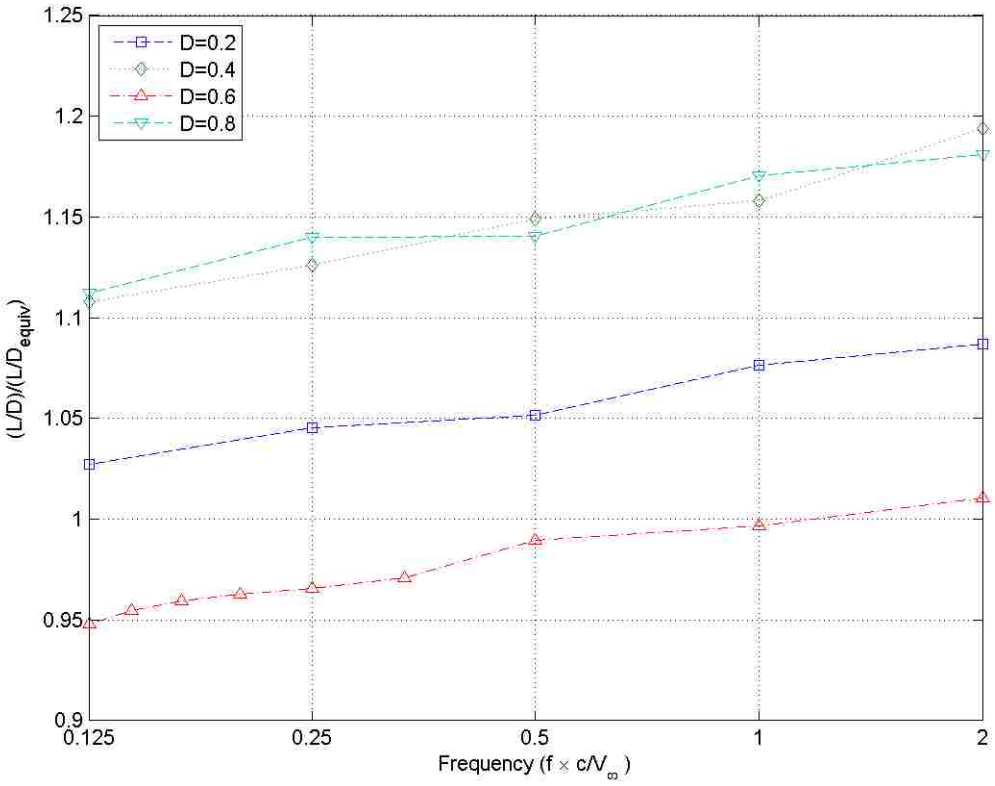

Figure 4.64. Lift-to-drag ratio enhancement as function of frequency and duty cycle

4.3. OBSERVATION OF DOUBLE PEAK IN C_L WAVEFORM IN F=0.25 AND F=0.125 CASES

To illustrate the mechanism responsible for the double peak wave formation, Figure 4.65 shows the flow-field developments over the course of a single actuation

period for the f=0.25, D=0.4 case. In this figure, frames corresponding to peaks or troughs in the C_l waveform are indicated in the appropriate captions. Frame (a) corresponds to the instant before the actuator pulse. As indicated, this corresponds to a peak in the C_l waveform. With the actuator pulse comes a quick reduction in LSB size and the associated suction peak, leading to the C_l trough corresponding to frame (c). However, as the actuator continues to operate, the leading edge suction peak improves substantially, and the pressure over the aft portion of the airfoil decreases slightly. These effects combine to form the C_l peak in frame (g). Following frame (g), the pressure over the aft portion of the airfoil recovers, resulting in the trough in frame (k). From frame (k) to the beginning of the next duty cycle, the LSB continues to become larger, propagating downstream, and resulting in lift enhancement, which leads back to the initial C_l peak.

Figure 4.66 shows the pressure distributions of the peaks and troughs for all of the f=0.25 cases. Though not immediately evident, the mechanisms responsible for the 2-peak waveform are roughly the same. Initially following the t_p/T peak, the actuator destroys or reduces the suction peak associated with the LSB, reducing the lift coefficient. However, the actuator gradually improves the natural suction peak of the airfoil, and by accelerating the flow, decreases the pressure over the mid and aft portions of the airfoil. Eventually, these effects dissipate, leading to the final trough. As time progresses, the LSB continues to develop, moving downstream, and enhancing the lift at the end of the duty cycle and the beginning of the next.

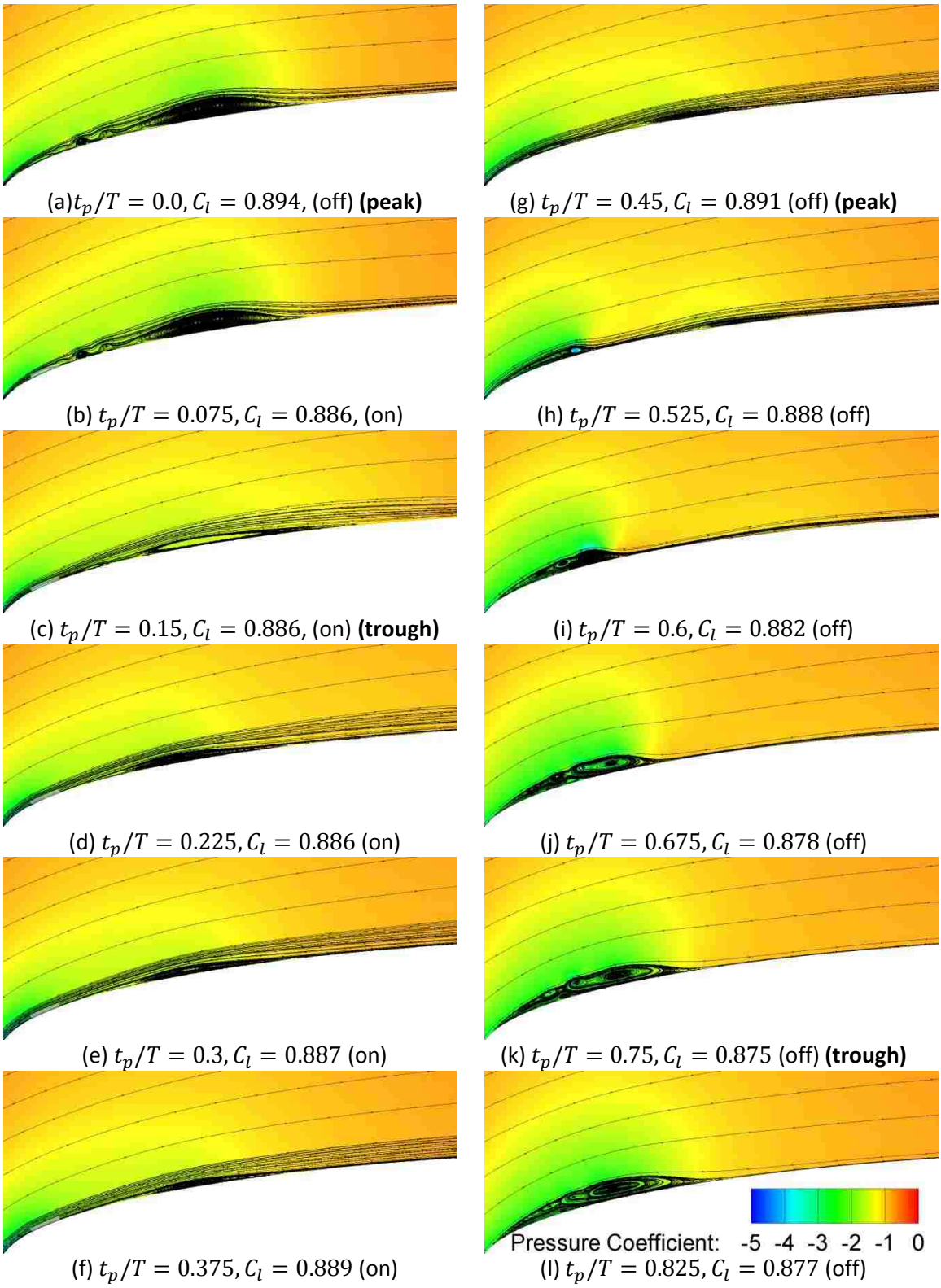

(a)$t_p/T = 0.0, C_l = 0.894$, (off) **(peak)**

(b) $t_p/T = 0.075, C_l = 0.886$, (on)

(c) $t_p/T = 0.15, C_l = 0.886$, (on) **(trough)**

(d) $t_p/T = 0.225, C_l = 0.886$ (on)

(e) $t_p/T = 0.3, C_l = 0.887$ (on)

(f) $t_p/T = 0.375, C_l = 0.889$ (on)

(g) $t_p/T = 0.45, C_l = 0.891$ (off) **(peak)**

(h) $t_p/T = 0.525, C_l = 0.888$ (off)

(i) $t_p/T = 0.6, C_l = 0.882$ (off)

(j) $t_p/T = 0.675, C_l = 0.878$ (off)

(k) $t_p/T = 0.75, C_l = 0.875$ (off) **(trough)**

(l) $t_p/T = 0.825, C_l = 0.877$ (off)

Figure 4.65. Pressure coefficient contour and streamline distributions over 1 duty cycle (f=0.25, D=0.4)

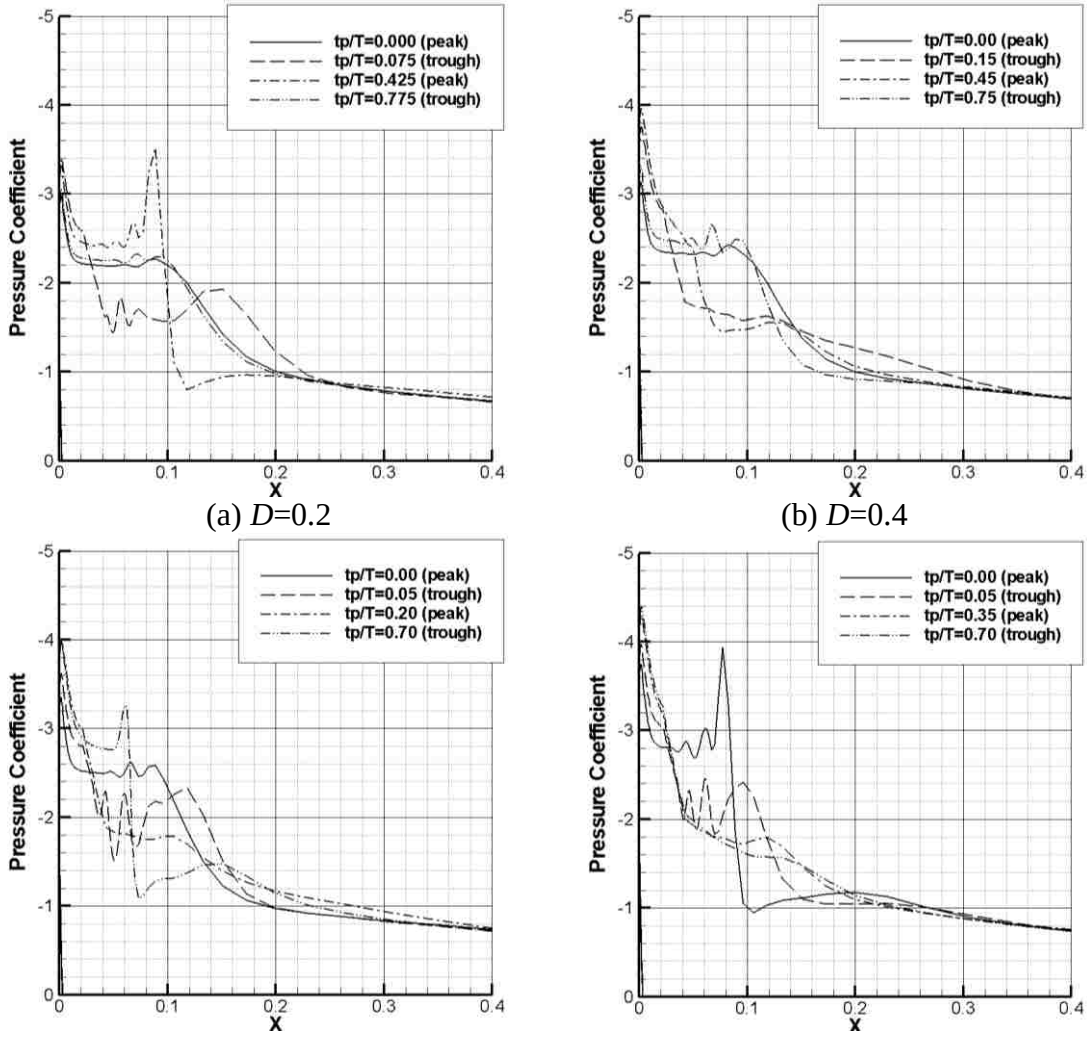

(a) D=0.2 (b) D=0.4

(c) D=0.6 (d) D=0.8

Figure 4.66. Pressure distributions at peaks and troughs in C_l amplitude (f=0.25)

5. ACTUATOR SCALABILITY AND PRACTICAL CONSIDERATIONS

For these computational results to be of practical use to engineers, it is necessary to establish a mathematical link between the dimensionless parameters used in this study and physically measurable plasma actuator parameters. The most easily measurable actuator performance characteristic is thrust, measured in force per unit length. Thus, in this exercise, a link is established between the dimensionless force magnitude f_{nd} and the physical actuator thrust T'. Beginning with equation (1), reproduced here for convenience, we have

$$f_{nd} = \frac{f_d c}{\rho_\infty V_\infty^2}. \tag{1}$$

The dimensional body force magnitude f_d can be related to thrust T' via

$$f_d = \frac{T'}{A_{eff}}, \tag{2}$$

where A_{eff} is the effective plasma discharge volume per unit span. For the numerical solutions to be truly representative of physical reality, the following relation must hold true:

$$A_{eff} = A^* c^2, \tag{3}$$

where A^* is the cross-sectional area of the region to which the body force is applied in the simulation in dimensionless units (for this case A^*=0.02×0.003=6e-5). Substituting equations (2) and (3) into (1), and rearranging slightly, we find

$$f_{nd} A^* = \frac{T'}{\rho_\infty V_\infty^2 c}. \tag{4}$$

This equation is highly useful, insofar as the dependence of peak actuator effectiveness on velocity and the chord are immediately made obvious. However, for cross-referencing with CFD results, it is convenient to express velocity in terms of the Reynolds number. Hence, both sides of equation (4) are then multiplied by Re^2 to eliminate V_∞ from the right hand side:

$$f_{nd} A^* Re^2 = \frac{\rho_\infty}{\mu_\infty^2} T' c. \tag{5}$$

The remaining dimensionless term on the right hand side is a convenient scaling parameter, as will be shown later, and thus is given a special designation,

$$K_{sc} \equiv \frac{\rho_\infty}{\mu_\infty^2} T' c. \tag{6}$$

Substituting the definition for K_{sc} into equation (5), we arrive at

$$f_{nd} A^* Re^2 = K_{sc}. \tag{7}$$

K_{sc} is a convenient parameter for this application for several reasons. It is quite simple to compute for a physical actuator, requiring only knowledge of the free-stream operating conditions, characteristic length scale, and actuator thrust. As shown in equation (6), K_{sc} is proportional to actuator thrust (and hence power), so for constant flow conditions and chord length, K_{sc} scales linearly with T'. Conversely, for a constant T', K_{sc} scales proportionally with the chord length. The two characteristic flow parameters, ρ_∞ and μ_∞, though appearing in the Reynolds number, are not design parameters, and for most low Reynolds number applications are treated as constants. The remaining parameters are design parameters, independent of velocity. Hence, leaving K_{sc} constant, while altering the Reynolds number in equation (7), we isolate the relationship between f_{nd} and free-stream velocity for a specific actuator configuration (T') and airfoil (c). Additionally, it can be trivially shown that by fixing the ratio K_{sc}/Re in equation (7), we isolate the effect of altering the airfoil size (c) on actuator performance for a specific

actuator (*T'*) and flow velocity (V_∞). By varying K_{sc} and fixing the Reynolds number, we observe the effect of varying actuator thrust on f_{nd} for a specific chord and velocity.

It is convenient to plot equation (7) in a contour plot, as this illustrates many of the relationships previously discussed. Figure 5.1 plots the relationship between K_{sc}, Reynolds number and $f_{nd}A^*$ (the dimensionless equivalent of *T'*). The solid lines in this figure are constant K_{sc} contours. The corresponding values are scaled in millions. Each one of these lines represents a constant power curve for a specific actuator-airfoil combination, and shows the relationship between velocity and maximum actuator effectiveness, as previously described. The dashed lines represent constant K_{sc}/Re contours, and variations in Reynolds number correspond to changes in the chord of the airfoil for a specific *T'* and V_∞, as discussed above. The maximum value on the vertical axis ($f_{nd}A^*$=1.2e-3) is equivalent to f_{nd}=20, and f_{nd}=5, 10, and 15 occur at $f_{nd}A^*$=0.3e-3, 0.6e-3, and 0.9e-3, respectively.

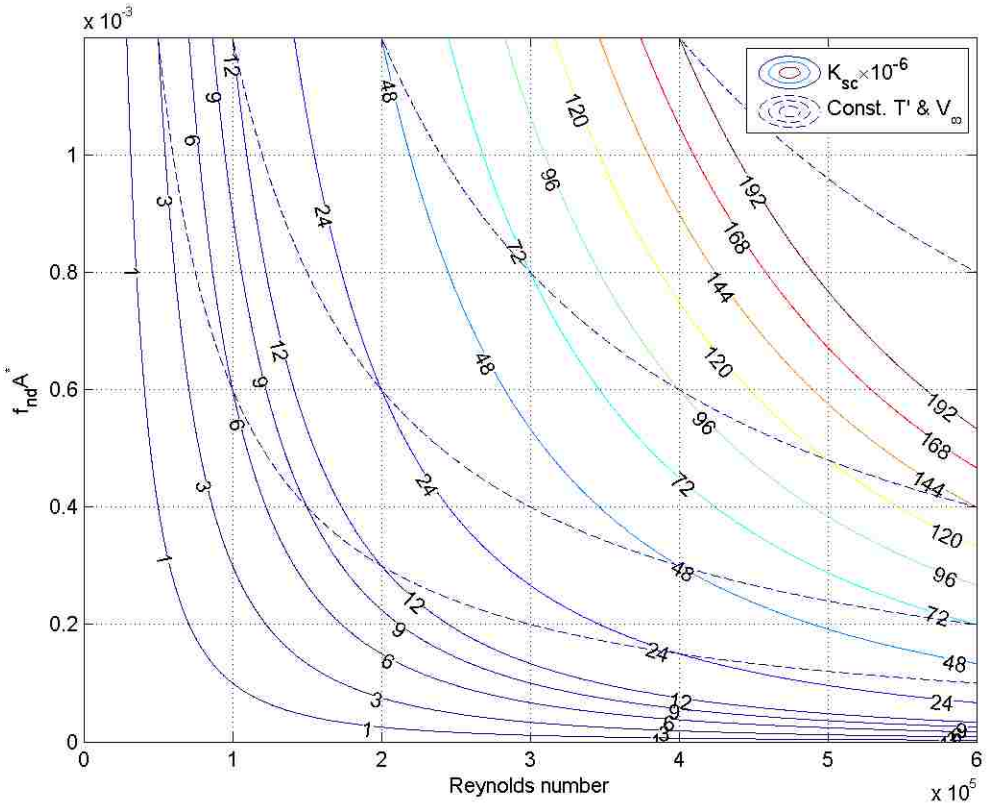

Figure 5.1. Relationship between *Re*, $f_{nd}A^*$, and K_{sc}

Figure 5.1 is a useful plot because it allows us to quickly cross-reference actuator effectiveness, however defined, for a given application with the power required to achieve that effectiveness under a variety of operating conditions. For instance, one could easily generate a contour map of *L/D* enhancement as a function of $f_{nd}A^*$ and *Re* for a given airfoil and angle of attack with a set actuator placement. By overlaying Figure 5.1 over that plot, one could quickly determine the K_{sc} required to achieve a desired condition. This relationship would hold under all conceivable applications using that airfoil, from wind turbines at sea-level to UAVs on Mars. With knowledge of the operating conditions, one could then quickly determine the actuator thrust requirements and design an active control system accordingly.

A quick examination of equations (6) and (7) indicates that, intuitively, for a constant *Re* and *c*, f_{nd} scales linearly with *T'*. This is quickly confirmed in Figure 5.1. As shown, the K_{sc}=3e6, 6e6, 9e6, and 12e6 lines intersect the *Re*=1e5 line in regular intervals, at $f_{nd}A^*$=0.3e-3, 0.6e-3, and 0.9e-3, respectively. From equation (4), it is evident that f_{nd} scales inversely with V_∞^2, indicating that for every doubling of the velocity, the f_{nd} achievable for a given actuator decreases by a factor of 4. This is immediately evident in Figure 5.1. As shown the $f_{nd}A^*$ value corresponding to K_{sc}=12e6 line quarters from 1.2e-3 at *Re*=1e5 to 0.3e-3 at *Re*=2e5, and again to 0.075e-3 at *Re*=4e5. Correspondingly, the K_{sc} required to maintain $f_{nd}A^*$=1.2e-3 is 48e6 at *Re*=2e5 and 192e6 at *Re*=4e5, requiring 4 and 16 times the power requirements of the same actuator at *Re*=1e5, respectively. Similar behavior is observed when investigating the relationship between airfoil size (*c*) and *fnd*, while holding the actuator thrust *T'* and velocity V_∞ constant. It can be trivially shown from equation (4) that f_{nd} scales inversely with the chord-length *c*, indicating that doubling the chord-length will result in a halving of the maximum achievable f_{nd}. This can also be quickly observed by following any one of the dashed lines in Figure 5.1. These findings indicate very strongly that plasma actuators scale poorly to incompressible high speed and large scale flows. This supports the widespread conviction that plasma actuators are extremely inefficient and/or impractical for macro-scale flow control applications.

It is of interest in this study to compare the produced CFD results against hypothetical practical cases to gauge the practicality of the results. In this exercise, the

minimum actuator thrust required to match the most extreme case in this study (f_{nd} = 20, Re=1e5, up to 60% L/D enhancement) is estimated. One of the most intriguing potential applications for plasma actuators is wind turbine technology. Generally, wind turbines are designed with a cut-in (minimum) wind speed near 3 m/s. The chord-length required to meet the Reynolds number (1e5) at this velocity, assuming standard sea-level conditions, (ρ_∞=1.225 kg/m^3, μ_∞=1.78e-5 Pa-s) is 0.484 m. From Figure 5.1, the minimum K_{sc} required to achieve this condition is 12 million. Solving for *T'* using equation (6), we find that the minimum actuator thrust required to operate at this condition is approximately 6.4 mN/m, perhaps greater than ideal, but certainly achievable. Airfoils with larger chords would be incapable of operating at this Reynolds number due to the minimum airspeed requirement, while airfoils with chords smaller than 0.484 m would require more thrust to achieve the required K_{sc}. However, smaller airfoils would reach the cut-in speed at lower Reynolds numbers. For instance, an airfoil with half the chord of the previous would reach the cut-in limit at a Reynolds number of 5e4. The K_{sc} value required at this Reynolds number is only 3 million, meaning the predicted thrust required to achieve f_{nd}=20 in this specific case is only 3.2 mN/m. Conversely, larger airfoils cutting in at a higher *Re* would require greater thrust per unit span. Crudely assuming that turbine blade power produced is proportional to blade area, this information indicates that the ratio of actuator power required to turbine power generated is roughly constant with respect to scale.

Of course, this analysis fails to account for changes in the flow-physics with the Reynolds number. It is unknown what level of effectiveness is required to achieve the desired performance enhancement at lower or higher Reynolds numbers. It is thought that, due to the more dominant presence of the LSB at lower Reynolds numbers, that less thrust would be required to achieve a similar performance enhancement. At higher Reynolds numbers where the LSB is less pronounced, it may not be practically possible to achieve the performance enhancements seen at a Reynolds number of 1e5. However, this is speculative. A more complete parametric analysis, varying Reynolds number and f_{nd} would be required to determine the relationship between *Re* and actuator effectiveness. Such an analysis could then be cross-referenced against Figure 5.1 to determine the optimal operating conditions for the actuator.

6. CONCLUSIONS AND OUTLOOK

6.1. CONCLUSIONS

A body force generation system, such as a plasma actuator, would seem to make an ideal low Reynolds number aerodynamic performance enhancement device, particularly in the presence of LSBs. In this study, it was found that a localized body force was capable of significantly reducing the size of a LSB, or even eliminating it entirely. The actuator was consistently found to marginally increase lift, while dramatically reducing the drag associated with the LSB. The resultant aerodynamic efficiency of the airfoil was as much as 60 percent greater than that of the reference case, and comparable to that attained by the same airfoil at higher Reynolds numbers, where the LSB was not observed.

Further enhancement was achieved by operating the actuator in a pulsed, rather than in steady state. With no special optimization, a high frequency pulsed actuator was found to consistently reduce drag by 8 to 13 percent and improve the airfoil's lift-to-drag ratio by as much as 19 percent over equivalently powered steady actuators. There is clearly potential for enhanced power-equivalent effectiveness using a pulsed actuator.

These results, given the relatively conservative modeling of the actuator, are encouraging. With a greater body force magnitude, higher pulsing frequencies, or lower characteristic Reynolds numbers, the application of an external body force might result in aerodynamic performance surpassing that found at very high Reynolds numbers. However, the effect the actuator had on both the size of the LSB and the aerodynamic performance of the airfoil was highly sensitive to the physical placement of the actuator. It was found that the optimal location of the actuator with respect to the LSB varied with the actuator's strength, but that it was always near the nominal separation point. If placed too far downstream of the separation point, the actuator was found to induce instability. Despite this, the results of this study are promising for body force generators, such as plasma actuators, as a means of eliminating LSBs and generally improving low Reynolds number aerodynamic performance. This study warrants further experimental research into the feasibility of plasma actuators in such applications.

6.2. SUGGESTIONS FOR FUTURE WORK

This computational work could be expanded upon in a number of ways. More sophisticated modeling techniques could be utilized to obtain more accurate solutions. It was assumed in this analysis that the actuator itself (i.e. the exposed electrode) had no aerodynamic footprint, or that the airfoil surface in that region was perfectly smooth. It is unknown how the geometry of the actuator may affect flow-field developments or turbulence in this flow problem. Additionally, a more sophisticated code solving the Navier-Stokes and Maxwell equations would be capable of more accurately approximating the spatial-temporal distribution of the actuator-induced body force. Another assumptions made in this study was that the actuator had no effect on turbulence intensity. Using higher fidelity modeling techniques, such as Large Eddy Simulation (LES) or Direct Numerical Simulation (DNS), it may be possible to estimate these effects.

Another way to expand upon this work would be to use the analysis tools developed in chapter 5 to explore in depth the feasibility and potential effectiveness of plasma actuators as a means of flow control over a variety of phenomena, including LSBs, in numerous applications, such as wind turbines, UAVs, turbo-machinery, Martian aircraft, etc. Such a reference would be highly valuable to the broader research community, in that it would allow researchers to quickly identify the most promising applications for their work, and tailor it toward that end.

BIBLIOGRAPHY

[1] Horton, H. P., "Laminar Separation in two and three-dimensional incompressible flow," PhD Dissertation, University of London, 1968.

[2] King, R. M., Chokani, N., and Mangalam, S. M., "Control of Laminar Separation Bubbles Using an Adaptive Mechanical Turbulator," *40th AIAA Aerospace Sciences Meeting and Exhibit,* AIAA, Ren, NV, Jan. 2002.

[3] Almutairi, J. H., Jones, L. E., and Sandham, N. D., "Intermittent Bursting of a Laminar Separation Bubble on an Airfoil," *AIAA Journal,* Vol. 48, No. 2, Feb. 2010, pp. 414-426.

[4] Zaman, K. and McKinzie, D. J., "Control of "Laminar Separation" Over Airfoils by Acoustic Excitation," *27th AIAA Aerospace Sciences Meeting and Exhibit,* AIAA, Ren, NV, Jan. 1989.

[5] Bak, C., Madsen, H. A., Fuglsang, P., and Rasmussen, F., "Observations and Hypothesis of Double Stall," *Wind Energy,*Vol. 2, No. 1, 1999, pp. 195–210.

[6] Aholt, J., "Influence of Laminar Separation Bubbles on the Aerodynamic Characteristics of Elliptical Airfoils at Low Reynolds Numbers," *2008-2009 Missouri Space Grant Consortium Student Reports and Abstracts,* MOSGC, Columbia, MO, April 2009.

[7] Kruse, M. and Radespiel, R., "Measurement of a Laminar Separation Bubble on a Swept Horizontal Tailplane using μPIV," *38th Fluid Dynamics Conference and Exhibit,* AIAA, Seattle, WA, Jun. 2008.

[8] Radespiel, R., Windte, J., and Scholz, U., "Numerical and Experimental Flow Analysis of Moving Airfoils with Laminar Separation Bubbles," *44th AIAA Aerospace Sciences Meeting and Exhibit*, AIAA, Ren, NV, Jan. 2006.

[9] Zaman, K. B. M. Q., Mckinzie, D. J., and Ramsey, C. L., "A Natural Low-Frequency Oscillation of The Flow Over an Airfoil Near Stalling Conditions," *Journal of Fluid Mechanics,* Vol. 202, 1989, pp. 403-442.

[10] Schreck, S. J. and Robinson, M. C., "Horizontal Axis Wind Turbine Blade Aerodynamics in Experiments and Modeling," *IEEE Transactions on Energy Conversion,* Vol. 22, No. 1, 2007, pp. 61–70.

[11] Hourmouziadis, J., "Aerodynamic design of low pressure turbines," AGARD, 167, 8.1-8.40., 1989.

[12] Sharma, "Impact of Reynolds number on LP turbine performance," NASA/CP-1998-206958, 65-70, 1998.

[13] Stieger, R., Hollis, D., and Hodson, H. "Unsteady Surface Pressures Due to Wake Induced Transition in a Laminar Separation Bubble on a LP Turbine Cascade," *Proceedings of ASME Turbo Expo 2003*, ASME, Atlanta, GA, 2003.

[14] Nagel, A., Levy, D. E., and Shepshelovich, M., "Conceptual Aerodynamic Evaluation of MINI/MICRO UAV," *44th AIAA Aerospace Sciences Meeting and Exhibit*, AIAA, Ren, NV, Jan. 2006.

[15] Leslie, A., Wong, K. C., and Auld, D., "Broadband noise reduction on a mini-UAV Propeller," *14th AIAA/CEAS Aeroacoustics Conference*, AIAA, Vancouver, British Columbia Canada, May 2008.

[16] Asada, K., Ninomiya, Y., Oyama, A., and Fujii, K., "Airfoil Flow Experiment on the Duty Cycle of DBD Plasma Actuator," *47th AIAA Aerospace Sciences Meeting Including the New Horizons Forum and Aerospae Exposition*, AIAA, Orlando, FL, Jan. 2009.

[17] Horstmann, K., Quast, A., and Boermans, L., "Pneumatic turbulators - a device for drag reduction at Reynolds numbers below $5x10^6$," Agard-cp-365, AGARD, 1984.

[18] Enloe, C. L., McLaughlin, T. E., VanDyken, R. D., Kachner, K. D., Jumper, E. J., and Corke, T. C., "Mechanisms and Responses of a Single Dielectric Barrier Plasma Actuator: Plasma Morphology," *AIAA Journal*, Vol. 42, No. 3, 2004, pp. 589–593.

[19] Enloe, C. L., McLaughlin, T. E., VanDyken, R. D., Kachner, K. D., Jumper, E. J., Corke, T. C., Post, M., and Haddad, O., "Mechanisms and Responses of a Single Dielectric Barrier Plasma Actuator: Geometric Effects," *AIAA Journal*, Vol. 42, No. 3, 2004, pp. 595–604.

[20] Patel, M., Ng, T. T., Vasudevan, S., Corke, T. C., Post, M., McLaughlin, T. E., and Suchomel, C. F., "Scaling Effects of an Aerodynamic Plasma Actuator," *Journal of Aircraft*, Vol. 45, No. 1, Feb. 2008.

[21] Corke, T. C. and Post, M. L., "Overview of Plasma Flow Control: Concepts, Optimization, and Applications," *43rd AIAA Aerospace Sciences Meeting and Exhibit*, Ren, NV, Jan. 2005.

[22] Asada, K. and Fujii, K., "Computational Analysis of Unsteady Flow-field Induced by Plasma Actuator in Burst Mode," *5th Flow Control Conference*, AIAA, Chicago, Ill, Jul. 2010.

[23] Huang, J., Corke, T. C., and Thomas, F. O., "Plasma Actuators for Separation Control of Low Pressure Turbine Blades," *41st AIAA Aerospace Sciences Meeting and Exhibit,* AIAA, Ren, NV, Jan. 2003.

[24] Nelson, R. C., Corke, T. C., Othman, H., Patel, M. P., Vasudevan, S., and Ng, T., "A Smart Wind Turbine Blade Using Distributed Plasma Actuators for Improved Performance," *46th AIAA Aerospace Sciences Meeting and Exhibit*, AIAA, Ren, NV, Jan. 2008.

[25] Sosa, R. and Artana, G., "Steady control of laminar separation over airfoils with plasma sheet actuators," *Journal of Electrostatics*, Vol. 64, 2006, pp. 604–610.

[26] Hall, K. D., Jumper, E. J., and Corke, T. C., "Potential Flow Model of a Plasma Actuator as a Lift Enhancement Device," *43rd AIAA Aerospace Sciences Meeting and Exhibit,* AIAA, Ren, NV, Jan. 2005.

[27] Vo, H. D., "Control of Rotating Stall in Axial Compressors Using Plasma Actuators," *37th AIAA Fluid Dynamics Conference and Exhibit*, AIAA, Miami, FL, Jun. 2007.

[28] Greenblatt, D. and Wygnanski, I. J., "The control of flow separation by periodic excitation," *Progress in Aerospace Sciences*, Vol. 36, 2000, pp. 487-545.

[29] Assel, T. W., *Computational Study of Flow Over Elliptic Airfoils for Rotor/Wing Unmanned Arial Vehicle Applications*, Master's thesis, University of Missouri-Rolla, Rolla, MO, 2007.

[30] Buning, P. G., Jespersen, D. C., Pulliam, T. H., Klopfer, G. H., Chan, W. M., Slotnick, S. E., and Renze, K. J., OVERFLOW User's Manual : Version 1.8aa, NASA, 2003.

[31] Choi, S. and Kwon, O. J., "Aerodynamic Characteristics of Elliptic Airfoils at High Reynolds Numbers," *Journal of Aircraft*, Vol. 45, No. 2, Apr. 2008, pp. 641-650.

[32] Kwon, K. and Park, S. O., "Aerodynamic Characteristics of an Elliptic Airfoil at Low Reynolds Number," *35th AIAA Fluid Dynamics Conference and Exhibit*, AIAA, Toronto, Ontario Canada, Jun. 2005.

[33] Mertz, B., Corke, T. C., "Single-dielectric barrier discharge plasma actuator modelling and validation," *Journal of Fluid Mechanics*, Vol. 669, pp. 557-583, 2011.

VITA

Justin Roger Aholt was born on December 18, 1988. He began his education at the University of Missouri-Rolla in 2007 and graduated *summa cum laude* with a Bachelor of Science in Aerospace Engineering in May 2010. Post graduation, he elected to pursue a Master of Science degree in Aerospace Engineering as a Chancellor's Fellow at the Missouri University of Science and Technology.